

MULTIMODAL BIOMETRIC RECOGNITION USING IRIS, KNUCKLEPRINT AND PALMPRINT

A Thesis Submitted

in Partial Fulfillment of the Requirements

for the Degree of

Doctor of Philosophy

by

ADITYA NIGAM



to the

**DEPARTMENT OF COMPUTER SCIENCE AND ENGINEERING
INDIAN INSTITUTE OF TECHNOLOGY KANPUR, INDIA**

August 2014



CERTIFICATE

It is certified that the work contained in the thesis entitled "*Multimodal Biometric Recognition using Iris, Knuckleprint and Palmprint*" by *Aditya Nigam* has been carried out under my supervision and that this work has not been submitted elsewhere for a degree.

August 2014

Dr. Phalguni Gupta
Professor,
Department of Computer Science and Engineering,
Indian Institute of Technology Kanpur,
Kanpur-208016, INDIA.

Synopsis

Personal authentication is one of the basic requirements of our modern day society. Almost financial as well as personal security related applications expect to have an automated, efficient, near real time and highly accurate access control mechanism. Traditional methods of authentication are based on token and/or knowledge. Biometrics is an alternative to traditional methods because it is harder to circumvent. Biometric based authentication systems use individual's characteristics which are based on either behavior (voice, signature, gait *etc*) or physiology (face, iris, palmprint, fingerprint, knuckleprint, ear *etc*). These characteristics are hard to circumvent because they cannot be lost or forgot like token or knowledge based methods. Some of the well known identification systems make use of fingerprint, face, iris, palmprint, finger-knuckleprint, ear, gait *etc*. But each biometric trait has its own set of challenges and trait specific issues. Hence, none of the traits can be considered as the best one because it depends on the type of applications where it has to be applied.

The performance of any unimodal biometric system is dependent on factors like environment, atmosphere, sensor precision. Also, there are several trait specific challenges such as pose, expression, aging *etc* for face recognition, occlusion and acquisition related issues for iris and poor quality and social acceptance related

issues for fingerprint. Hence, fusion of more than one biometric samples, traits or algorithms to achieve superior performance is an alternative way to achieve the better performance and is termed in literature as multi-biometrics or multimodal biometrics. In this thesis, we have considered three different biometric traits *viz.* iris, knuckleprint and palmprint. Iris can be considering as the best biometric in terms of performance which is fused with two other biometric traits to obtain an efficient multi-modal biometric system.

The iris is a ring made up of tissues that allows light to enter into the eye. Thin circular diaphragm between cornea and lens is called as iris which has abundance of micro-texture such as crypts, furrows, ridges, corona, freckles and pigment spots. These textures are randomly distributed and hence they are believed to be unique. On the other hand, knuckleprint and palmprint do not have such a rich anatomical structure. But, they possess line like (*i.e.* knuckle-lines, palm-lines, wrinkles) rich pattern based structure in vertical, horizontal as well as diagonal directions which can be very useful if they are used in conjunction with iris samples because iris has mostly radial features. It has been observed experimentally that such a fusion of orthogonal multiple biometric modalities facilitates the system to reject the imposter confidently.

Utilization of multi modality information can be useful to achieve high performance while working over large database. The spoof vulnerability is much lesser than unimodal system; hence it is ideal for outdoor unattended supervision in uncontrolled environments. However, not much work has been done in this area mainly due to non-availability of multimodal datasets.

Any biometric based personal authentication system consists of several steps such as : Sample Acquisition, ROI Extraction, Sample Normalization, Preprocessing,

Feature Extraction and Template Matching. Each step affects overall performance of the system; segmentation is one of the most critical steps. Wrong segmentation renders the subsequent steps meaningless.

This thesis proposes an efficient multimodal authentication system which fuses iris, knuckleprint and palmprint images. To the best of our knowledge, this is the first effort in which iris, knuckleprint and palmprint samples are fused. In this work we have proposed new iris, knuckleprint and palmprint extraction algorithms. Several quality parameters for iris and knuckleprint modalities are proposed. Each biometric trait is enhanced and transformed using the proposed local enhancement and *LGBP* transformation. Tracking based matching algorithm is proposed to perform biometric sample identification/recognition that uses corner features and *CIOF* dissimilarity measure.

There are eight chapters in this thesis. The introduction of any general biometric system, stages involved, modes of operation, traits and their properties are discussed in Chapter 1. Also motivation and performance parameter are described along with the key contributions presented. In the next chapter the detailed literature review is presented for each of the three traits considered in this thesis work. There are several image processing as well as computer vision based techniques that are used in designing the systems. They are discussed in Chapter 3.

In Chapter 4, iris based recognition system has been proposed. The iris segmentation is done efficiently using an improved circular hough transform for inner iris boundary (*i.e* pupil) detection. The robust integro-differential operator is used to detect outer iris boundary that makes use of the pupil location. The quality of the acquired iris sample is estimated using the proposed quality assessment parameters and if it is less than a predefined threshold then it is recaptured. This early quality

assessment is very crucial in order to handle poor quality and non-ideal imagery. The segmented iris is normalized to polar coordinates (*i.e.* rectangular strips) and is preprocessed using the proposed *LGBP* (Local Gradient Binary Pattern) to obtain robust features. The *KLT* based corners are extracted and matched using the proposed dissimilarity measure *CIOF* (Corners having Inconsistent Optical Flow). The proposed system has been tested over publicly available CASIA 4.0 Interval and Lamp iris databases consisting of 2,639 and 16,212 images respectively. It is found that *CRR* (Rank 1 accuracy) of the proposed system is 100% and 99.87% for Interval and Lamp databases respectively. Further, its *EER* for Interval and Lamp are 0.109% and 1.3% respectively.

In Chapter 5, knuckleprint based recognition system has been proposed. The knuckleprint segmentation is done by estimating the central knuckle-line using a new modified version of gabor filter called curvature gabor filter. The quality of the acquired knuckleprint sample is estimated using the proposed quality assessment parameters. The segmented knuckleprint ROI is preprocessed using the proposed *LGBP* (Local Gradient Binary Pattern) to obtain robust features. The *KLT* based corners are extracted and matched using the proposed dissimilarity measure *CIOF* (Corners having Inconsistent Optical Flow). The proposed system has been tested over publicly available PolyU knuckleprint databases consisting of 7,920 images. It is found that *CRR* of the proposed system is 99.79% with an *EER* of 0.93% over PolyU knuckleprint database.

In Chapter 6, palmprint based recognition system has been presented. The palmprint segmentation is done by obtaining the two valley points and then a square shaped ROI is clipped using that. The segmented palmprint is preprocessed using the proposed *LGBP* (Local Gradient Binary Pattern) proposed dissimilarity

measure *CIOF* (Corners having Inconsistent Optical Flow) is used for matching. The system has been tested over publicly available CASIA and PolyU palmprint databases consisting of 4,528 and 7,720 images respectively. It is found that *CRR* (Rank 1 accuracy) of the proposed system is 100% and 99.95% for CASIA and PolyU palmprint databases respectively. Further, its *EER* for CASIA and PolyU are 0.15% and 0.41% respectively.

In Chapter 7, details of multi-modal based recognition system and all stages involved in it are discussed. The major focus is over the chimeric multimodal database creation and its experimental analysis. Three multimodal systems *viz.* iris and knuckleprint, knuckleprint and palmprint and finally iris, knuckleprint and palmprint have been discussed. Several testing strategies such as intersession matching, one training and one testing and multiple training and multiple testing have been considered. Two publicly available iris databases (CASIA Interval and LAMP) are fused with two public palmprint databases (CASIA, PolyU) while for knuckleprint largest publicly available PolyU database is used. Hence, 4 tri-modal databases are generated for testing. It is observed that the performance of the trimodal system shows almost perfect behavioral (*i.e* $CRR = 100\%$ and $EER = 0\%$) under various testing strategies.

The last chapter concludes the work carried out in the thesis. It is shown through experimental analysis that orthogonal feature based modality fusion of iris with other biometrics like knuckleprint and palmprint can be very useful while working on large databases. It is observed that very high accuracy can be achieved. The proposed system can perform single verification of an individual within a second that is fast enough for any real-time application.

Acknowledgements

It gives me immense pleasure in expressing my profound sense of gratitude to my thesis supervisor Prof. Phalguni Gupta. I am highly indebted and deeply grateful to him for his inspiring guidance, constant encouragement, valuable suggestions and ingenious ideas. His enormous knowledge and understanding has greatly helped me in better understanding of various aspects of Biometrics. His expertise in the area of Biometrics and enthusiasm in the research have been of great value to me.

Aditya Nigam

Dedicated

to

*My Beloved Parents, All My Respected Teachers & My
Wife Mrs. Jyoti Nigam and Son Master Bhavya Nigam*

Contents

List of Tables	xx
List of Figures	xxiv
List of Algorithms	xxxix
List of Abbreviations	xxxiii
1 Introduction	1
1.1 Biometric Traits	4
1.1.1 Physiological based Traits	4
1.1.2 Behavioral	7
1.2 Modes of Biometric System	9
1.2.1 Enrollment	9
1.2.2 Verification	10
1.2.3 Identification	11
1.3 Multi-biometric System	12
1.3.1 Types of Multi-biometric System	12
1.3.2 Fusion Levels	15
1.4 Motivation of Thesis	16
1.4.1 Iris	16

1.4.2	Knuckleprint	17
1.4.3	Palmprint	18
1.4.4	Multi-biometrics	18
1.5	Performance Analysis Metrics	20
1.5.1	Verification Performance Metrics	20
1.5.2	Identification Performance Metrics	23
1.6	Thesis Contribution	24
1.6.1	ROI Extraction	25
1.6.2	Quality Estimation	25
1.6.3	Biometric Feature Enhancement and Transformation	26
1.6.4	Biometric Feature Extraction and Matching	26
1.6.5	Multimodal Biometric System	26
1.7	Thesis Organization	27
2	Literature Review	29
2.1	Iris based Biometric System	29
2.2	Knuckleprint based Biometric System	36
2.3	Palmprint based Biometric System	40
2.4	Multi-modal Biometric System	43
3	Preliminaries	45
3.1	Local Binary Pattern (LBP)	46
3.2	Corner Point Detection	49
3.3	Sparse Point Tracking (KLT)	50
3.4	Phase Only Correlation (POC)	53
4	Iris Recognition System	57
4.1	Iris ROI Extraction	57
4.1.1	Iris Inner Boundary Localization	58

4.1.2	Iris Outer Boundary Localization	62
4.1.3	Proposed Segmentation Algorithm	64
4.1.4	Iris Normalization	65
4.2	Iris Quality Estimation	68
4.2.1	Focus (F) based Quality Attribute	69
4.2.2	Motion Blur (MB) based Quality Attribute	70
4.2.3	Contrast and Illumination (CI) based Quality Attribute	72
4.2.4	Dilation (D) based Quality Attribute	72
4.2.5	Specular Reflection (SR) based Quality Attribute	73
4.2.6	Occlusion (O) based Quality Attribute	73
4.2.7	Quality Class Determination	79
4.3	Iris Image Preprocessing	80
4.3.1	Iris Image Enhancement	81
4.3.2	Iris Image Transformation	82
4.4	Iris Feature Extraction and Matching	84
4.4.1	Corners having Inconsistent Optical Flow (CIOF)	84
4.4.2	Matching Algorithm	85
4.5	Databases	87
4.5.1	Databases Used	87
4.5.2	Testing Strategy	88
4.6	Experimental Results	89
4.6.1	Iris Segmentation Analysis	89
4.6.2	Threshold Selection	91
4.6.3	Impact of Enhancement on System Performance	93
4.6.4	Comparative Analysis	94
5	Knuckleprint Recognition System	99
5.1	Knuckleprint ROI Extraction	100

5.1.1	Knuckle Area Detection	100
5.1.2	Central Knuckle-Line Detection	102
5.1.3	Central Knuckle-Point Detection	104
5.2	Knuckleprint Image Quality Extraction	106
5.2.1	Focus (F)	108
5.2.2	Clutter (C)	108
5.2.3	Uniformity based Quality Attribute (S)	109
5.2.4	Entropy based Quality Attribute (E)	110
5.2.5	Reflection based Quality Attribute (Re)	111
5.2.6	Contrast based Quality Attribute (Con)	112
5.2.7	Quality Class Determination	113
5.3	Knuckleprint Image Preprocessing	114
5.4	Knuckleprint Feature Extraction and Matching	115
5.4.1	Corners having Inconsistent Optical Flow (CIOF)	115
5.5	Database Specifications	117
5.5.1	Testing Strategy	118
5.6	Performance Analysis	119
5.6.1	Knuckleprint Segmentation	119
5.6.2	Threshold Selection	119
5.6.3	Comparative Analysis	121
6	Palmprint Recognition System	123
6.1	Palmprint ROI Extraction	123
6.2	Palmprint Preprocessing	125
6.3	Palmprint Feature Extraction and Matching	126
6.3.1	Corners having Inconsistent Optical Flow (CIOF)	127
6.4	Database	128
6.4.1	Testing Strategy	131

6.5	Performance Analysis	131
7	Multimodal Based Recognition System	135
7.1	Knuckleprint and Palmprint Fusion	136
7.1.1	Multi-modal Databases Creation	136
7.1.2	Testing Strategy	138
7.1.3	Performance Analysis	140
7.2	Iris and Knuckleprint Fusion	144
7.2.1	Multimodal Database Creation	145
7.2.2	Testing Strategy	146
7.2.3	Performance Analysis	147
7.3	Iris, Knuckleprint and Palmprint Fusion	149
7.3.1	Multimodal database creation	151
7.3.2	Testing Strategy	152
7.3.3	Performance Analysis	152
8	Conclusions	159
	References	164
	Publications	177

List of Tables

1.1	Biometric Properties ($L = Low$; $M = Medium$; $H = High$)	19
4.1	Quality Parameters and Quality Class for Images in Fig. 4.19	80
4.2	Iris Database Specifications	88
4.3	Database and Testing Strategy Specifications	88
4.4	Values of Various Parameters used in Algorithm 4.1 and 4.2	89
4.5	Variation in Threshold needed for Correct Segmentation	90
4.6	Required Parametric Variations: '–' stands for no change, '↑' stands for increasing and '↓' for decreasing the parameter value	91
4.7	Segmentation Error. (Rows Below Images: Errors Occurred in Inter- val, Lamp Databases)	91
4.8	Threshold Selection for CASIA V4 Interval and Lamp Iris Database using only <i>vcode</i> Matching over Validation Set of First 100 Subjects.	92
4.9	Enhancement based Performance boost-up over Iris Interval Databases (In the above Table fusion referred as <i>vcode+hcode</i>)	93
4.10	Performance Analysis of Proposed System	95
4.11	Comparative Performance Analysis over CASIA V4 Interval and Lamp Iris Database	96
5.1	Database Specifications	119

5.2	Parameterized Performance Analysis of the proposed system on PolyU Knuckleprint Database. (only <i>vcode</i> matching)	120
5.3	Comparative Performance Analysis over PolyU Knuckleprint (Results as reported in [27])	121
6.1	Database Specifications	130
6.2	Palmprint Results (L= <i>LEFT Hand</i> ,R= <i>RIGHT Hand</i> ,ALL= <i>L + R</i>)	132
6.3	Comparative Performance with Other Systems	134
7.1	Database Specifications (L= <i>LEFT Hand</i> ,R= <i>RIGHT</i> ,ALL= <i>L + R</i>)	139
7.2	Testing Strategy Specifications (L= <i>LEFT</i> ,R= <i>RIGHT</i> ,ALL= <i>L + R</i>)	141
7.3	Consolidated Results (L= <i>LEFT Hand</i> ,R= <i>RIGHT Hand</i> ,ALL= <i>L+R</i>)	142
7.4	Database Specifications	146
7.5	Performance Analysis of the Proposed System over Iris Interval and Lamp Databases along with Knuckleprint PolyU Database (In the above Table fusion referred as <i>vcode+hcode</i>)	149
7.6	Database Specifications of Four Self Created Tri-Modal Database using Iris, Knuckleprint and Palmprint.	150
7.7	Database Specifications for Interval_CASIA (<i>db1</i>) containing images from 349 Subjects in $(3 + 4) = 7$ different poses. First 3 images are considered for training and Last 4 are taken as testing.	153
7.8	Database Specifications for Interval_PolyU (<i>db2</i>) containing images from 349 Subjects in $(3 + 4) = 7$ different poses. First 3 images are considered for training and Last 4 are taken as testing.	154
7.9	Database Specifications for Lamp_Casia (<i>db3</i>) containing images from 566 Subjects in $(4 + 4) = 8$ different poses. First 4 images are considered for training and Last 4 are taken as testing.	155

7.10 Database Specifications for Lamp-PolyU (<i>db4</i>) containing images from 386 Subjects in $(6 + 6) = 12$ different poses. First 6 images are con- sidered for training and Last 6 are taken as testing.	156
---	-----

List of Figures

1.1	Some Biometric Traits	2
1.2	Flow Diagram of Enrollment Process	10
1.3	Flow diagram of Authentication Process	11
1.4	Flow Diagram of Identification Process	12
1.5	Fingerprint Sensors	13
1.6	Two Fingerprint Matchers (Multi-algorithm)	14
1.7	Samples of Same Fingerprint (Multi-instance)	14
1.8	Five different Biometric Traits (Multi-Modal)	15
1.9	Iris, Knuckle and Palmprint Anatomy	17
1.10	Graphical Representation of FAR and FRR	21
1.11	Graphical Representation of EER and Accuracy	22
1.12	Graph Showing Genuine and Imposter Score Distribution (here $\int_0^t (s(x H_G)dx)$ represents the genuine similarity score distribution)	23
1.13	Graph showing Genuine Vs Imposter Best Score Graph	24
2.1	Images are taken from [19, 18]	30
2.2	Mapping of radial rays into a polar representation pupil and iris boundaries become vertical edges [13]	31

2.3	(a) Most Significant bit-plane 7 (b) Bit-plane 6 (c) Bit-plane 5 (d) Bit-plane 4 (e) Bit-plane 3 (f) Bit-plane 2 (g) Bit-plane 1 (h) Least Significant bit-plane 0 [11].	31
2.4	Iris Deformable Model [50]	32
2.5	Iris Image Preprocessing [50] : (a) Original Image, (b) Detected Inner Boundary, (c) Detected Outer Boundary, (d) Lower Half of Iris, (e) Normalized, (f) Eyelid Masking and (g) Enhanced Image	33
2.6	Overview of Non-ideal Iris Recognition System [22]	33
2.7	Off Angle Iris Segmentation [2]	34
2.8	Two Most Popular Iris Systems	35
2.9	Steps Involved for Feature Vector Extraction [51]	36
2.10	Ordinal Measures for Iris Recognition [66]	37
2.11	Knuckleprint Acquisition System [77], (a) Device, (b) Raw Sample, (c) ROI Localized, (d) Cropped.	37
2.12	Ensemble of Local and Global Features [80]	38
2.13	Improvement over Gabor based <i>Compcode</i> . (a) Original Image, (b) Orientation Code (<i>ImCompCode</i>), (c) Magnitude Code (<i>MagCode</i>) (Images taken from [79])	39
2.14	Local Feature Extraction	40
2.15	Partitioning for Zernike based Palmprint System [7]	41
2.16	Partitioning for Phase based Palmprint System [9]	42
2.17	Partitioning for Stockwell based Palmprint System [6]	42
2.18	Partitioning for <i>DCT</i> based Palmprint System [8]	43
3.1	<i>LBP</i> Computation	47
3.2	Application of <i>LBP</i> in Face Recognition	48
3.3	Corner Features shown in Red	50
3.4	Hand Tracking Application	53

3.5	Phase Only Correlation (<i>POC</i>) between two translated images. Image in (c) represents the corresponding <i>POC</i> values for each spatial location	54
4.1	Overall Architecture of the Proposed Iris Recognition System	58
4.2	Iris Segmentation	58
4.3	Iris Pupil Segmentation (Thresholding)	59
4.4	Iris Pupil Segmentation (Gradient based Thresholding using Sobel)	60
4.5	For any radius r , any point (x, y) having 2 pupil centers (c_1^x, c_1^y) and (c_2^x, c_2^y)	61
4.6	Segmented Iris Pupil	61
4.7	All Steps in Iris Pupil Segmentation	62
4.8	Application of Integro-differential Operator	62
4.9	Iris Localization (1 st Row : Original Iris, 2 nd Row : Segmented Iris)	65
4.10	Normalization of the Cropped Iris	67
4.11	Focus Filter Response	70
4.12	JNB Edge Width	71
4.13	Occlusion in Normalized Iris	74
4.14	Application of Region-Growing	75
4.15	Eyelid Regions: Arrows Denote the Direction for Region-Growing	75
4.16	Determination of Eyelash Region	78
4.17	Reflection Detection by Thresholding	78
4.18	Overall Occlusion Mask	79
4.19	Quality Estimation	80
4.20	Iris Texture Enhancement	81
4.21	<i>LGBP</i> Transformation (Red: -ve gradient; Green: +ve grad.; Blue: zero grad.)	82
4.22	Original and Transformed (<i>vcode</i> , <i>hcode</i>) for Iris ROI's	83

4.23	Iris Images	87
4.24	Segmentation Error Hierarchy (Numbers Mentioned for each Subcategory Specify the Number Images of that Category for Interval Database.)	90
4.25	Parameterized ROC Curve of the Proposed System for Iris Interval Database (only <i>vcode</i> matching)	93
4.26	Parameterized <i>ROC</i> Analysis of the Proposed System for Iris Lamp Database (only <i>vcode</i> matching)	94
4.27	Enhancement based Performance boost-up in terms of Receiver Operating Characteristic Curves for the Proposed System	95
4.28	Comparative Analysis of Proposed System over Interval Database	97
4.29	Comparative Analysis of Proposed System over Lamp Database	97
5.1	Overall Architecture of the Proposed Knuckleprint Recognition System	100
5.2	Knuckleprint ROI Annotation	101
5.3	Knuckle Area Detection	101
5.4	Conventional Gabor Filter	102
5.5	Curvature Knuckle Filter	103
5.6	Knuckle Filter	104
5.7	Knuckleprint ROI detection. (a) Knuckle filter response is superimpose over the knuckle area with blue color, (b) Full Annotated and (c) FKP (FKP_{ROI})	105
5.8	Some Segmented Knuckleprints	106
5.9	Poor Quality Knuckleprint ROI Samples	107
5.10	Defocus based Quality Attribute F and C	109
5.11	Uniformity based Quality Attribute (S)	110
5.12	Entropy based Quality Attribute E	111
5.13	Reflection based Quality Attribute Re	112

5.14	Knuckleprint Quality Estimation. Top, Middle, Bottom Images for each Proposed Quality Parameter.	113
5.15	Enhanced Knuckleprint	114
5.16	Original and Transformed (<i>vcode</i> , <i>hcode</i>) for Knuckleprint ROI's . . .	114
5.17	Illumination Invariance of <i>LGBP</i> transformation. First row shows same image under five different illumination conditions. Second row shows their corresponding <i>vcode</i> 's	115
5.18	Knuckleprint Recognition	116
5.19	Some Images from Knuckleprint Database [56] used in this work . . .	117
5.20	Failed Knuckle ROI detection	120
5.21	Parameterized ROC Analysis of the Proposed System for PolyU Knuckleprint Database. First 50 subject's left index images are used. (only <i>vcode</i> matchings)	121
5.22	Performance of the Proposed System over Knuckleprint PolyU Database	122
6.1	Overall Architecture of the Proposed Palmprint Recognition System .	124
6.2	Palmprint ROI Extraction (Images are taken from [9])	124
6.3	Palmprint Image Enhancement	125
6.4	Original and Transformed (<i>vcode</i> , <i>hcode</i>) for Palmprint ROI	126
6.5	Steps of the Palmprint Recognition System	127
6.6	Sample Palmprint Images from Casia and PolyU Databases	130
6.7	Vertical and Horizontal Information Fusion based Performance Boost-up for CASIA Palmprint Databases (<i>X</i> – axis in <i>Log scale</i>)	132
6.8	Vertical and Horizontal Information Fusion based Performance Boost-up for PolyU Palmprint Databases (<i>X</i> – axis in <i>Log scale</i>)	133
7.1	Sample Images from all Databases (Five Distinct Users)	137
7.2	Genuine Vs Imposter Best Matching Score Separation Graphs	143

7.3 *ROC* Characteristics Comparison of the Unimodal Vs Multimodal
Databases for the Proposed System 150

List of Algorithms

4.1	Pupil Segmentation	63
4.2	Iris Segmentation	66
4.3	Eyelid Detection	76
4.4	Eyelash Detection	78
4.5	Occlusion Mask Determination	79
4.6	$CIOF(Iris_a, Iris_b)$	86
5.1	Knuckleprint ROI Detection	105
5.2	Uniformity based Quality Attribute (S)	110
5.3	$CIOF(knuckle_a, knuckle_b)$	118
6.1	Palmprint ROI Extraction	125
6.2	$CIOF(palm_a, palm_b)$	129

List of Abbreviations

CLAHE	Contrast Limited Adaptive Histogram Equalization
AUC	Area Under ROC Curve
CMC	Cumulative Matching Characteristics
CRR	Correct Recognition Rate
EER	Equal Error Rate
EUC	Error Under ROC Curve
FAR	False Acceptance Rate
FMR	False Match Rate
FNMR	False Non-Match Rate
FRR	False Rejection Rate
GAR	Genuine Acceptance Rate
ICA	Independent Component Analysis
IITK	Indian Institute of Technology Kanpur
PCA	Principal Component Analysis
ROC	Receiver Operating Characteristics
ROI	Region of Interest
SIFT	Scale Invariant Feature Transform
SURF	Speeded Up Robust Features
LDA	Linear Discriminant Analysis
DCT	Discrete Cosine Transform

POC	Phase Only Correlation
BLPOC	Band Limited Phase Only Correlation
LGBP	Local Gradient Binary Pattern
LOG	Laplacian of Gaussian
DI	Discriminative Index
GvI Graph	Genuine Vs Imposter Graph
FTE	Failure to Enroll Rate
LBP	Local Binary Pattern
EBGM	Elastic Bunch Graph Matching
NIR	Near Infra Red
SVM	Support Vector Machine
DFT	Discrete Fourier Transform
IDFT	Inverse Discrete Fourier Transform
HMM	Hidden Markov Model
CCD	Charged Coupled Device
SOTA	State of the Art
vcode	Vertical code
hcode	Horizontal code
CG	Curvature Gabor filter
JNB	Just Noticeable Blur
CIOF	Corners having Inconsistent Optical Flow

Chapter 1

Introduction

Personal authentication plays an important role in the society. It requires at least some level of security to assure the identity. Security can be realized through one of the three levels.

1. **Level 1 [Possession]** : The user possesses something which is required to be produced at the time of authentication. For example, key of a car or room.
2. **Level 2 [Knowledge]** : The user knows something which is used for authentication. For example, PIN (personal identification number), password, or credit card CVV (card verification value) .
3. **Level 3 [Biometrics]** : The user owns certain unique physiological and behavioral characteristics, known as biometric which are used for authentication. For example, face, iris, fingerprint, signature, gait.

There are some cases where more than one level of security are used to enhance the accuracy of any authentication system. However, there are drawbacks in Level 1 and Level 2 security. For example, key or smart-cards may be lost or mishandled while passwords or PIN may be forgotten or guessed. Since both possession and

knowledge are not intrinsic user properties, they are difficult to be managed by the user. But this is not the case with Level 3 security which is based on biometrics which can be considered as the science of personal authentication using the physiological (*eg.* fingerprint, face, iris, etc.) and behavioral characteristics of human beings (*e.g.* signature, gait, voice, etc.). Examples of some well known biometric traits are shown in Figs. 1.1.

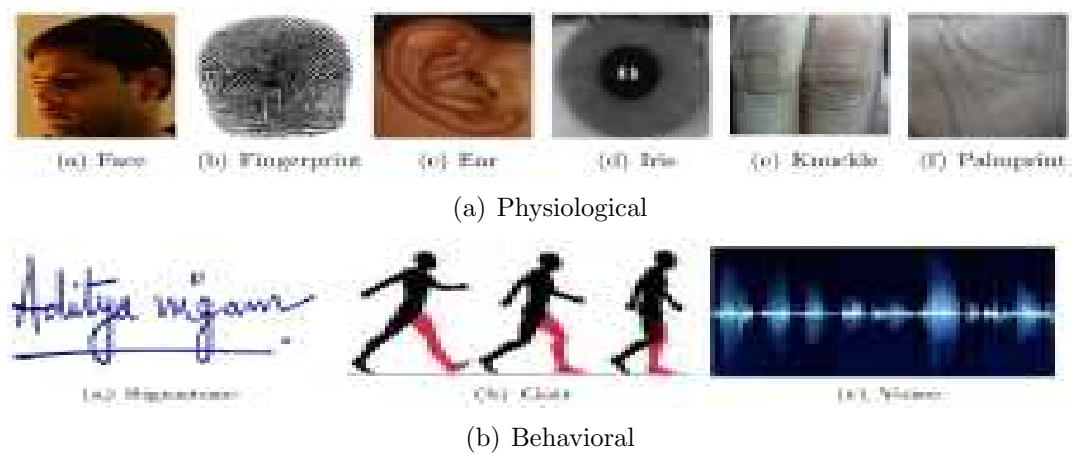


Figure 1.1: Some Biometric Traits

Any biometrics based authentication system is better than the traditional possession or knowledge based system because of the following reasons.

- Biometric traits are intrinsically related to the user. They cannot be lost, forgotten or misplaced; hence they are easy to manage.
- There is a need of physical presence of the trait for authentication.
- Features characteristics are unique.

Some of the vital properties that any biometric trait should possess are given below.

1. **Uniqueness:** Characteristics associated with the biometric trait should be different for everyone.
2. **Universality:** The biometric trait should be owned by everyone and should not be lost.
3. **Circumvention:** The biometric trait should not be spoofed or forged easily.
4. **Collectability:** The biometric trait should be able to acquire by some digital sensor.
5. **Permanence:** Characteristics associated with the biometric trait should be time invariant (temporally stable).
6. **Acceptability:** The biometric trait should be accepted by the society without any objection.

A biometric based personal authentication is a multi-staged process. In the initial stage, the raw image is captured using an acquisition sensor. This is very critical and important stage because accuracy of any biometric system is highly dependent on the quality of images. In the second stage, the desired part from the image, termed as region of interest (ROI), is extracted from the acquired image. Third stage estimates the quality of the ROI. If the quality of the ROI is poor, then one may go for re-acquisition of the image. In next stage, the ROI is preprocessed using some enhancement technique. Some transformations are also performed to get the robust ROI. Discriminative features from the enhanced ROI are extracted in the next stage. Finally, features of a query image have matched against those of image(s) in the database to authenticate the claim.

1.1 Biometric Traits

There does not exist any biometric trait which satisfies all desired properties strictly. For example, facial features are not permanent throughout the life span, fingerprints are not visible for hard working people *etc.* However, there exist several well known biometric traits which satisfy more or less all biometric properties. Biometric traits can be divided based on physiological and behavioral characteristics.

1.1.1 Physiological based Traits

This subsection discusses some of the well known biometric traits which are based on physiological characteristics. These traits are face, fingerprint, ear, iris, palmprint and knuckleprint.

- **Face :** It is one of the most common and well known biometric traits. Images can be captured from distance and even can be extracted from video frames. In a typical face recognition system, initially face is detected from a test image and features are extracted. These features are matched against those stored in the database. An appropriate matching algorithm is used to obtain the matching score. Most commonly geometric distances between facial key-points such as eyes, nose, mouth. There are several real time applications such as surveillance, criminal identification, access control management where it is being used. Face recognition is non-intrusive but due to several challenges like pose, illumination, occlusion, aging and expression, its performance is found to be restricted.
 - **Advantages :** Face is the most common and non-intrusive trait and hence, can be captured easily using cheap sensors. It is widely acceptable in the society.

- **Challenges :** The face pose varies with the viewing angle along with illumination. The facial expressions can deform the face significantly while partial occlusion may hide some facial regions. Aging is a big challenge to deal with because facial features do not vary in a specific pattern.
- **Fingerprint :** For quiet a long time, fingerprints are being used for personal authentication. Any typical fingerprint is made up ridges. There exist huge amount of discriminative textures and patterns such as loop, arch, whorl over a fingerprint. The ridge ending and the ridge bifurcation are known as minutia features. These features are assumed to be unique and stable. Several minutia based fingerprint matching algorithms are proposed. This type of algorithms uses the co-ordinates of minutiae point along with its orientation. Fingerprint sensors are easily available but the good quality fingerprint is a major challenge. The poor quality of fingerprints may be due to poor quality of sensor or external factors such as dirt, oil, sweat *etc.* It is also observed that laborers possess poor quality fingerprints due to their nature of work.
 - **Advantages :** Fingerprints are unique. Lesser amount of user cooperation is required for its acquisition and can be captured through cheap sensors.
 - **Challenges :** The major challenge is to get good quality fingerprints.
- **Ear :** Like other biometric traits, it contains robust, unique and discriminative line based features. In an ear recognition system, ear is segmented from the raw profile face image. Features obtained from ear are matched against those that are stored in database. The major disadvantage of ear is the occlusion which occurs due to hair or any other foreign body such as ear ring, cap, ear phones *etc.*

- **Advantages :** Similar to face, ear can also be acquired non-intrusively using cheap sensors. They are universal and have robust shape that do not vary too much. The social acceptance of ear is high.
 - **Challenges :** Ear recognition performance suffers in varying illumination, pose and translation. The scale and external body occlusion like hair and ear rings are other challenges to deal with.
- **Iris :** Iris is considered as one of the best known biometric traits. It is basically a donut shape annular region that is bounded by sclera and pupil. There exist discriminative textures within iris in the form of furrows, ridges, crypts. It is difficult to capture iris in visible light as it is sensitive to light. Hence, iris acquisition is captured in *NIR* (Near Infra-Red) light in high resolution. Iris is segmented and normalized into a fixed size rectangular strip. There exist several texture based techniques to extract binary features which are matched using hamming distance for authentication. The iris based recognition systems are usually found to be very accurate and robust. But iris can be spoofed through contact lense. The major problem for iris is that it requires stringent user cooperation during acquisition. Also, iris is very sensitive to any external stimulus and it is very hard to control it.
- **Advantages :** Iris possesses highly discriminative unique texture that is naturally well protected. They are difficult to alter and faster to process. Iris images can be acquired touchlessly.
 - **Challenges :** Accurate iris segmentation in varying illumination is very challenging. The eyelid and eyelash along with motion blur and specular reflection is another issue. Off-angle iris recognition is also a very challenging problem.

- **Palmprint :** The inner part of a palm image is considered as palmprint. It includes ridges, minutia, principle line, delta points and rich palmprint texture in abundance. These features are assumed to be stable and unique. Binary features are extracted using several textures as well as statistical and structural properties. Stability of palmprint features is not yet critically studied.
 - **Advantages :** Palmprint can be captured using the low cost sensors in a touch-less manner. The extracted palm ROI is large and contains discriminative and unique features.
 - **Challenges :** Variation of illumination and rotation as well as translation and handling the problem of occlusion are the major challenges.

- **Knuckleprint :** The outer part of a finger is considered as finger knuckle. This can be acquired through any sensor. The line based structural features can be extracted from them and are assumed to be discriminative features. Several gabor based texture and orientation based techniques are used to extract binary features.
 - **Advantages :** It is naturally well protected and can be acquired using low cost sensors. Unique and discriminative features are available over knuckleprint ROI.
 - **Challenges :** Major challenges are the ways to handle the problem of illumination variation as well as rotation and translation.

1.1.2 Behavioral

Some of the most popular behavioral biometric characteristics are discussed below.

- **Gait :** It is one of the behavioral biometric traits. It considers the characteristics that are lying on the way that a person walks. Gait data can be acquired

using moving light displays or video streams. Further, there are sensors that can record various crucial parameters such as pressure and step patterns that can be used for identification.

- **Advantages :** It can be acquired non-intrusively and from distance; hence its user acceptance is good.
 - **Challenges :** Major challenges are the way of handling variations due to background, clothing or walking surface.
- **Signature :** The hand-written signature of a person is an instance of personal verification. Generally it is used for verification of the owner of bank cheques or other off-line documents. From any signature, the orientation and co-ordinate based features in X and Y directions are extracted. They are matched with the features that are already available in the existing database of the claimed identity. General features such as writing angle, breakpoint and curvatures are termed as static while pen-speed, writing time, pressure applied are termed as dynamic features. There are two modes in which such system works, one is on-line while other is off-line. Image of the off-line signature is obtained by scanning handwritten signature while digital signature is acquired through digital signature pad or tablet. It is not universal as illiterate persons do not know how to sign. It is not permanent as it can vary with time and can be spoofed/forged easily.
 - **Advantages :** It has well acceptance socially.
 - **Challenges :** Signature can vary due to aging, emotion or writing surface posing big challenge to automated signature recognition.
 - **Voice :** It considers how a person makes sounds while speaking. It is believed that every person has its own natural texture and tonal quality that depends

on nasal tone, cadence and inflection. Several voice based characteristic are extracted and used for voice based authentication. Features are not permanent and can be imitated/spoofed easily. It is not universally owned as dumb persons cannot speak anything.

- **Advantages :** It is well accepted by the society.
- **Challenges :** Voice suffers from aging, emotion and other environmental variation severely.

1.2 Modes of Biometric System

There are three different possible modes in which any biometric system can be operated and they are enrollment, verification and identification. Every user of the system needs to be enrolled to the system by providing images of the biometric trait. Features are extracted from the images and are stored in the database. In case of verification or identification, features of the query image are matched against those of the enrolled users.

1.2.1 Enrollment

In this step, a user enrolls or registers to the existing database. A biometric sensor is used to acquire the image from the user and its quality is evaluated. If the quality is above than a threshold set a priori features are extracted and a unique identification number is assigned to it. Otherwise, image is re-captured. This process of capturing is repeated until the desired quality image is captured. The process of enrollment subsystem is shown in Fig. 1.2.

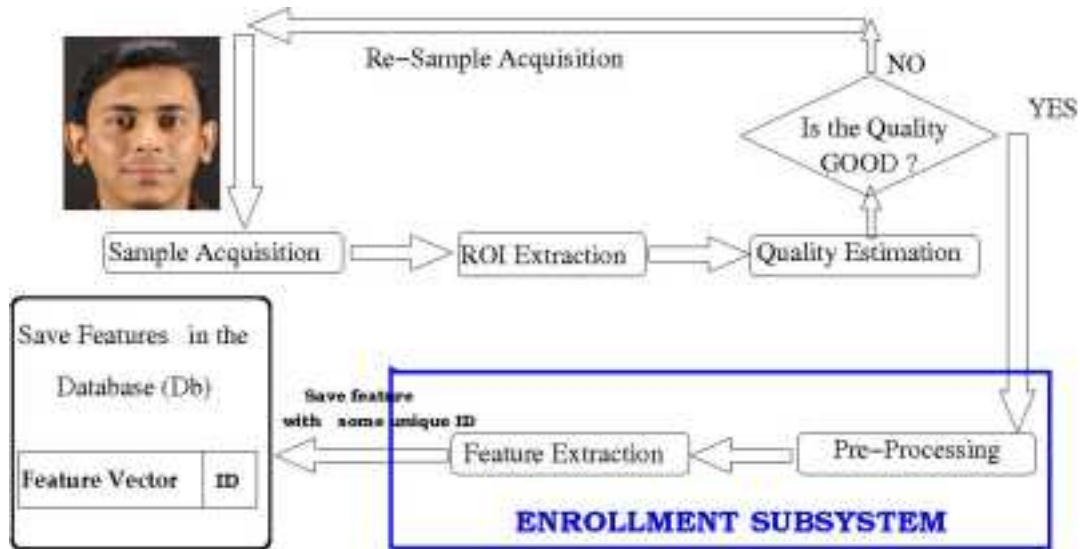


Figure 1.2: Flow Diagram of Enrollment Process

1.2.2 Verification

It is also known as *One-to-One* (i.e **1:1**) matching. In this mode, user claims an identity and the system verifies the correctness of the claim. Features from the biometric trait provided by the user are matched with the features of the claimed identity stored in the existing database. If the similarity matching score is more than a pre-computed threshold, then the claim is verified and the user is considered as a *genuine* user. Otherwise, the claim is rejected and the user is an *imposter*. The flow diagram of the verification subsystem is shown in Fig. 1.3.

Suppose, F_1 and F_2 are the feature vectors of a biometric trait of two subjects, s_1 and s_2 . By the term “Matching between s_1 and s_2 ”, we mean the similarity or dissimilarity between their feature vectors F_1 and F_2 . One can make use of any distance measure to obtain the similarity or the dissimilarity score between the two feature vectors. Without any loss of generality, let us assume that the distance measure provides the similarity score. If the score is greater than a predefined threshold then we can conclude that the two images are matched (genuine); otherwise they

are not matched (imposter).

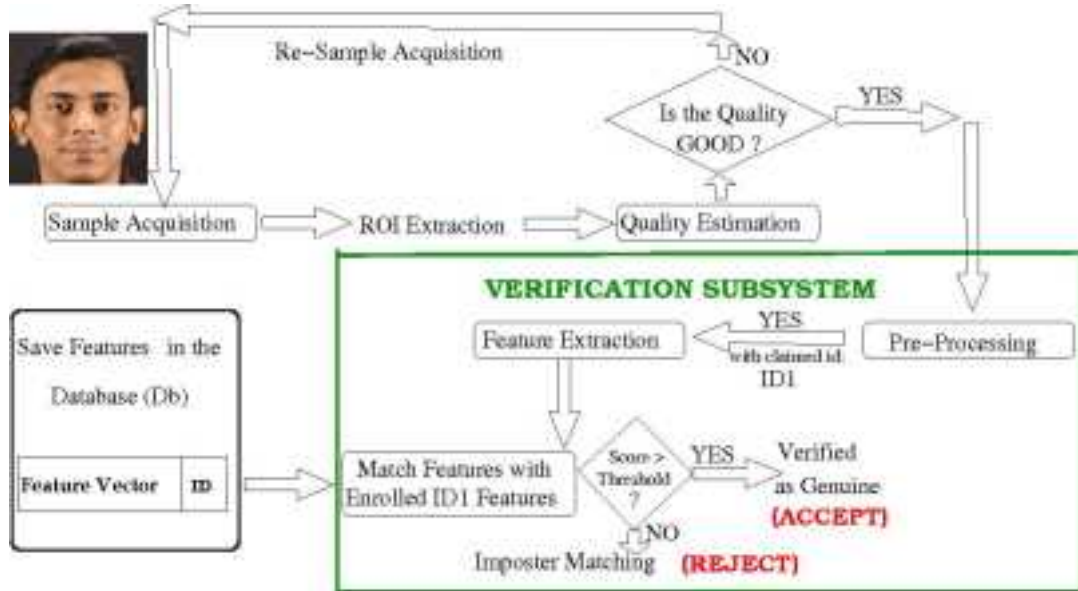


Figure 1.3: Flow diagram of Authentication Process

1.2.3 Identification

It is also known as *One-to-Many* (i.e. **1:N**) matching. In this mode, the system may not have any information other than the presented biometric trait. It attempts to determine the correct identity of that user; hence it is termed as Identification. The ROI of biometric image is preprocessed and features are extracted. The feature vector is matched with feature vectors of all users in the database and the top best matches are obtained.

More clearly, let F_1 be probe features of a biometric trait. The matching score may be computed using a variety of distance metrics to obtain the similarity or the dissimilarity scores between F_1 and all feature vectors that are stored in the database. Out of all these scores, the best N matching images are reported as N probable matches. The identification subsystem is shown in Fig. 1.4.

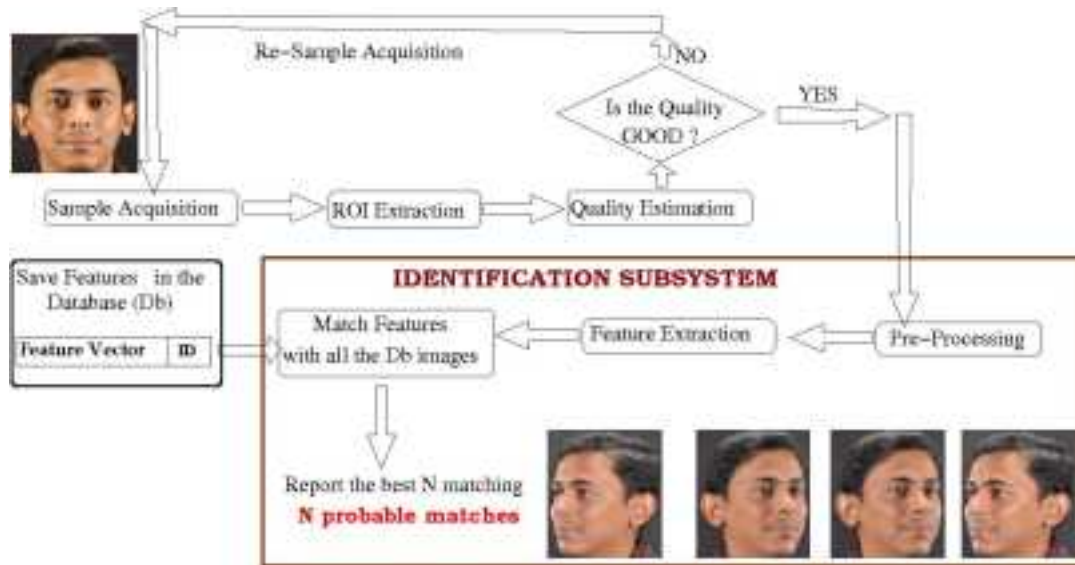


Figure 1.4: Flow Diagram of Identification Process

1.3 Multi-biometric System

The performance of any unimodal biometric system is often got restricted due to variation and uncontrolled environmental condition, sensor precision and reliability as well as several trait specific challenges such as pose, expression, aging etc for face. Moreover, it considers features to take decision on matching and hence, it is difficult to improve its accuracy. Hence one can explore the possibility of fusing more than one biometric samples, traits or algorithms. This is termed as multi-biometrics [16]. There exist different types of multi-biometric system. Some of them are discussed below.

1.3.1 Types of Multi-biometric System

Any biometric based authentication system consists of several stages and has many challenges and limitations. The aim of any multi-biometric system is to improve the performance of the system.

- **Multi-sensor System :** It considers images of same biometric trait where images are captured with the help of multiple sensors. Fig. 1.5 shows three types of fingerprint scanners which can be used to build a multi-sensor biometric system. These three sensors use using different technologies to acquire data and hence the quality as well as discriminative features of their samples are significantly different.



Figure 1.5: Fingerprint Sensors

- **Multi-algorithm System :** It considers multiple matching algorithms to improve the performance of the system. Images of the selected trait are captured using single sensor. In Fig. 1.6, it is shown that one can use different algorithms applied over the same image. One algorithm may be using some global texture like orientation field features while other one may use minutia based local features. Fusion of these matchers is expected to perform better than any of these two algorithms.
- **Multi-instance System :** It considers more than one image of the same trait per user. Multiple samples are collected. In Fig. 1.7, three samples of the same finger collected under controlled environment are shown. This redundant information is useful to address the issues related to local as well

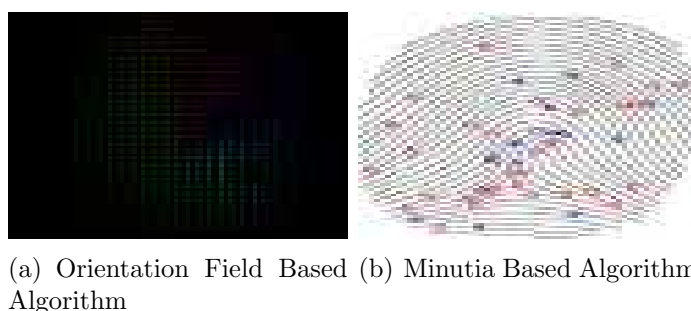


Figure 1.6: Two Fingerprint Matchers (Multi-algorithm)

as environmental condition variations.



Figure 1.7: Samples of Same Fingerprint (Multi-instance)

- **Multi-modal System** : It considers multiple biometric traits for authentication. Uncorrelated traits are considered to achieve better performance [34]. Also it makes system more robust against spoofing attacks as it becomes more and more difficult to imitate all selected traits at-once. But still print-attack and spoof-attack may circumvent these systems [33]. Hence trait selection with better spoofing algorithms is desirable. In Fig. 1.8, a multi-modal system is shown in which face, fingerprint, ear, iris and palmprint samples are used.

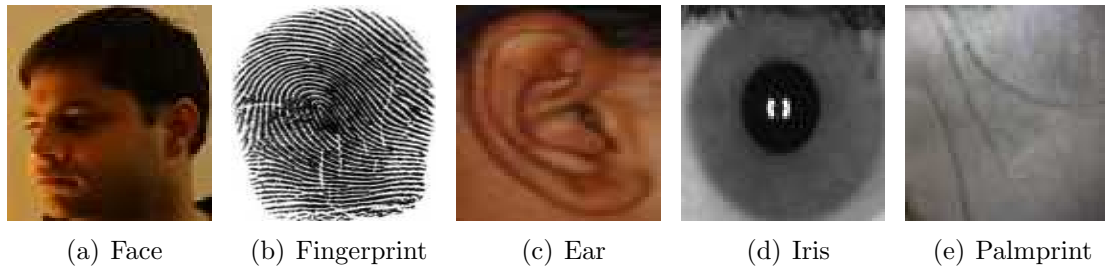


Figure 1.8: Five different Biometric Traits (Multi-Modal)

1.3.2 Fusion Levels

There are several ways that can be used to fuse various characteristics in a multi-biometric system. Fusion can be done at various levels which are discussed below.

- **Score Level :** Samples of different traits are matched with their corresponding trait individually and scores are obtained. Scores are normalized to same scale and converted into either dissimilarity or similarity. These scores are combined to obtain the fused score. There exist several score level fusion techniques such as *max*, *min*, average or weighted average. For example, let a face similarity score be 91 in a scale of [0 to 100] and an iris dissimilarity score be 0.27 in a scale of 0 to 1.0. Either face score should be scaled to [0 to 1.0] and converted into dissimilarity (*i.e* $1 - \frac{91}{100} = 0.09$), or iris score should be scaled to [0 to 100] and converted into similarity (*i.e* $100 - 0.27 * 100 = 73$), before fusion hence for fusion of face and iris, one can use weighted average of either 91 and 73 or 0.09 and 0.27 scores.
- **Feature Level :** All features from each trait are first extracted individually for every subject. These features should be of the same type and are concatenated into one single multi-biometric template which is used for authentication. For example, *LBP* based histogram features extracted from face and iris images can be fused by concatenating both histograms one after the

other to obtain a single histogram. The χ^2 dissimilarity measure can be used to obtain the fused multi-modal matching score.

- **Decision Level :** All samples of different traits are matched with their corresponding trait to obtain individual scores. These scores are thresholded to obtain individual decision for each trait. The final decision is taken by fusing them using *OR*, *AND* or other rules. For example, for face, iris and palmprint traits let the individual decisions be *Face = Accept*, *Iris = Reject* and *Palmprint = Accept*. Simple rules like at-least 2 *Accept* for matching can be used to make the decision.

1.4 Motivation of Thesis

There exist several potentially viable physiological and behavioral biometric traits. Each biometric trait has its own unique and complex anatomical structure. The dynamics of this structure accounts to the discriminative power as well as its stability.

1.4.1 Iris

It is a ring made up of tissues. The detailed iris related anatomical features are described in [12] and are shown in Fig. 1.9(a). Thin circular diaphragm between cornea and lens is called as iris which has abundance of micro-textures as crypts, furrows, ridges, corona, freckles and pigment spots. These textures are randomly distributed; hence they are believed to be unique [32]. Iris texture is very fine and most of its details are developed during the embryonic development. Textures of two subjects are believed to be unique and even the right eye of the same subject is different from the left eye [21]. Iris is a naturally well-protected biometric as compared to the other traits and is also assumed to be invariant to age.

Issues such as iris occlusion due to eyelid and eyelashes and specular reflection remain to be addressed. Also accurate iris localization is a challenge. Huge amount of efforts are required to improve the accuracy and reliability of any iris based system. Estimating the iris quality is also an important issue that has to be resolved. In this thesis, we have addressed some of these issues.

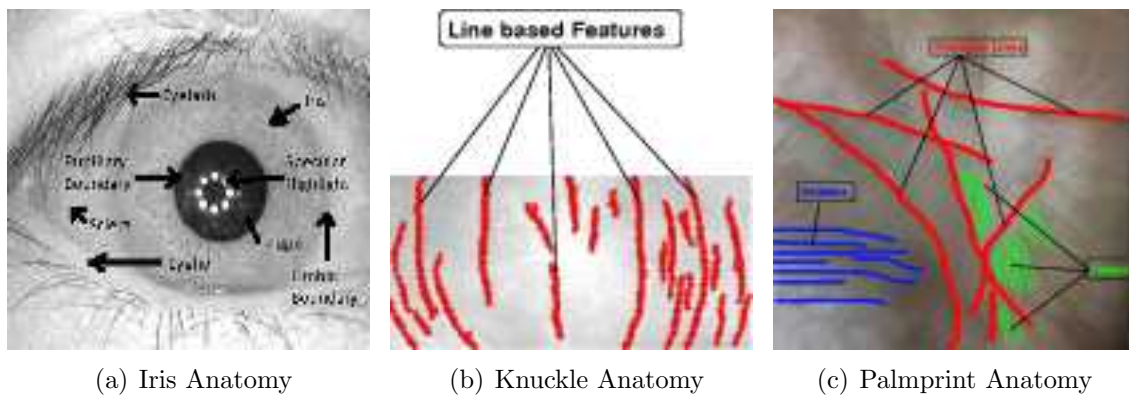


Figure 1.9: Iris, Knuckle and Palmprint Anatomy

1.4.2 Knuckleprint

Anatomical structure of the knuckleprint is shown in Fig. 1.9(b). The line like (*i.e.* knuckle lines) rich pattern structures in vertical as well as horizontal directions exist over it knuckleprint. These horizontal and vertical pattern formations are believed to be very discriminative [80]. The knuckleprint texture is developed very early and last very long because it occurs on the outer side of the hand and no one can use them for almost any work except boxers. Negligible wear and tear as well as print quality degradation with time and age are observed. Its failure to enrollment rate is also expected to be very low as compared to the fingerprint and it does not require much user cooperation.

Since it is a very new trait, there exist several challenges that have to be ad-

dressed. The central knuckle line extraction is a major issue that is required to register knuckleprints. There is a need to design a reliable feature selection as well as knuckleprint matching algorithm. Estimating the quality of a knuckleprint is a challenge that requires significant attention. This thesis has addressed some of these issues.

1.4.3 Palmprint

The inner part of the hand is called as palm and the extracted region of interest in between fingers and wrist is termed as palmprint which is shown in Fig. 1.9(c). Even monozygotic twins are found to have different palmprint patterns [37]. Pattern formation within this region is supposed to be stable as well as unique [9]. Huge amount of textures in the form of palm-lines, ridges, wrinkles *etc.* is available over palmprint as shown in Fig. 1.9(c). Prime advantage of palmprint over fingerprint includes its higher social acceptance because it is never being associated with criminals. It has larger ROI area as compared to fingerprint images that ensures abundance of structural features including principle lines, wrinkles, creases and texture pattern. Due to larger *ROI*, even low resolution palmprint images can be used to enhance system's speed but to reduce the cost.

There are several challenges that are to be addressed. The accurate palmprint localization is one of the key issue that is required to extract registered palmprints. One needs to design reliable features selection as well as palmprint matching algorithm. Methods of computing the quality of a palmprint is a challenge that requires significant attention. This thesis has dealt with some of these issues.

1.4.4 Multi-biometrics

A comparative study between iris, knuckleprint and palmprint is presented in Table 1.1. It has been observed experimentally that such a fusion of two or more biometric

Property	Meaning	Iris	Palmprint	Knuckleprint
Universality	Every individual must possess	M	M	M
Uniqueness	Features should be distinct across individuals	H	M	M
Permanence	Features should be constant over a long period of time	H	H	H
Collectability	Trait can be easily acquired	L	M	H
Performance	Possess high performance	H	M	M
Acceptability	Acceptable to a large percentage of the population	L	M	H
Circumvention	Difficult to mask or manipulate	M	M	H

Table 1.1: Biometric Properties (L = *Low*; M = *Medium*; H = *High*)

modalities facilitates the system to reject the imposters much more confidently and hence boosting the overall system performance significantly. Most of the state-of-the-art uni-modal biometric based authentication systems perform block by block and pair-wise matching [6], [7], [9], [36], [65], [76]; hence they require pre-registered images. But they cannot produce highly accurate systems.

Any multi-modal system makes use of some biometric traits to enhance system's performance. Multimodal systems are more relevant when the number of enrolled users is very large. The false acceptance rate grows rapidly with the increase in the size of the database [5]; hence multiple traits are used to achieve better performance. Also multi-modal systems can enable us to deal with missing trait. The spoof vulnerability is much lesser than any unimodal system; hence it is ideal for outdoor and non-controlled environments. To best of the knowlegde not much work has been done in this area mainly due to the non-availability of multi-modal datasets. Iris, knuckleprint and palmprint traits have uncorrelated features; hence this thesis has considered these traits for fusion to enhance the system performance. Further, these traits are never used to design a multimodal system in the past. All of them

are well protected and also their textures cannot be altered or deformed easily.

1.5 Performance Analysis Metrics

It is necessary to analyze the performance of any biometric system. The inferences drawn over performance analysis is used in judging the suitability for its application. There exist several performance measures to analyze a verification or identification system.

1.5.1 Verification Performance Metrics

Like any pattern recognition system, there are two types of errors *viz.*; False Acceptance Rate (FAR) and False Rejection Rate (FRR). When two feature vectors are matched, it generates a matching score. This score is either dissimilarity or similarity score. For a dissimilarity (similarity) score, if it is less (greater) than a predefined threshold, we assume, these two feature vectors are matched. FAR is the probability of accepting an imposter as a genuine user wrongly. More clearly, if we perform N distinct imposter matchings and M of them have got accepted wrongly as genuine matching then FAR is given by :

$$FAR = \frac{M}{N} \times 100\% \quad (1.1)$$

Similarly, FRR is defined as the probability of rejecting a genuine user wrongly. That means, if we perform N distinct genuine matchings and M of them have been got rejected wrongly then FRR is given by :

$$FRR = \frac{M}{N} \times 100\% \quad (1.2)$$

For various thresholds, if we plot FAR or FRR , we get a curve which is known

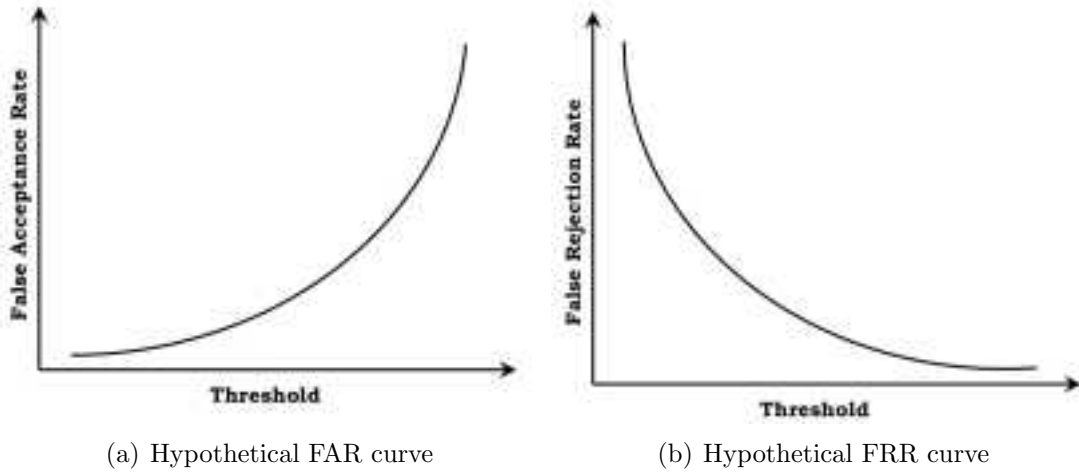


Figure 1.10: Graphical Representation of FAR and FRR

as FAR or FRR curve. Sample FAR and FRR curves are shown in Fig. 1.10.

[a] **EER** : Equal error rate (EER) is the value of FAR for which FAR and FRR are equal. That means, EER is the point of intersection of FAR and FRR curves. Also, if we draw a curve of FAR vs FRR for all thresholds and draw a line at 45° from origin then EER is the point of intersection of that line with the FAR vs FRR curve. It is shown in Fig. 1.11(a).

[c] **Accuracy** : If T is the threshold for which $\frac{FAR + FRR}{2}$ is minimum for all FAR and FRR at different threshold, then we define the accuracy at T as

$$Accuracy = \left(100 - \frac{FAR_T + FRR_T}{2} \right) \% \quad (1.3)$$

where FAR_T , FRR_T are FAR and FRR at threshold T . The threshold (T) at which the combination of FAR and FRR gives the highest accuracy, is considered as the optimum threshold. It can be observed that accuracy may not be maximum at the threshold of EER .

[c] **Receiver Operating Characteristics (ROC) Curve** : It is a graph

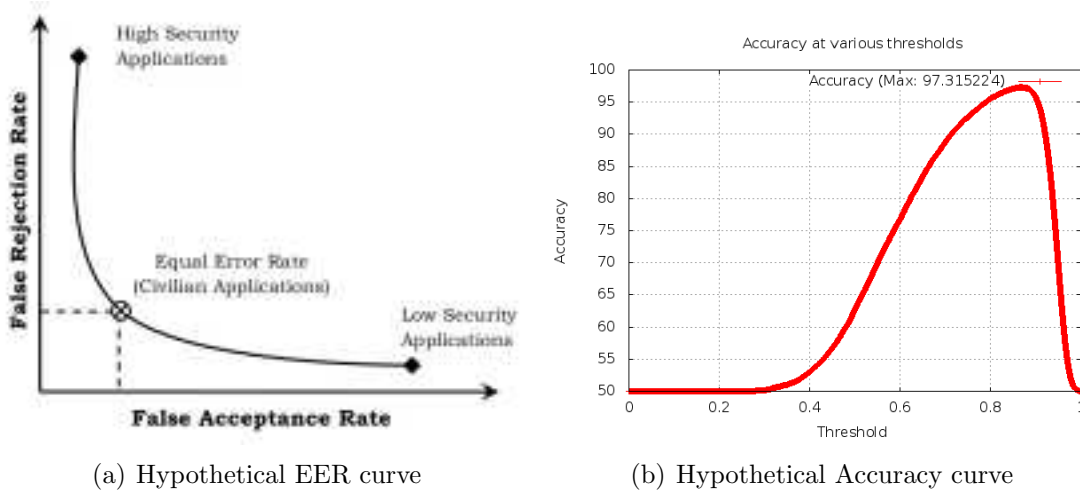


Figure 1.11: Graphical Representation of EER and Accuracy

plotting FAR against various FRR s. It helps to analyze the behavior of FAR against FRR as shown in Fig. 1.11(a). It quantifies the discriminative power of the system between genuine and imposter's score. An ideal ROC curve would include a point at $FRR = 0, FAR = 0$ which signifies $EER = 0$. The curve provides a good way to compare the performance of two biometric systems. Lower the ROC curve (towards both co-ordinate axis) better is the system since area under the curve (*i.e* error) is lesser.

[d] **Error under ROC Curve (EUC)** : It is a scalar quantity defined as the area under the ROC curve. It estimates the amount of error incurred while one makes decision on genuine and imposter matchings.

[f] **Decidability Index** : It measures separability between imposter and genuine matching scores and is defined by:

$$d' = \frac{|\mu_G - \mu_I|}{\sqrt{\frac{\sigma_G^2 + \sigma_I^2}{2}}} \quad (1.4)$$

where μ_G and μ_I are the mean and σ_G and σ_I are the standard deviation of the

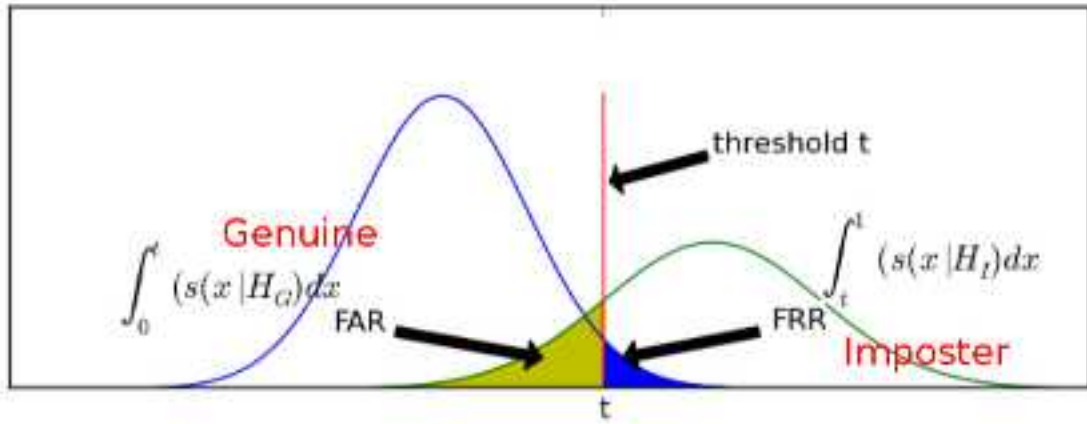


Figure 1.12: Graph Showing Genuine and Imposter Score Distribution (here $\int_0^t (s(x|H_G))dx$ represents the genuine similarity score distribution)

genuine and imposter scores respectively. In Fig. 1.12, the genuine and the imposter score distributions are shown. Higher the value of d' , better is separation between two distributions; hence error is less.

1.5.2 Identification Performance Metrics

For identification, performance analysis is done by correct recognition rate, CRR and genuine vs imposter best match graph.

[a] **CRR** : The correct recognition rate, CRR , is also known as the **Rank 1** accuracy. It is defined as the ratio of the number of correct (Non-false) top best matches and the total number of matching performed in the query set. More clearly, if we have N images in the test set and out of that, M images have got the Non-false top best match then CRR is given by :

$$CRR = \frac{M}{N} \times 100\% \quad (1.5)$$

[b] **Genuine vs Imposter Best Match Graph (GvI Graph)** : The graph which shows separation of genuine *vs* imposter best matching scores plots the best

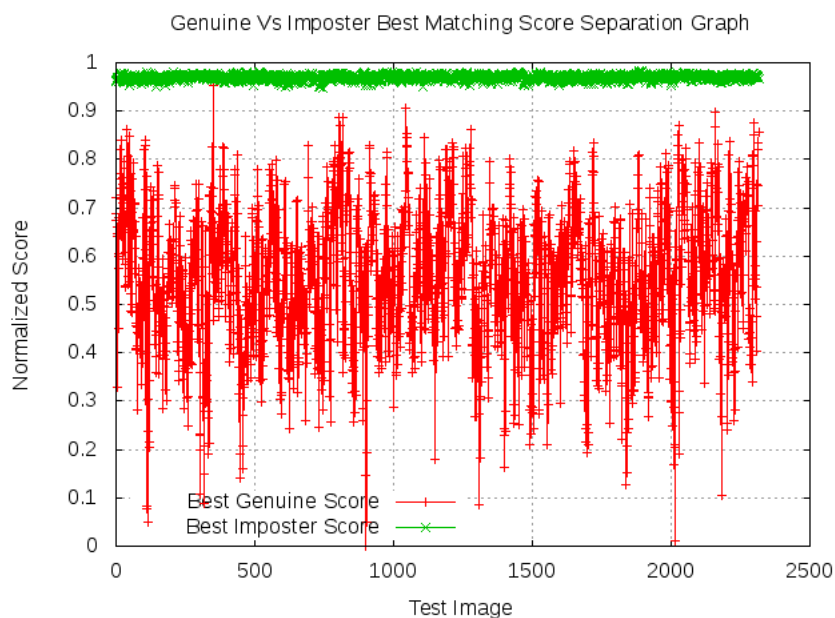


Figure 1.13: Graph showing Genuine Vs Imposter Best Score Graph

genuine and the best imposter scores for all probe images. From the graph, separation between the best genuine and the imposter matching scores can be analyzed visually. In Fig. 1.13, one such plot is shown from which one can observe that genuine matching scores are well separated from imposters and overlapping scores are errors.

1.6 Thesis Contribution

This thesis deals with the problem of designing some efficient biometric systems. It has considered three biometrics traits *viz.* iris, knuckleprint and palmprint. Finally, it has proposed an efficient multimodal biometric system which makes use of three traits. Score level fusion is performed to obtain the matching score of the multimodal system. The contribution of this thesis spans over all stages involved in the development of any biometric system.

1.6.1 ROI Extraction

The data acquisition system captures the biometric samples. It is required to extract the region of interest (ROI) from the acquired samples. We have proposed efficient algorithms to extract the *ROI* from iris, knuckle and palm samples.

1. Iris *ROI* Extraction : It requires the exact localization of inner as well as outer iris boundary. Improved Hough and Integro-differential transformations are used in the way that they can complement to each other to extract the inner and outer boundaries respectively. The iris *ROI* is extracted efficiently by using the modified hough and sector restricted integro-differential transform.
2. Knuckleprint *ROI* Extraction : It contains different type of texture and structure. Gabor filter is modified to Curvature Gabor filters (*CG*) to model the knuckleprint *ROI*. It is used as a template to localize the central phalangeal joint and to segment the knuckleprint *ROI*.
3. Palmprint *ROI* Extraction : The palmprint has a very peculiar and well defined structure. Some landmark key-points such as valley and hill points are used to segment the palmprint *ROI*.

1.6.2 Quality Estimation

The quality of the extracted biometric ROI plays a significant role in the overall performance of any system. Hence, several general as well as trait specific quality parameters are proposed to estimate the quality of any iris, knuckleprint and palmprint sample.

1. Iris Quality Estimation : The quality of an iris sample is modeled as a function of six attributes, namely focus, motion blur, occlusion, contrast and illumination, dilation and specular reflection.

2. Knuckleprint Quality Estimation : The knuckleprint image quality is obtained by computing the amount of well focus edges, amount of clutter, distribution of focused edges, block-wise entropy of focused edges, reflection caused by light source or camera flash and the amount of contrast.
3. Palmprint Quality Estimation : The palmprint image quality is obtained by estimating the amount of three primary features, namely palm principle lines, ridges and wrinkles.

1.6.3 Biometric Feature Enhancement and Transformation

An enhancement algorithm which can be used to obtain robust iris, knuckle and palmprint *ROI* has been proposed. *ROIs* are transformed using the proposed local gradient based binary pattern to obtain highly discriminative as well as robust texture representation.

1.6.4 Biometric Feature Extraction and Matching

A feature extraction and matching algorithm is proposed to perform biometric sample identification/recognition. The discriminative corner features are used for matching. The matching algorithm uses the concept of sparse point tracking but under three constrains *viz.* vicinity, correlation and patch-wise error bounds. The proposed matching algorithm is parameterized and is fine tuned to make the matching.

1.6.5 Multimodal Biometric System

We have proposed an efficient multimodal biometric system using three traits, *viz.* iris, knuckleprint and palmprint. Since same matching algorithm is used to matching iris, knuckle and palm, simple score level fusion is done. To analyze the performance

of the system, we have created several chimeric multi-modal biometric databases. The system is optimized to perform efficiently so that it can be considered as a real-time application. In this thesis we have shown that uncorrelated features of different modalities can be fused to achieve better performance.

1.7 Thesis Organization

This thesis contains eight chapters. A general biometric system with its properties has been discussed in first chapter. Also motivation of the thesis presented.

The literature review on each of the three traits *viz.* iris, knuckleprint, palmprint is presented in Chapter 2. Also, it has presented the some well known work on various multi-modal based biometric system. Some image processing and computer vision based techniques which are used to design our systems have been presented in the next chapter.

In Chapter 4, an efficient iris based recognition system has been proposed. Each iris is efficiently segmented using an improved circular hough transform for inner iris boundary (*i.e.* pupil) detection. The robust integro-differential operator is used to detect outer iris boundary that makes use of the pupil location. If the quality of the acquired iris sample is less than a predefined threshold then the image is recaptured. This early quality assessment is very crucial to handle the problem of poor quality and non-ideal imagery. The segmented iris is normalized to polar coordinates (*i.e.* rectangular strips) and *LGBP* (Local Gradient Binary Pattern) algorithm is proposed to obtain robust features. The corner features are extracted and matched using the proposed dissimilarity measure *CIOF* (Corners having Inconsistent Optical Flow). The system has been tested over publicly available CASIA 4.0 Interval and Lamp iris databases which consist of 2,639 and 16,212 images respectively.

In the next chapter, a knuckleprint based recognition system has been proposed.

The segmentation of the knuckleprint is done by estimating the central knuckle-line. It has used a new modified version of gabor filter to extract the knuckleprint. We have proposed a technique to extract the quality of the acquired knuckleprint sample. If it is less than a predefined threshold then it is recaptured. The segmented knuckleprint ROI is preprocessed using the proposed *LGBP* (Local Gradient Binary Pattern) to obtain robust features. The corner features are extracted and matched using the proposed dissimilarity measure, *CIOF* (Corners having Inconsistent Optical Flow). The proposed system has been tested over the publicly available PolyU knuckleprint database consisting of 7,920 images.

An effective palmprint based recognition system has been proposed in Chapter 6. The palmprint segmentation is done by obtaining the two valley points and then a square shaped ROI is extracted. The quality of the acquired palmprint sample is estimated using the proposed quality assessment parameters and if the quality is less than a predefined threshold, it is recaptured. The segmented palmprint is preprocessed using the proposed *LGBP* (Local Gradient Binary Pattern) to obtain robust features. The *KLT* based corner features are extracted and matched using the proposed dissimilarity measure *CIOF* (Corners having Inconsistent Optical Flow). The proposed system has been tested over publicly available CASIA and PolyU palmprint databases which consist of 4,528 and 7,720 images respectively.

In Chapter 7, an efficient multi-modal based recognition system has been proposed. Four different fused multimodal systems *viz.* iris and knuckleprint, knuckleprint and palmprint, palmprint and iris and finally iris, knuckleprint and palmprint have been proposed and these systems are analyzed on the chimeric databases created by us. Conclusions along with the future scope of work have been presented in the last chapter.

Chapter 2

Literature Review

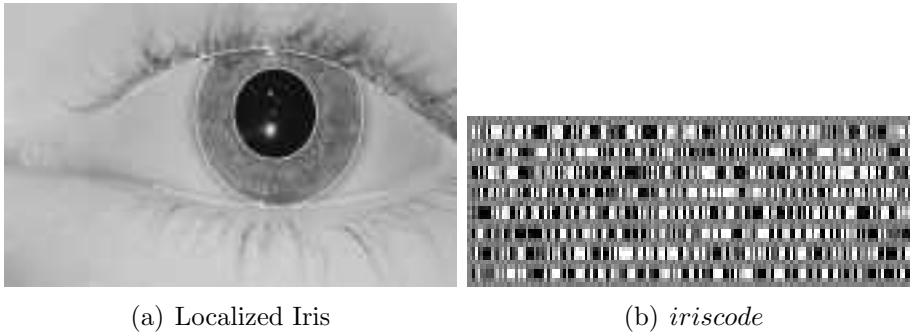
This chapter presents the literature survey on the work carried out on these three traits.

2.1 Iris based Biometric System

The iris ROI should be accurately localized which is challenging due to lot of variation in illumination and other extrinsic factors. The iris sample suffers from dimensional inconsistency among eye images which is caused due to pupil dilation, head movement, eye movement *etc.* Hence, the ROI is normalized to a rectangular strip of fixed size.

The pioneering work in iris recognition system is done by Daugman [19]. The integro-differential operator is used to find circular boundaries by detecting heavy jump or drop in summation of pixel intensities over the circle. The multi-scale quadrature $2D$ gabor wavelet coefficients are used. A binary feature vector (*i.e. iriscode*) of 256 bytes is generated which is shown in Fig. 2.1(a). Feature vectors obtained from two iris images are matched by the hamming distance.

Wildes [69] has used circular hough transform which finds the circle that fits max-



(a) Localized Iris

(b) *iriscode*

Figure 2.1: Images are taken from [19, 18]

imum edge points. Huang *et.al* [31] have used rescaled image to find iris boundaries and have used it to guide the search on the original image. It has improved the approach presented in [69]. The algorithm proposed by Liu *et al.* [42] segments the iris image by ignoring high intensity edge pixels around specular reflections. Lili and Mei [41] have found a coarse location of iris. It is based on the assumption that image histogram has three main peaks and they are due to pupil, iris and sclera. He and Shi [29] have proposed an approach in which image is binarized to locate the pupil. It uses edge detection and circular Hough transform to find the limbic boundary. Feng *et al.* [25] have used coarse-to-fine strategy to find iris boundary and have suggested an improvement to use lower part of the pupil because it is stable even under occlusion. Xu *et al.* [72] have divided the image into grids and have used the minimum mean intensity across the grids as a threshold. It has considered to locate pupil and subsequently the limbic boundary. Zaim *et al.* [74] have used a split and merge algorithm to detect pupil as the connected region of uniform intensity.

Camus and Wildes [13] have presented an algorithm which is based on Daugman's integro-differential operator that searches in cubic space of (x, y, r) . Instead of applying the operator directly taking all points as candidate center points, they have used local minimas of intensity as seed points, making the process faster by

3.5 times as compared to Daugman's algorithm [18]. Actual iris center is examined by measuring the image patch gradient information. Also uniformity is measured across the eight rays passing from the assumed potential center at a $\frac{\pi}{4}^\circ$ angle difference, as shown in Fig. 2.2. It gives an accuracy of 99.5% in case of having no glasses and that of 66.6% with glasses.

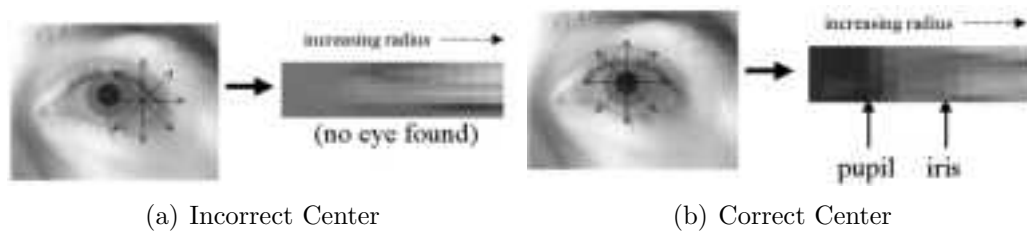


Figure 2.2: Mapping of radial rays into a polar representation pupil and iris boundaries become vertical edges [13]

Bonney *et al.* [11] have extracted pupil by using least significant bit-plane along with erosion and dilation operations. Using pupil area, the standard deviation in horizontal and vertical direction is computed to search for limbic boundary; both boundaries are modeled as ellipses and is shown in Fig. 2.3. This method does not rely on circular edges detection; hence it is not restricted to circular iris.

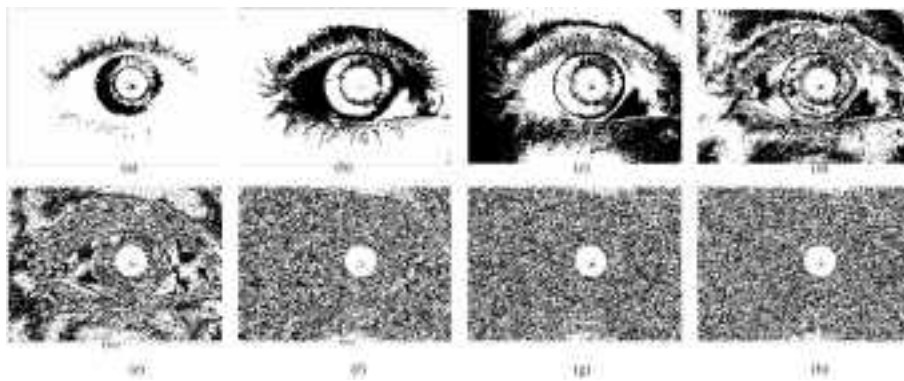


Figure 2.3: (a) Most Significant bit-plane 7 (b) Bit-plane 6 (c) Bit-plane 5 (d) Bit-plane 4 (e) Bit-plane 3 (f) Bit-plane 2 (g) Bit-plane 1 (h) Least Significant bit-plane 0 [11].

In [30], He *et al.* have proposed a Viola and Jones style cascade of classifiers [67] for detecting the presence of pupil region and for optimizing the boundary of pupil. Miyazawa and Ito [50] have thresholded iris image and have used the center of gravity of binary image to find out pupil center followed by ellipse fitting to determine pupil boundary. The iris boundary is modeled as an ellipse and is found using the integro-differential operator. Pupil center is detected using the center of

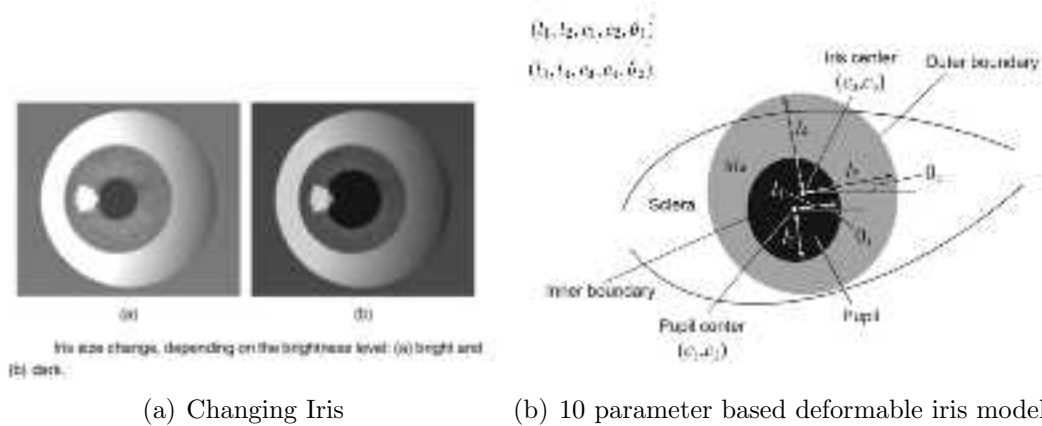


Figure 2.4: Iris Deformable Model [50]

gravity of the binarised image. The two ellipses, as shown in Fig. 2.4 are extracted by computing a parameter based deformable iris model as shown in Fig. 2.4(b). Segmented iris is used to extract features and matching is performed using band limited phase only correlation, (*BLPOC*). Preprocessing of an iris image is shown in Fig. 2.5.

The recent trend in iris segmentation deals with the off-angle images *i.e.* person looking at some angle rather than straight. Dorairaj *et al.* [22] have proposed the global *ICA* encoding for non-ideal iris based recognition. It has used an initial available estimate of angle of rotation and then the integro-differential operator for ellipse has been used for detection and refinement of result. The off-angle image is projected to front-view image. The overview of the proposed scheme is shown in Fig. 2.6(b).

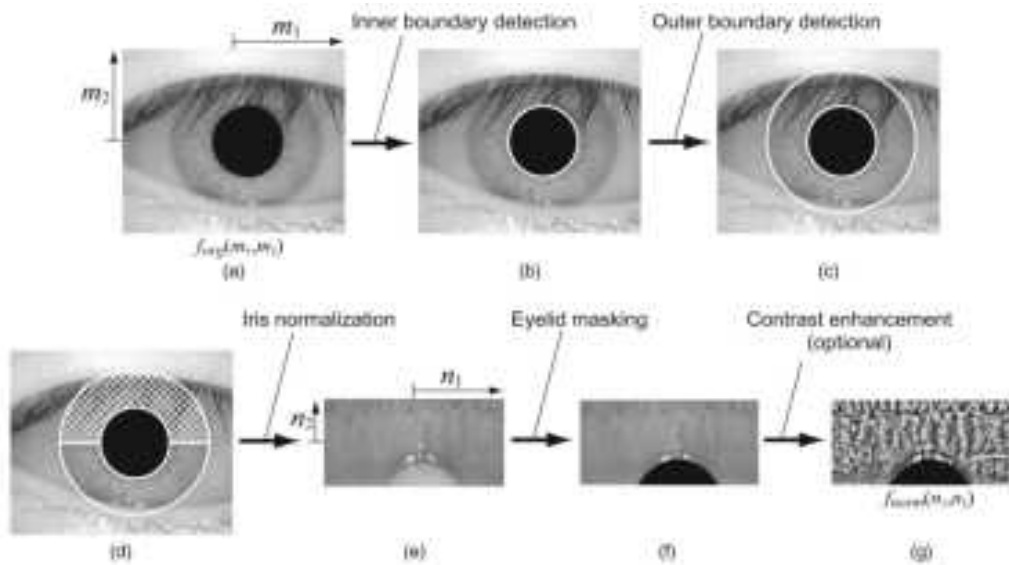


Figure 2.5: Iris Image Preprocessing [50] : (a) Original Image, (b) Detected Inner Boundary, (c) Detected Outer Boundary, (d) Lower Half of Iris, (e) Normalized, (f) Eyelid Masking and (g) Enhanced Image

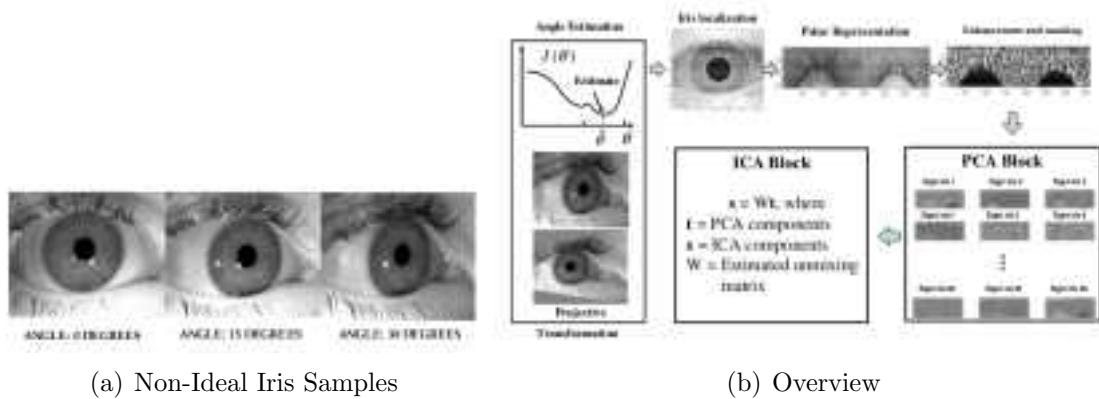


Figure 2.6: Overview of Non-ideal Iris Recognition System [22]

Li *et al.* [40] have fitted an ellipse to pupil boundary and have used rotation and scaling to transform it to circular boundary. It is shown that this calibration improves the intra-class and inter-class separation that is achieved by Daugman-like recognition algorithm [19].

One of the major factors that reduces the iris quality significantly is off-angle.

It is almost impossible to give iris data without any off-angle. Abhyankar *et al.* [2] have proposed an approach involving bi-orthogonal wavelet networks for non-ideal imagery. Non-ideal and poor quality iris imaging may cause irrecoverable loss of information as iris segmentation starts to behave erroneous. The circle fitting algorithm performs very poorly when one attempts to segment off-angle images, as shown in Fig. 2.7. Some projective geometry and affine transformations are used

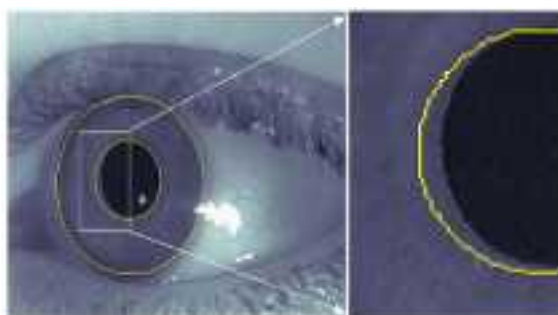


Figure 2.7: Off Angle Iris Segmentation [2]

to distribute the radial resolution uniformly in all quadrants. Synthetic iris samples are generated by rotating them at an angle of 10° and 20° . Active shape model (ASM) [3] is used to find elliptical iris boundaries from off-angle images.

In [19], gabor wavelet responses are quantized to generate feature vector and matching is done using hamming distance. The phase demodulation process is used to encode iris patterns. Local regions of an iris are projected onto quadrature 2D Gabor wavelets. The angle of each phase is quantized to one of the four quadrants by setting two bits of phase information as shown in Fig. 2.8(a).

In [69], hough transform is used for iris localization and Laplacian of Gaussian (LOG) is used for matching. In [45], vanishing and appearing of important image structures are considered as key local variations and dyadic wavelets are used to transform 2D image signals into 1D signals to obtain unique features. They have located positions of key variations accurately by easily computable dyadic wavelets. The overview of the system and the dyadic wavelet transformation of any 2D signal

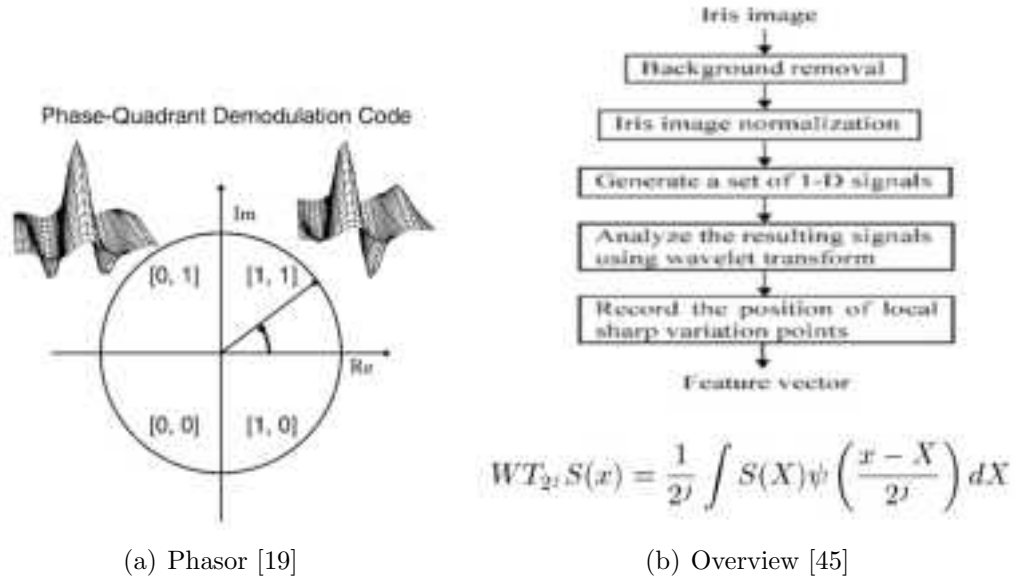


Figure 2.8: Two Most Popular Iris Systems

$(S(X))$ are shown in Fig. 2.8(b). The response is converted into a 1D binary sequence and dissimilarity score is computed using hamming distance for matching.

In [24], gabor wavelet with elastic graph matching is used for iris recognition. In [51], Discrete Cosine Transform (DCT) coefficients are extracted from non-overlapping rectangular blocks at various angles and of variable sizes and are quantized. The binary feature for each rectangular block is computed. Average is done across the width to get a 1D vector that is windowed using the hanning window to suppress the spectral leakage. The DCT is applied over it and the DCT coefficients are used as features. The differences between the DCT coefficients of adjacent patch is binarised to obtain a binary code using zero crossings. Steps involved in feature extraction are given in Fig. 2.9. The hamming distance based matching is performed for score computation.

In [50], Phase Only Correlation (POC) and Band Limited Phase Only Correlation ($BLPOC$) are used for accurate iris recognition. In [60], variational model is applied to localize iris while modified contribution selection algorithm ($MCSA$)

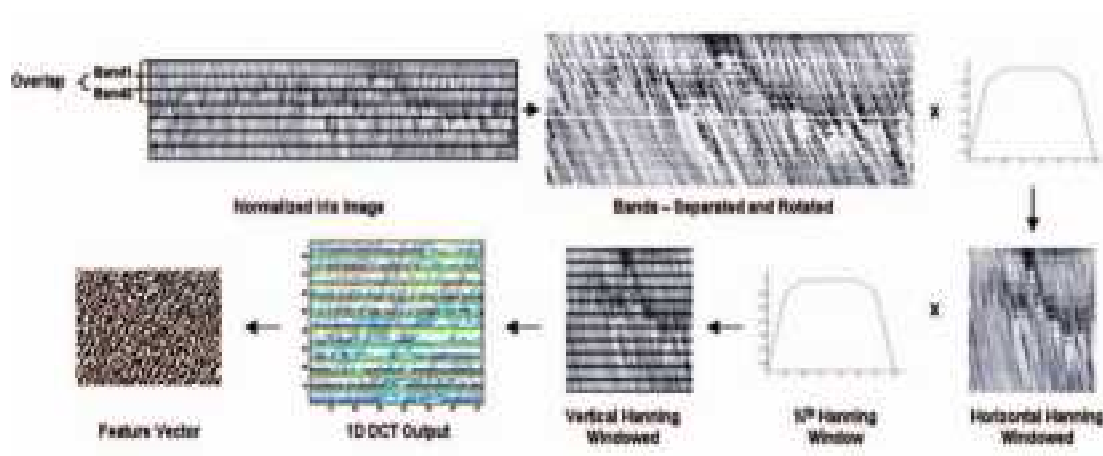


Figure 2.9: Steps Involved for Feature Vector Extraction [51]

is used for iris feature ranking. In [66], compact and highly efficient ordinal measures are applied for iris recognition. The relationship between iris patches selected over the complete normalized iris is considered to be robust and is shown in Fig. 2.10(a). Hence, such ordinal relationships can be used as key signature of the iris patch and this ordinal relationship is encoded as a binary feature. These ordinal relationship between iris patches is efficiently computed using multi-lobe differential filters (MLDF Filters) as shown in Fig. 2.10(b). Also, there are some significant contributions like application of Principle Component Analysis (*PCA*) and Independent Component Analysis (*ICA*) in iris recognition [17], [31]. A comprehensive survey on iris biometrics is available in [12].

2.2 Knuckleprint based Biometric System

The finger knuckleprint is relatively new trait and a limited amount of work has been done. In [77], Zhang *et.al* have extracted the knuckleprint *ROI* using convex direction coding as shown in Fig. 2.11 .

The correlation between two knuckleprints is used for identification. It is calcu-

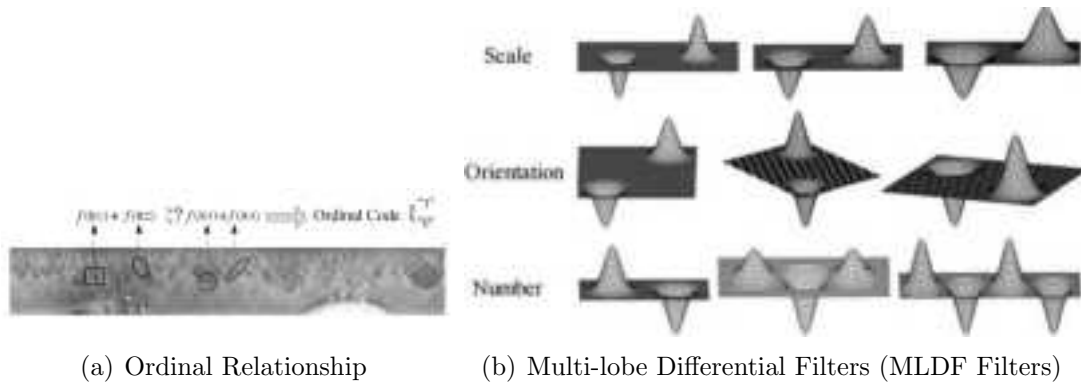


Figure 2.10: Ordinal Measures for Iris Recognition [66]

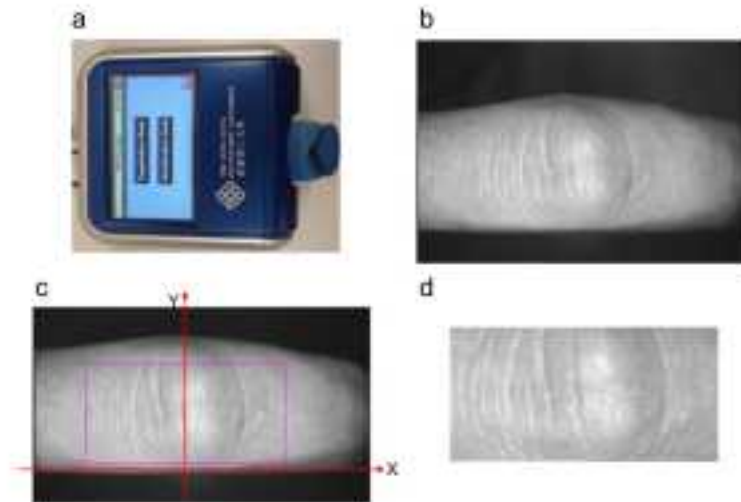


Figure 2.11: Knuckleprint Acquisition System [77], (a) Device, (b) Raw Sample, (c) ROI Localized, (d) Cropped.

lated using band limited phase only correlation (*BLPOC*). The knuckleprints are assumed to possess small range of frequencies and hence, the Fourier based frequency band is restricted and phase only correlation (*POC*) is calculated. The *POC* value between two images can be used as similarity score and is obtained using the cross-spread spectrum of the Fourier transform of both images.

In [52], knuckleprints are enhanced using *CLAHE* to address non-uniform reflection because they can be affected due to noise and improper illumination. There

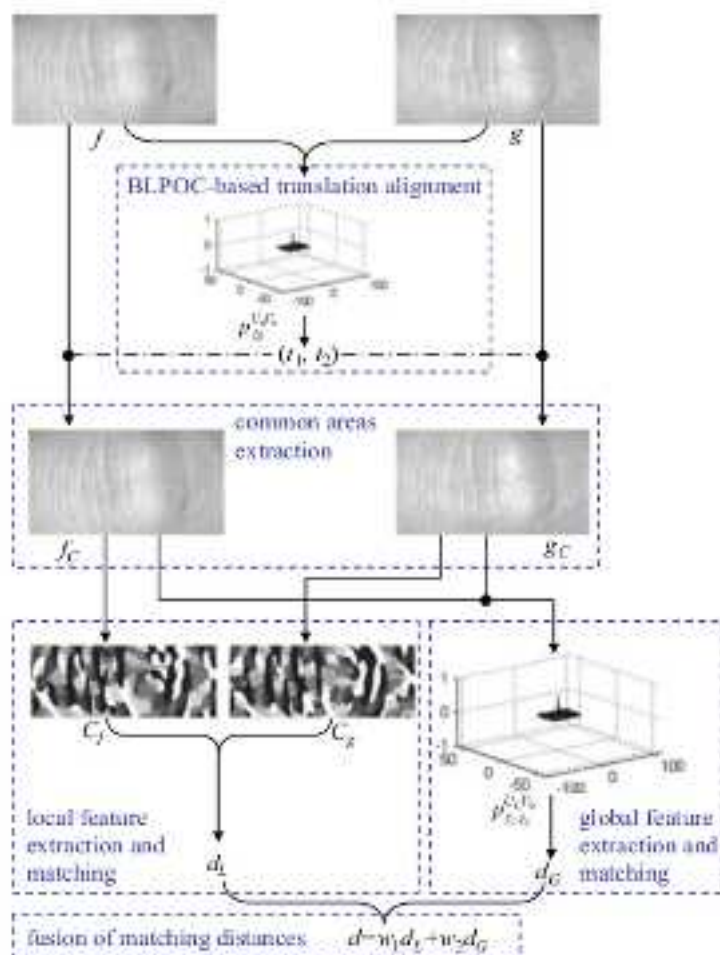


Figure 2.12: Ensemble of Local and Global Features [80]

can be some variation because of scale and rotation; hence, scale invariant feature transform (*SIFT*) key-points can be used for matching. In [71], a knuckleprint based recognition system that extracts features using local gabor binary patterns has been proposed. Gabor filter is applied over a pixel and its neighborhood. A discriminating local pattern is extracted to represent that pixel.

In [80], local and global features are fused to achieve better performance. Global features are extracted by band limited phase only correlation (*BLPOC*) [77] while local features are found using gabor filter [35] which is a Gaussian envelope modulated

by a sinusoidal plain wave. It ensures that the major contribution in convolution response comes from the local small patch. The local orientation of a pixel is estimated by applying six gabor filters at an angle of $\frac{\pi}{6}$. The maximum responsive gabor filter is considered to code that pixel. Encoding is done into three bit code for each pixel. Hamming distance is used for matching. Both local and global scores are fused to get the better result.

In [79], a bank of six gabor filters at an angle of $\frac{\pi}{6}$ is applied to extract features for those pixels that are having varying gabor responses. All pixels do not contribute to discrimination equally as some of them may be at a similar background patch; hence, they may not possess any dominant orientation. Such pixels are ignored and the orientation code is computed as shown in Fig. 2.13(b). Similarly, magnitude code is obtained by the real and imaginary part of the gabor filers as shown in Fig. 2.13(c). The orientation and magnitude information are fused to achieve better results.

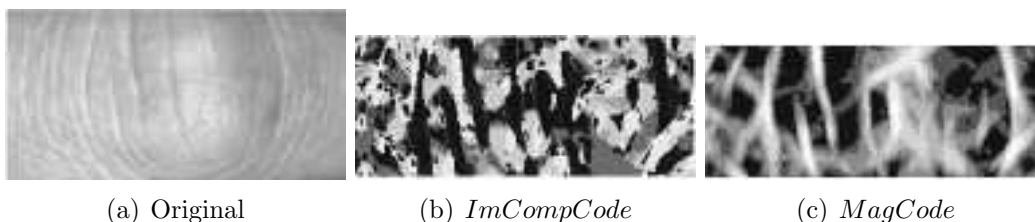


Figure 2.13: Improvement over Gabor based *Compcode*. (a) Original Image, (b) Orientation Code (*ImCompCode*), (c) Magnitude Code (*MagCode*) (Images taken from [79])

In [78], three local features *viz.* phase congruency, local orientation and local phase as shown in Fig. 2.14 are extracted. All of them are computed using the quadrature pair filter and are fused at score level. Finally, all are fused along with the gabor based local features and *BLPOC* based global features [80] to achieve the better performance.



Figure 2.14: Local Feature Extraction

2.3 Palmprint based Biometric System

Palmprint recognition systems are broadly based on structural and statistical features. In [28], line-like structural features are extracted by applying morphological operations over edge-maps. In [23], structural features such as points on principle line and some isolated points are utilized for palmprint authentication.

Gabor based directional filtering is used to develop several palmprint based recognition systems such as [35], [36], [65], [76]. In [76], single fixed orientation gabor filter is applied over the palmprint and the resulting Gabor phase is binarized using zero crossings. In [36], bank of elliptical Gabor filters with different orientations is employed to extract the phase information of the palmprint image and is merged according to a fusion rule to produce feature vector. In [35], the palmprint is processed using the bank of Gabor filters with different orientations. The highest filter response is preserved as features. Further, to improve the performance, a modified algorithm using fuzzy C-means is used to cluster the orientation of each Gabor filter in [73]. In [65], the palmprint is processed using the bank of orthogonal Gabor filters. Their differences are considered as palmprint features. All these systems use hamming distance for matching two palmprints. Statistical techniques such as Principle Component Analysis (*PCA*), Linear Discriminant Analysis (*LDA*), Independent Component Analysis (*ICA*) and their combinations are also applied to palmprints to achieve better performance [43],[62],[70].

Several other techniques such as Stockwell [6], Zernike moments [7], Discrete Cosine Transforms (DCT) [8] and Fourier [9] transforms are also applied to achieve

good performance. The palmprint samples are partitioned into several different ways to compliment the transform or the method that is finally used to extract the features.

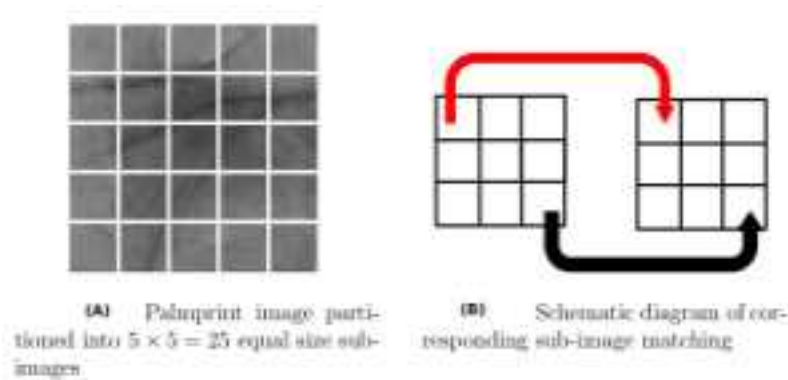


Figure 2.15: Partitioning for Zernike based Palmprint System [7]

In [7], each palmprint is partitioned into non-overlapping blocks as shown in Fig. 2.15. From each block, Zernike moment based features are computed. The order of the moment signifies the degree of the detailed information. Higher the order, more is the information. Lower order moments are used to compute features as they can coarsely represent the image information. Blocks are also weighed based on the entropy of the block and the binarised feature vector is matched using the hamming distance.

In [9], palmprint samples are divided into overlapping square blocks as shown in Fig. 2.16. The $2D$ block is converted into two $1D$ signal by performing averaging operation in horizontal and vertical directions. The phase difference between horizontal and vertical signals is binarised using zero-crossing to obtain the binary vector. The hamming distance is used for matching.

In [6], the palmprint is divided into circular strips. The radius of the strip is a variable and is optimized for performance as shown in Fig. 2.17. Similar to Fourier transform, Stockwell transform can also be used for spectral decomposition. But the

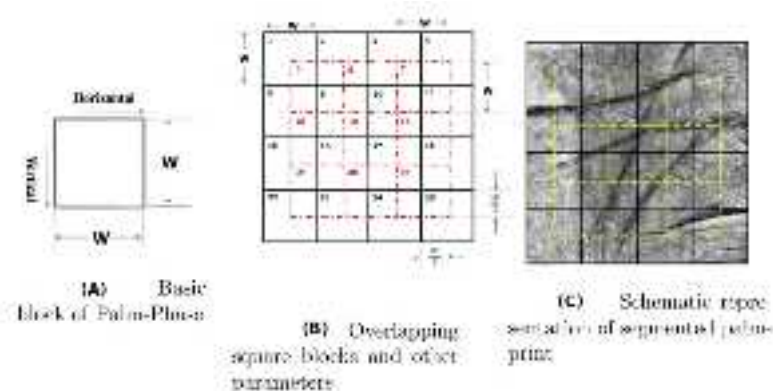


Figure 2.16: Partitioning for Phase based Palmprint System [9]

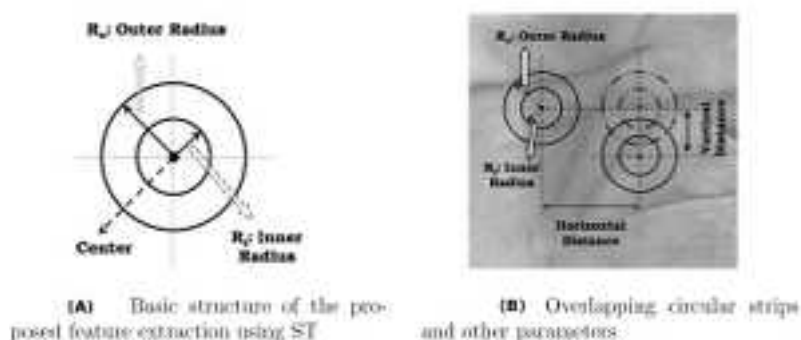


Figure 2.17: Partitioning for Stockwell based Palmprint System [6]

instantaneous – phase used by Stockwell transform produces feature vector that encodes both phase and time which is more useful than only phase or magnitude as we can get from Fourier transform. Hence, features using Stockwell transform are computed from this annular ring as shown in Fig.2.17. The 2D annular ring is converted into 1D average vector over which Stockwell transform is applied. These features are binarised and hamming distance is used for matching.

In [8], the palmprint samples are divided into oriented rectangular boxes of variable size and orientation as shown in Fig. 2.18. The 2D DCT can perform the image compression and hence, is used to save energy of the image more efficiently.

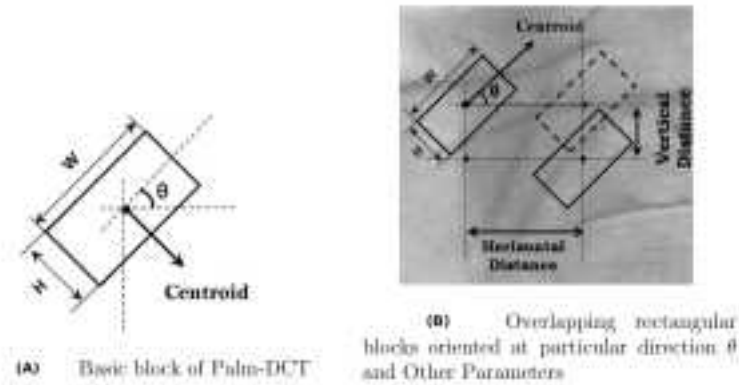


Figure 2.18: Partitioning for *DCT* based Palmprint System [8]

The *DCT* based feature for each rectangular block is computed. For each rectangle, average in the vertical direction is computed to get a $1D$ vector that is windowed using the hanning window to suppress the spectral leakage. On each windowed signal, the *DCT* is applied and the coefficients are used as features. Features of the adjacent block are subtracted and binarised to obtain the binary feature vector. The hamming distance is used to determine its matching score.

2.4 Multi-modal Biometric System

Not much work has been reported in this area largely because of non-availability of multi-modal biometric database. In [64], 2D discrete wavelets have been used to extract low dimensional features from iris and face. A reduced joint feature vector set is obtained using Direct Linear Discriminant Analysis (*DLDA*) which is finally used for classification. In [58], face and iris (left and right both) are fused using *SIFT* feature vector. The classification is done using nearest neighborhood ratio matching. In [81], iris and face are considered and PCA coefficients along with Daughman's gabor filter approaches are used for face and iris images respectively. Scores are fused after min-max normalization.

In [59], scores obtained by *eigenfinger* and *eigenpalm* are fused while in [39] hand shape and palm features are fused. In [38], finger geometry and dorsal finger surface information are fused to improve the performance as compared to its unimodal version. In [49], features which are automatically detected by tracking are encoded using efficient directional coding while Ridgelet transformation is used for feature matching and these scores are fused using SVM. In [48], 1D gabor filters are used to extract features from knuckle and palmprint. In [82], fusion of knuckle and palmprint information is done at score level. Sharp edge based knuckleprint features are denoised using wavelet. Corner features with their local descriptors are considered for palmprint images. Finally, matching is done by cosine similarity function and hierarchical hand metric. In [53], radon and haar transforms are used for feature extraction from knuckleprints of multiple fingers and nonlinear fisher transformation is done for dimensionality reduction. Matching is done using parzen window classification. In [47], score level fusion is performed on palm and knuckleprints using phase only correlation (*POC*) function.

Chapter 3

Preliminaries

There exist several techniques for extracting features from iris, knuckle and palmprint. These techniques can broadly be divided into two categories: *global* and *local*. Any global feature extraction technique considers whole image to obtain features from the image while on the other hand, local techniques consider only a few neighboring pixels or a fixed size in each of local patches. Some of the well known global extraction techniques are designed with the help of Gabor filters, local binary patterns, Radon based transforms, Gaussian based ordinal measures, Wavelets, Stockwell transform, Zernike moment and discrete cosine transform (DCT). Similarly, there are several local feature extraction techniques to extract features. Some of them are *PCA*, *LDA*, *Gabor – PCA*, *LBP – PCA*, *DFT* etc. Advantages of the use of global features is that they can be computed at once for the whole image; hence they should be easy to compute and fast. But full image approximation may create the problem of under-estimation. Local features are extracted for each pixel, block or key point; hence, they are computationally intensive. But performance-wise, they are found to be better because of the effective use of smaller neighborhood and similar patch approximation.

Generally, features of iris, knuckle and palmprint are converted into binary vector

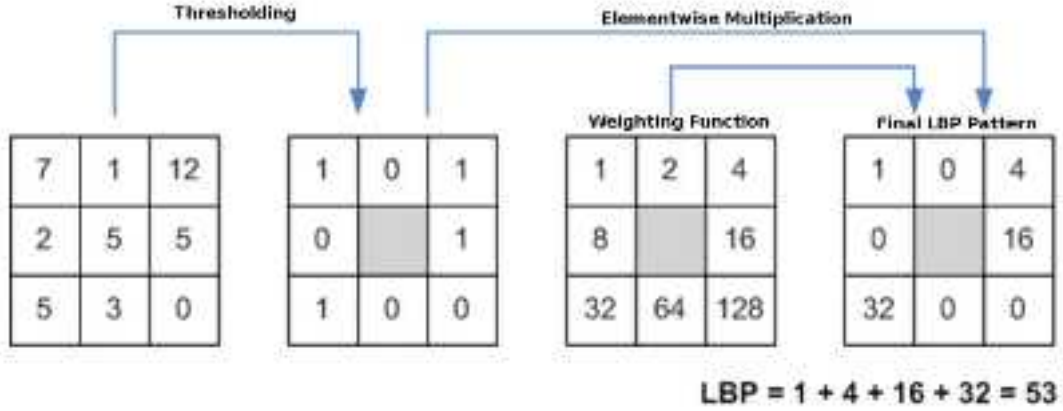
and hamming distance based measures are used to compute matching scores between two feature vectors. One of the disadvantages of such a matching strategy is that if the images are not well registered, the performance of the system gets severely affected. This is because it never attempts to compute the pixel or patch level correspondence.

This chapter discusses some well known feature extraction techniques which are used to design biometric systems based on Iris, Knuckleprint and Palmprint. These techniques are local binary pattern (LBP) [54], Phase Only Correlation (POC) [80], KLT Corner Extraction [63] and LK-tracking algorithms [44].

3.1 Local Binary Pattern (LBP)

It is a well known texture operator [54] which is simple and computationally efficient and effective. It assumes that any image texture has some pattern and a strength is associated to it. It is invariant to illumination and its intensity has the range from 0 to 255; hence, it can be realized as a gray-scale image. It is based on the assumption that pixel's relative gray value with respect to its 8-neighborhood pixels can be more stable than its own intensity value. A 8-bit local binary pattern is computed by thresholding its 8 neighbors with respect to itself and by representing the ordinal relation as shown in Fig. 3.1.

The *LBP* features of each image can be computed in the form of *LBP* histograms. These histograms are saved in the form of 1-D vectors and are used to compute distance. Let S and M be the histograms of the probe image and the gallery image respectively. To discriminate histogram features, there exist several possible dissimilarity measures as discussed below.

Figure 3.1: *LBP* Computation

- Histogram intersection:

$$D(S, M) = \sum_i \min(S_i, M_i) \quad (3.1)$$

- Log-likelihood statistic:

$$L(S, M) = - \sum_i S_i \log M_i \quad (3.2)$$

- Chi square statistic (χ^2)

$$\chi^2(S, M) = \sum_i \frac{(S_i - M_i)^2}{S_i + M_i} \quad (3.3)$$

where S_i and M_i are i^{th} bin of histograms S and M respectively.

The *LBP* based histogram features can be used for face recognition. Let us assume that we have two facial images *probe* and *gallery* between which we have to find out the dissimilarity score. Regions like left eye, right eye, nose and lips of each facial image are divided into $8 \times 8 = 64$ blocks. For each block, a histogram is

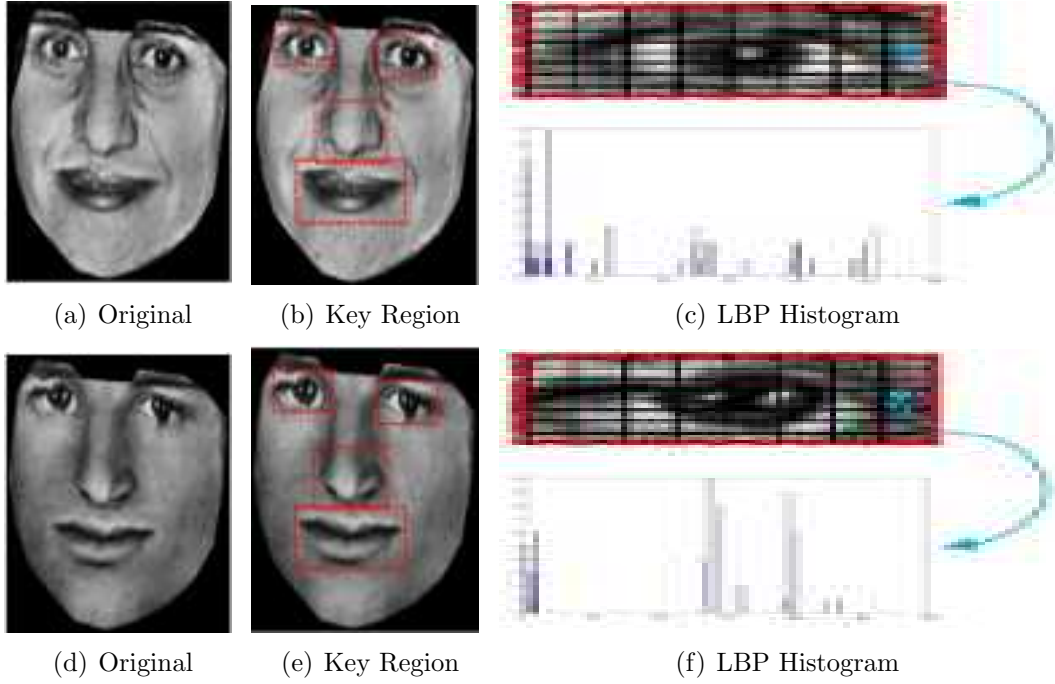


Figure 3.2: Application of *LBP* in Face Recognition

calculated using decimal values of the binary patterns as labels. The concatenation of the histograms for each block in each region acts as the feature vector of that image (say H_{probe} and $H_{gallery}$ for *probe* and *gallery* respectively). This feature vector is used for calculation of dissimilarity between the probe and the gallery images. The Chi square (χ^2) measure can be used to obtain the dissimilarity between probe and gallery image as

$$\chi^2(H_{probe}, H_{gallery}) = \sum_{i=0}^{255} \frac{(H_{probe}^i - H_{gallery}^i)^2}{H_{probe}^i + H_{gallery}^i} \quad (3.4)$$

where H_{probe}^i and $H_{gallery}^i$ are the values for i^{th} label of probe and gallery histograms respectively. Overall dissimilarity score for probe and gallery images can be expressed as

$$D(\text{probe}, \text{gallery}) = \sum_{\forall \text{Region}} \sum_{\forall \text{Blocks}} \chi^2(H_{\text{probe}}, H_{\text{gallery}}) \quad (3.5)$$

It can be noted that since D provides the dissimilarity information between two samples, lower the value of D , better is the match.

3.2 Corner Point Detection

Some key points that are visually significant, lie on the edges or sharp discontinuities. But all points on the edges in an image cannot be considered as key feature points because they all look similar along that edge. Corners have strong derivative in two orthogonal directions and can provide enough robust information for tracking. We have considered corner points as features because of their repeatability and discrimination.

The autocorrelation matrix M [63] can be used to calculate corner points that are having strong orthogonal derivatives. The matrix M can be defined for any pixel at the i^{th} row of the j^{th} column of an image as:

$$M(i, j) = \begin{pmatrix} A & B \\ C & D \end{pmatrix} \quad (3.6)$$

where

$$\begin{aligned}
A &= \sum_{-K \leq a, b \leq K} w(a, b) \cdot I_x^2(i + a, j + b) \\
B &= \sum_{-K \leq a, b \leq K} w(a, b) \cdot I_x(i + a, j + b) \cdot I_y(i + a, j + b) \\
C &= \sum_{-K \leq a, b \leq K} w(a, b) \cdot I_y(i + a, j + b) \cdot I_x(i + a, j + b) \\
D &= \sum_{-K \leq a, b \leq K} w(a, b) \cdot I_y^2(i + a, j + b)
\end{aligned} \tag{3.7}$$

and $w(a, b)$ is the weight given to the neighborhood, $I_x(i + a, j + b)$ and $I_y(i + a, j + b)$ are the partial derivatives sampled within a patch of size $(2K + 1) \times (2K + 1)$ centered at the pixel (i, j) . However, all neighbors may not have same weight.

The matrix M can have two eigen values λ_1 and λ_2 such that $\lambda_1 \geq \lambda_2$ with e_1 and e_2 as the corresponding eigenvectors. All pixels having $\lambda_2 \geq T$ (smaller eigen value greater than a threshold) are considered as corner points. An example is shown in Fig. 3.3.

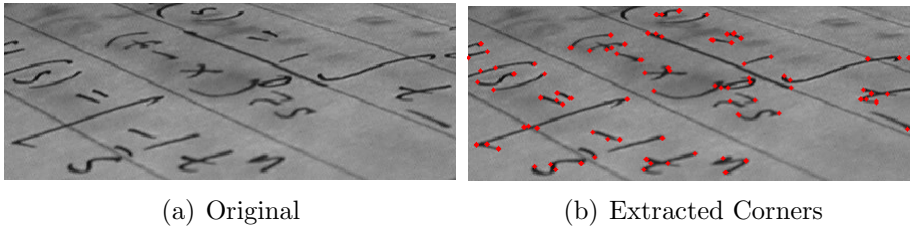


Figure 3.3: Corner Features shown in Red

3.3 Sparse Point Tracking (KLT)

The feature point correspondence problem is the key issue in authentication. We have used corner points as the feature points; corner point correspondence issue can

be tackled with the help of a suitable tracking algorithm. The *KL*-tracking algorithm [44] localizes the set of features points of an image in another image when two images are taken of the same object but at different time. This tracking algorithm makes an effort to estimate the optical flow vector for each sparsely populated feature point and uses that flow vector to estimate the final position of that feature in the subsequent image.

Let there be a feature at location (x, y) at a time instant t with intensity $I(x, y, t)$ and this feature has moved to the location $(x + \delta x, y + \delta y)$ at the time instant $t + \delta t$. Three basic assumptions that are used by KL Tracking to perform tracking successfully are:

- **Brightness Consistency:** Features in a frame do not change much for the small change in the value of δt , *i.e*

$$I(x, y, t) \approx I(x + \delta x, y + \delta y, t + \delta t) \quad (3.8)$$

- **Temporal Persistence:** Features in a frame moves only within a small neighborhood. It is assumed that features have not made much movement for the small change in the value of δt . Using Taylor series and neglecting the high order terms, one can estimate $I(x + \delta x, y + \delta y, t + \delta t)$ as

$$\frac{\delta I}{\delta x} \delta x + \frac{\delta I}{\delta y} \delta y + \frac{\delta I}{\delta t} \delta t = 0 \quad (3.9)$$

Dividing both sides of Eq 3.9 by δt one gets,

$$I_x V_x + I_y V_y = -I_t \quad (3.10)$$

where V_x, V_y are the respective components of the optical flow velocity for

the pixel $I(x, y, t)$ and I_x, I_y and I_t are the derivatives in the corresponding directions.

- **Spatial Coherency:** In Eq. 3.10, there are two unknown variables V_x and V_y for every feature point. Hence finding unique V_x and V_y for every feature point is an ill-posed problem¹. The spatial coherency assumption is used to solve this problem. It assumes that a local mask of pixels moves coherently. Therefore, one can estimate motion of the central pixel by assuming the local constant flow. The KL tracking uses a non-iterative method by considering flow vector (V_x, V_y) as constant within 5×5 neighborhood (*i.e* 25 neighboring pixels, $P_1, P_2 \dots P_{25}$) around the current feature point (center pixel) to estimate its optical flow. The said assumption is fair as all pixels within a mask of 5×5 can have coherent movement. Hence, one can obtain an over-determined system of 25 linear equations which can be represented by

$$\underbrace{\begin{pmatrix} I_x(P_1) & I_y(P_1) \\ \vdots & \vdots \\ I_x(P_{25}) & I_y(P_{25}) \end{pmatrix}}_C \times \underbrace{\begin{pmatrix} V_x \\ V_y \end{pmatrix}}_V = - \underbrace{\begin{pmatrix} I_t(P_1) \\ \vdots \\ I_t(P_{25}) \end{pmatrix}}_D \quad (3.11)$$

where rows of the matrix C represent the derivatives of image I in x and y directions and those of D are the temporal derivative at 25 neighboring pixels. This system of linear equations is used to compute the estimated flow of current feature point \hat{V} using least square method. The 2×1 matrix \hat{V} is defined as

$$\hat{V} = (C^T C)^{-1} C^T (-D) \quad (3.12)$$

¹There are two variables to evaluate using only one equation

The final location $\hat{\mathbf{F}}$ of any feature point is estimated with the help of its initial position vector $\hat{\mathbf{I}}$ and the estimated flow vector $\hat{\mathbf{V}}$ as

$$\hat{\mathbf{F}} = \hat{\mathbf{I}} + \hat{\mathbf{V}} \quad (3.13)$$

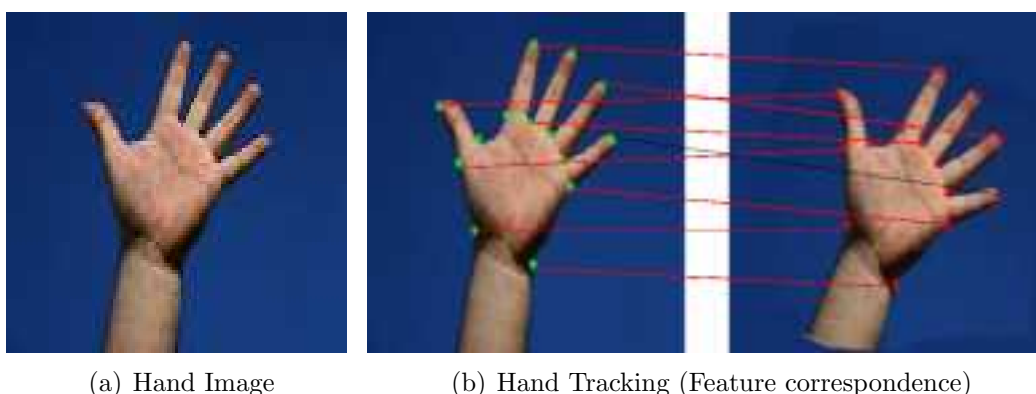


Figure 3.4: Hand Tracking Application

A hand tracking system can make use of the tracking algorithm as shown in Fig. 3.4. It can estimate the sparse optical flow using KL-tracking algorithm. The optical flow which is nothing but the direction of feature motion (*i.e* motion vectors) for each feature is computed for all video frames. Hence, feature correspondence can be used to track hand in a video while it is moving freely.

3.4 Phase Only Correlation (POC)

The *POC* can play an important role in registering two images. Let f and g be two $M \times N$ images. Assume $M = 2M_0 + 1$, $N = 2N_0 + 1$ and the image center is at location $(0, 0)$. If F and G are the Discrete Fourier Transform (*DFT*) of f and g

images respectively, then

$$F(u, v) = \sum_{m=-M_0}^{M_0} \sum_{n=-N_0}^{N_0} f(m, n) e^{-j2\pi(\frac{mu}{M} + \frac{nv}{N})} \quad (3.14)$$

$$= A_F(u, v) e^{j\theta_F(u, v)} \quad (3.15)$$

$$G(u, v) = \sum_{m=-M_0}^{M_0} \sum_{n=-N_0}^{N_0} g(m, n) e^{-j2\pi(\frac{mu}{M} + \frac{nv}{N})} \quad (3.16)$$

$$= A_G(u, v) e^{j\theta_G(u, v)} \quad (3.17)$$

Cross Phase Spectrum between G and F is given by:

$$R_{GF}(u, v) = \frac{G(u, v) \times F^*(u, v)}{|G(u, v) \times F^*(u, v)|} = e^{j(\theta_G(u, v) - \theta_F(u, v))} \quad (3.18)$$



Figure 3.5: Phase Only Correlation (POC) between two translated images. Image in (c) represents the corresponding POC values for each spatial location

Phase Only Correlation (POC) is the $IDFT$ of $R_{GF}(u, v)$ and is given by :

$$P_{gf}(m, n) = \frac{1}{MN} \sum_{u=-M_0}^{M_0} \sum_{v=-N_0}^{N_0} R_{GF}(u, v) e^{j2\pi(\frac{mu}{M} + \frac{nv}{N})} \quad (3.19)$$

From [50], we can have the following. When two images are “Same”, the POC function $P_{gf}(m, n)$ becomes kronecker delta function $\delta(m, n)$. If two images are “Similar”, the POC function gives a distinct sharp peak; otherwise, the peak value

drops significantly. Hence peak height of $P_{gf}(m, n)$ can be considered as a similarity measure.

Image in Figure 3.5(b) is a translated version of image in Figure 3.5(a). One can clearly observe from Fig. 3.5(c) that there exists a sharp distinct peak which points to the location (t_x, t_y) at which translation is most likely to be expected. In other words, image in Fig. 3.5(b) can be registered by translating image in Fig. 3.5(a) by t_x units in x -direction and t_y units in y -direction.

Chapter 4

Iris Recognition System

This chapter deals with the problem of designing an efficient iris based recognition system. Two state-of-the-art techniques (Integro-differential and Hough transformation) are applied in designing the system so that they can compliment to each other for the efficient iris segmentation. The iris contains good amount of texture but it is required to be enhanced. Identification/authentication is performed by tracking corner features. Like any other biometric system, iris based recognition system consists of five major tasks, *viz.* *ROI* extraction, quality estimation, *ROI* preprocessing, feature extraction and matching. The overall architecture of the proposed iris based recognition system is shown in Fig. 4.1.

4.1 Iris ROI Extraction

This section proposes an efficient iris segmentation technique. It approximates pupil and limbic boundaries by circles. It extracts iris ROI by applying hough and integro-differential transformations. A modified hough transform is used to locate the inner boundary and then sector based integro-differential operator is applied to localize the outer iris boundary. The detected iris is projected into a rectangular strip which

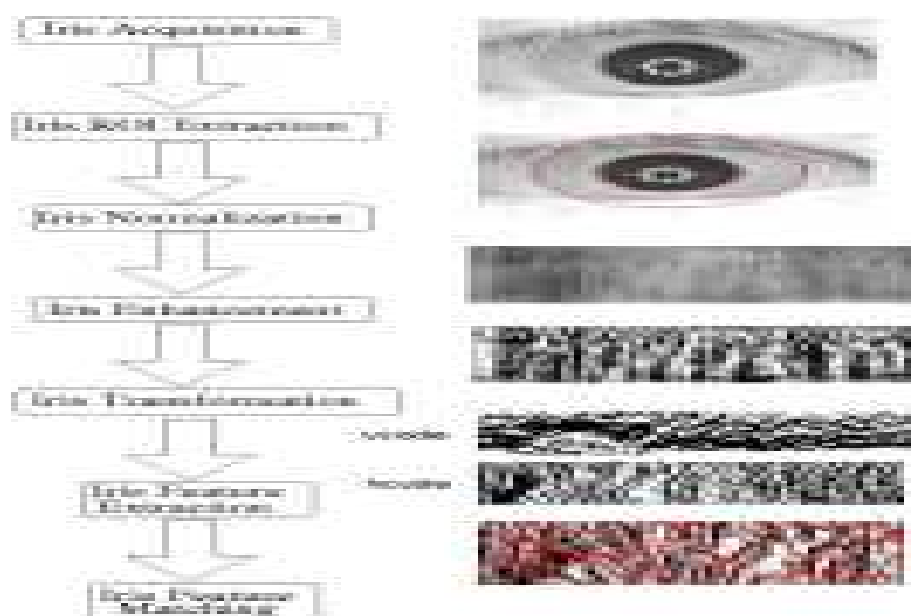


Figure 4.1: Overall Architecture of the Proposed Iris Recognition System

is shown in Fig. 4.2.

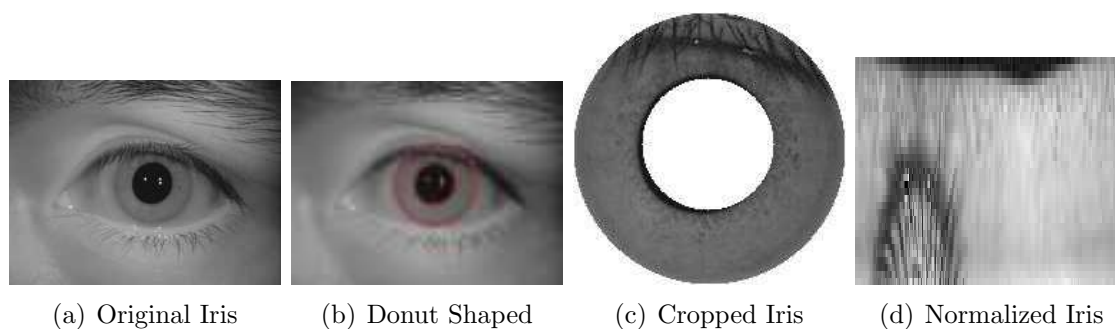


Figure 4.2: Iris Segmentation

4.1.1 Iris Inner Boundary Localization

The pupil of an eye can be modeled as a dark circular region within the iris. Each eye image is scaled down for faster processing and thresholded based on image brightness to filter out pixels of the pupil and to get a binary image I_t . This reduces

the computation for pupil boundary (*i.e.* iris inner boundary) on only dark pixels in the image. However, there may be some eyelashes, eyebrows or shadow points which can act as noise in inner boundary detection. Also, specular reflection on the pupil may cause the incorrect detection of the boundary. Hence, morphological operator of flood-filling with four neighbors is applied to the binary image I_t . Pixels which cannot be reached by flood-filling the background form holes are removed. Thus, specular reflection inside the pupil region and other dark spots caused by eyelashes are removed as shown in Figure. 4.3(b) represented as I_{tf} .

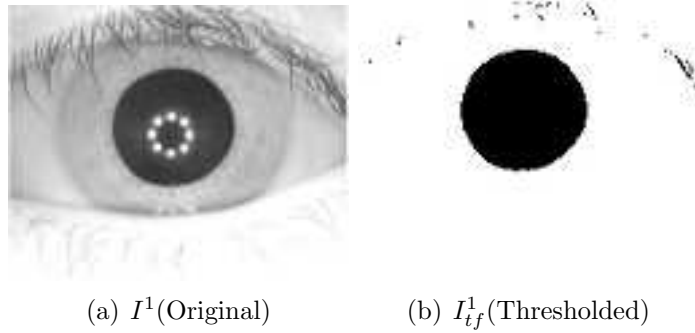


Figure 4.3: Iris Pupil Segmentation (Thresholding)

The Sobel filters in both horizontal and vertical directions are applied on the iris image to obtain the horizontal and vertical gradient images. The Sobel derivative is an approximation to image intensity gradient in a given direction. The gradient magnitude image I_g is obtained by

$$I_g(x, y) = \sqrt{(I_{gh}^2(x, y) + I_{gv}^2(x, y))} \quad (4.1)$$

where I_{gh} and I_{gv} are horizontal and vertical gradient images.

The gradient magnitude image I_g is thresholded to generate binary image I_{gb} as shown in Figure. 4.4(b), representing only strong edges. Edge orientation at any

pixel (x, y) in the generated binary image is obtained by:

$$\theta(x, y) = \tan^{-1} \left(\frac{I_{gv}(x, y)}{I_{gh}(x, y)} \right) \quad (4.2)$$

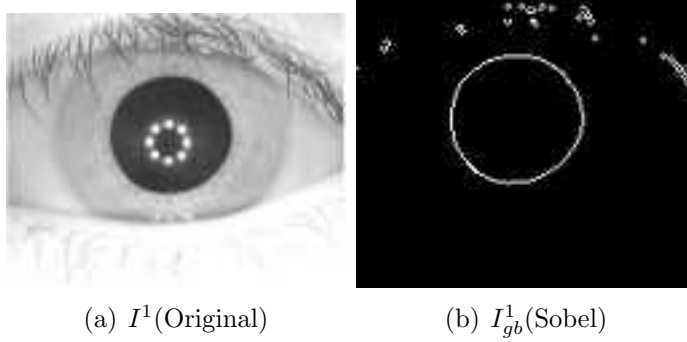


Figure 4.4: Iris Pupil Segmentation (Gradient based Thresholding using Sobel)

An improved circular Hough transform [10] is applied over I_{tf} to detect the pupil boundary. The top left-most corner is considered as the origin. The original Hough transform for circle detection has three parameters; hence the parametric space is of $3D$ viz. x and y coordinates of the center and the radius r . In order to reduce $3D$ parametric search space, the Hough transform is modified so that the search can be performed on $1D$ space (*i.e.* only on the radius r).

Modified Hough Transform : Suppose, an edge pixel (x, y) in the generated binary image is on a circle. For any fixed radius, there can only be two potential pupil centers (c_1^x, c_1^y) and (c_2^x, c_2^y) . They must be on the opposite sides of the tangential line to the circle at that point and over the normal line as shown in Fig. 4.5.

These potential centers are calculated for different radii r using the normal to the orientation angle $\theta(x, y)$ by using the following equations:

$$c_1^x = x + r \cdot \sin(\theta(x, y) - \pi/2) \quad (4.3)$$

$$c_1^y = y - r \cdot \cos(\theta(x, y) - \pi/2) \quad (4.4)$$

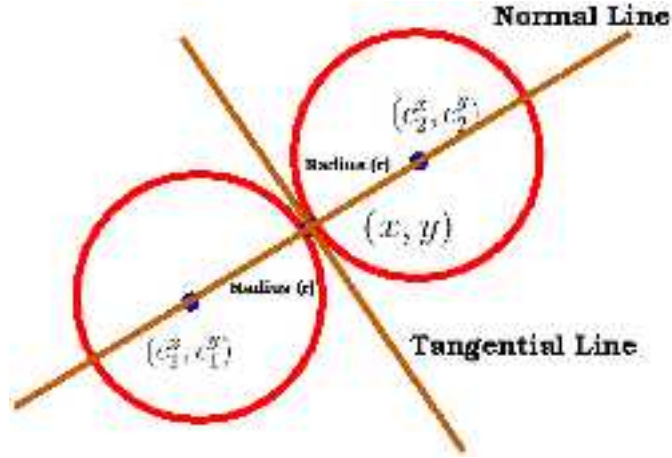
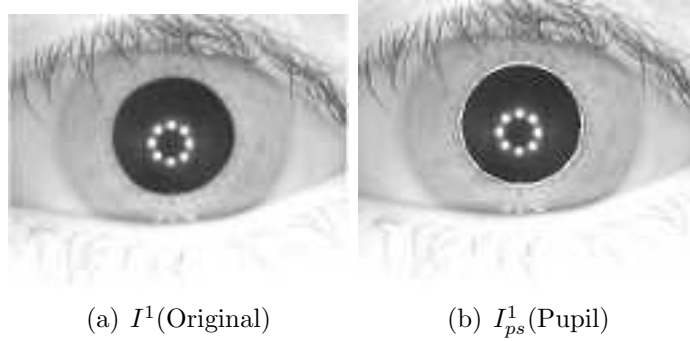


Figure 4.5: For any radius r , any point (x, y) having 2 pupil centers (c_1^x, c_1^y) and (c_2^x, c_2^y)

$$c_2^x = x - r \cdot \sin(\theta(x, y) - \pi/2) \quad (4.5)$$

$$c_2^y = y + r \cdot \cos(\theta(x, y) - \pi/2) \quad (4.6)$$



(a) $I^1(\text{Original})$

(b) $I_{ps}^1(\text{Pupil})$

Figure 4.6: Segmented Iris Pupil

A voting scheme is devised in which all edge pixels cast a vote for its likely-to-be-circle. A 3-D array A is created for storing the votes for every set of possible parameter set where $A(i, j, r)$ represents the number of edge pixels casting vote for the circle having center at (i, j) pixel with radius r . Each edge pixel for a fix radius r can vote for only two circles that have their center at a distance of r from itself in either side as shown in Fig. 4.5. The values $A(c_1^x, c_1^y, r)$ and $A(c_2^x, c_2^y, r)$

are incremented by 1 for each edge point (x, y) , if the candidate points (c_1^x, c_1^y) and (c_2^x, c_2^y) are lying within the image boundary of the generated binary image. The parameter set with maximum votes give the coordinates of the center and the radius of the iris inner boundary as shown in Figure 4.6(b). The algorithm for inner boundary localization is described in Algorithm 4.1. Results obtained at each step of the algorithm are shown in Figure 4.7.

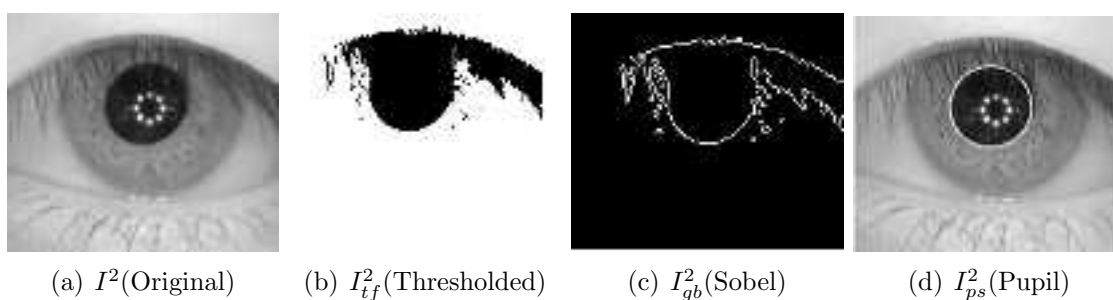


Figure 4.7: All Steps in Iris Pupil Segmentation

4.1.2 Iris Outer Boundary Localization

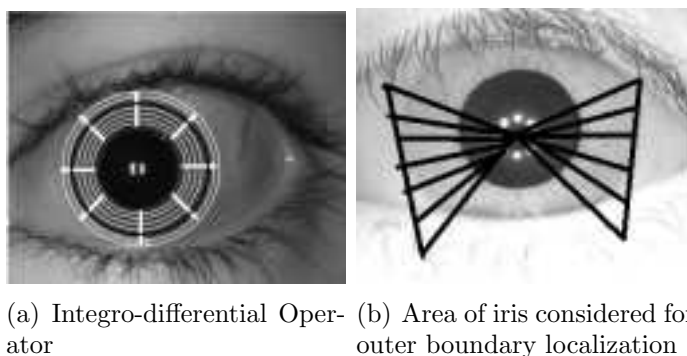


Figure 4.8: Application of Integro-differential Operator

The contrast across the outer iris boundary is less compared to the inner boundary. Thus, any edge detector may fail to detect the true edges. To tackle this issue, circular integro-differential operator [19] which uses raw derivative information is used.

Algorithm 4.1 Pupil Segmentation**Require:**

Iris image I of dimension $m \times n$,
 $p_{r_{min}}$: minimum pupil radius,
 $p_{r_{max}}$: maximum pupil radius,
 t : binary threshold.

Ensure:

Pupil center c_p with co-ordinates as (c_p^x, c_p^y) ,
Pupil radius p_r .

```

1:  $I_t \leftarrow \text{threshold}(I, t)$ ; // generate binary image after thresholding
2:  $I_{tf} \leftarrow \text{remove\_specular\_reflection}(I_t)$ ; // flood filling
3:  $I_g, I_{gh}, I_{gv} \leftarrow \text{Sobel}(I_{tf})$ ; // Sobel edge detection
4:  $I_{gb} \leftarrow \text{Threshold\_Gradient}(I_g)$ ; // choosing the best edge points
5:  $E \leftarrow$  white pixels in  $I_{gb}$ ; // collect the edge points in  $I_{gb}$ 
6: for all Edge pixels  $(x, y) \in E$  do
7:    $\theta(x, y) \leftarrow \tan^{-1} \left( \frac{I_{gv}(x,y)}{I_{gh}(x,y)} \right)$ ; // edge orientation at a point
8: end for

9:  $A(m, n, p_{r_{max}}) \leftarrow 0$ ; // 3-D array initialization for voting

10: for all Edge pixels  $(x, y) \in E$  do
11:   for  $r = p_{r_{min}}$  to  $p_{r_{max}}$  do
12:     Compute  $(c_1^x, c_1^y), (c_2^x, c_2^y)$  by putting  $(x, y)$  and  $\theta(x, y)$  in eqs. (4.3)-(4.6);
13:     if Point  $(c_1^x, c_1^y)$  lies within  $I_{gb}$  image then
14:        $A(c_1^x, c_1^y, r) \leftarrow A(c_1^x, c_1^y, r) + 1$ ; // Vote Casting
15:     end if
16:     if Point  $(c_2^x, c_2^y)$  lies within  $I_{gb}$  image then
17:        $A(c_2^x, c_2^y, r) \leftarrow A(c_2^x, c_2^y, r) + 1$ ; // Vote Casting
18:     end if
19:   end for
20: end for

21:  $c_p^x \leftarrow \text{argmax}_{(i)} A(i, j, k)$ ;
22:  $c_p^y \leftarrow \text{argmax}_{(j)} A(i, j, k)$ ;
23:  $p_r \leftarrow \text{argmax}_{(k)} A(i, j, k)$ ;

```

Integro-differential operator: For any circle with center (c^x, c^y) and radius r , the integro-differential operator adds the intensity values over this circle and calculates the difference in the summation over the concentric circle of higher radius

$(r + \delta r)$. The circle having the maximum jump in terms of this summation gives the outer iris boundary as shown in Fig. 4.8(a). The integro-differential operator can be expressed as:

$$G_\sigma(r) * \left(\frac{\sum_\theta [I(c^x - (r + \delta r) \sin \theta, c^y + (r + \delta r) \cos \theta) - I(c^x - r \sin \theta, c^y + r \cos \theta)]}{2\pi r} \right) \quad (4.7)$$

where $G_\sigma(r)$ is radial Gaussian operator with a standard deviation of σ and $*$ is the convolution operator. The arguments (c^x, c^y) and r for the maximum response value of this operator over the image give the coordinates of iris center and radius respectively.

4.1.3 Proposed Segmentation Algorithm

The image is smoothed using 2-D Gaussian filter to remove any stray noise. Iris center and pupil center may not be concentric, but are usually closed to each other. Hence iris center is searched within a $W \times W$ window around the pupil center (c_p^x, c_p^y) . For each point within this window, intensity values over an arc of $(-\pi/4, \pi/6) \cup (5\pi/6, 5\pi/4)$ radian angular sectors (with respect to horizontal as shown in Figure. 4.8(b)) over the perimeter are summed up for any particular radius. We have chosen only these sectors because in these sectors of the iris, occlusion is empirically found to be minimum as compared to other iris areas. The gradient for this sum is calculated for all radius. Parameters of the circle with maximum gradient is considered as the coordinates of iris center and iris radius.

The algorithm for outer iris boundary localization is explained in Algorithm 4.2. It uses,

- (a) The co-ordinates of pupil center (c_p^x, c_p^y) , the original image of dimension $m \times n$,

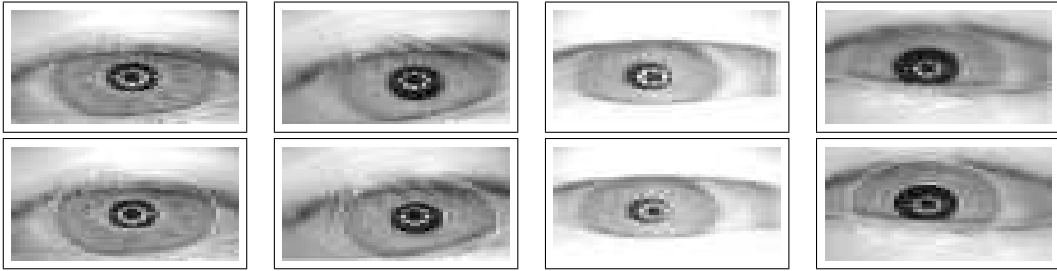


Figure 4.9: Iris Localization (1st Row : Original Iris, 2nd Row : Segmented Iris)

(b) The iris radius range is $(i_{r_{min}}, i_{r_{max}})$,

(c) The search window of size $W \times W$ around the pupil center within which iris center is assumed to be located,

(d) There is a occlusion free range of sector angles α_{range} .

The original image is smoothened to remove noise and circular integro-differential operator is applied over the occlusion free sectors using the candidate iris center points around the pupil center and the radii in the range. The circular summation of intensity for all candidate centers and for all radii is computed. The center coordinates and radius for which the maximum difference is obtained are considered as the iris center and radius. Algorithm 4.2 finds the parameters for outer iris boundary. Some typical eye images after iris localization are shown in Figure 4.9.

4.1.4 Iris Normalization

The iris samples suffer from dimensional inconsistencies among eye images mainly due to the following reasons:

- Iris stretching caused by pupil dilation due to varying illumination
- Varying imaging distance
- Rotation of the camera

Algorithm 4.2 Iris Segmentation

Require:

Iris image I of dimension $m \times n$,
 $i_{r_{min}}$: minimum iris radius,
 $i_{r_{max}}$: maximum iris radius,
 (c_p^x, c_p^y) : Pupil center,
 p_r : pupil radius,
 W : search window,
 α_{range} : angular range defining the occlusion free sectors.

Ensure:

Iris center $c_i(c_i^x, c_i^y)$,
 iris radius i_r .

```

1:  $I_s \leftarrow GaussSmooth(I, \sigma = 0.5, k = 3)$ ; //  $k$ : kernel size, Gaussian noise removal
2:  $max_{diff} \leftarrow 0$ ; // the maximum change in contour summation
3: for all points  $(c^x, c^y) \in [W \times W]$  window around  $(c_p^x, c_p^y)$  do
4:    $prev_{sum} \leftarrow 0$ ; // previous circular summation of intensity values
5:    $start_{flag} \leftarrow True$ ; // no circle has yet been summed up
6:   for  $r = i_{r_{min}}$  to  $i_{r_{max}}$  do
7:      $c_{sum} \leftarrow 0$ ;
8:     for all  $\alpha \in \alpha_{range}$  do
9:        $c_{sum} \leftarrow c_{sum} + I(c^x - r \sin(\alpha), c^y + r \cos(\alpha))$ ; //sector-wise summation
10:    end for
11:     $diff_{sum} \leftarrow c_{sum} - prev_{sum}$ ; // calculation of difference of sum
12:     $prev_{sum} \leftarrow c_{sum}$ ;
13:    if  $diff_{sum} > max_{diff}$  and  $start_{flag} \neq True$  then
14:       $max_{diff} \leftarrow diff_{sum}$ ;
15:       $c_i^x \leftarrow c^x, c_i^y \leftarrow c^y, i_r \leftarrow r$ ; // update the parameters
16:    end if
17:     $start_{flag} \leftarrow False$ ; // a circle has been summed up
18:  end for
19: end for

```

- Head tilt
- Rotation of the eye within the eye socket.

The iris normalization process produces iris regions which have the constant dimension. Hence, two images of the same iris under different environmental conditions

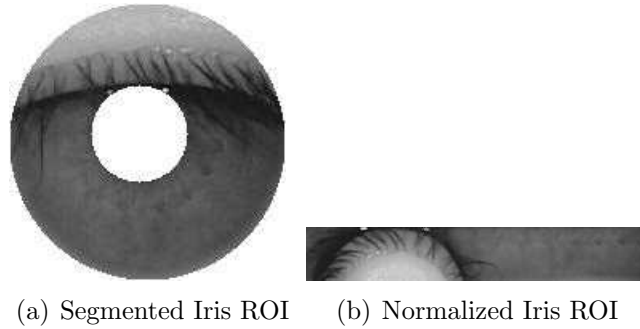


Figure 4.10: Normalization of the Cropped Iris

have their unique and random characteristic features at more or less same spatial location. Therefore, the iris can be transformed to a fixed dimension rectangular strip as shown in Fig. 4.10(b). For the normalization of the segmented iris, rubber sheet model [20], which assumes iris area to be stretched like rubber, is used. It handles the above mentioned inconsistencies by mapping the iris ring points from Cartesian to polar coordinates, using the following equations:

$$I(x(r, \theta), y(r, \theta)) \rightarrow I(r, \theta) \quad (4.8)$$

$$x(r, \theta) = (1 - r) \cdot x_i(\theta) + r \cdot x_o(\theta) \quad (4.9)$$

$$y(r, \theta) = (1 - r) \cdot y_i(\theta) + r \cdot y_o(\theta) \quad (4.10)$$

where I denotes the segmented iris image, $(x_i(\theta), y_i(\theta))$ and $(x_o(\theta), y_o(\theta))$ are coordinates of the inner and the outer boundary at an angle θ (*w.r.t* the horizontal direction) of pupil and iris centers respectively. The radius r ranges within the interval $[0, 1]$. The circular segmented iris region is divided into m equi-spaced concentric circles and n sectors to obtain $m \times n$ sized rectangular iris strip as shown in Fig. 4.10(b). Each intersection point is mapped to polar coordinate using equations (4.8) - (4.10).

4.2 Iris Quality Estimation

Quality of an image plays an important role in any identification system. Higher the quality, lesser the false accept and false reject rates. The quality of any iris image is affected by the presence of eyelashes and eyelids over the iris region, lack of focus over iris region, improper lightning condition, dilation of the iris *etc.* In this section, an algorithm has been proposed to classify iris images into different quality based classes lying between 1 and 5. Higher class index indicates better quality. The quality of the iris image has been modeled as a function of the following six attributes: Focus (F), Motion Blur (MB), Occlusion (O), Contrast and Illumination (CI), Dilation (D), Specular Reflection (SR). Hence overall quality of the iris image can be represented by

$$Quality = f(F, MB, O, CI, D, SR) \quad (4.11)$$

where f is a function which is learned from the training data using a Support Vector Machine (SVM). Quality attributes from the training set of iris images along with their respective true quality labels are used to train the SVM classifier. This creates a model based classifier which can be used to predict the quality of an iris image. The six quality attributes computed are

1. Focus (F) : It refers to the amount of blur due to defocus in the image.
2. Motion Blur (MB) : It is the blurring effect caused due to the movement of the camera relative to the subject or vice-versa during image acquisition.
3. Occlusion (O) : It is one of the major hurdles in iris recognition. It occurs due to eyelids, eyelashes, specular reflection and shadows.
4. Contrast and Illumination (CI) : It is defined as the range of its intensity level. Any high contrast image generally has a uniformly distributed histogram.

5. Dilation (D) : It is a natural process of expansion of the pupil area due to the lack of proper lightning within the surroundings that reduces the amount of iris area.
6. Specular Reflection (SR) : They are caused due to light source that is used to illuminate the iris. Iris is very reflective, so the light reflection is visible in the acquired image.

4.2.1 Focus (F) based Quality Attribute

Focus of an image refers to the amount of blur due to defocus in the image. It is the blurring introduced in the image when the focal point is outside the depth of the field of object being captured. Greater the distance, higher the amount of defocus blur. The 2D Fourier spectrum of any well focused image is uniform; but for a defocus image, the spectrum is concentrated more towards the low frequencies. The focus of an image can be estimated by calculating the high frequency components in the image spectrum. This is done by convolving the image with the proposed 6×6 kernel.

$$K = \begin{pmatrix} -1 & -1 & -1 & -1 & -1 & -1 \\ -1 & -1 & -1 & -1 & -1 & -1 \\ -1 & -1 & 8 & 8 & -1 & -1 \\ -1 & -1 & 8 & 8 & -1 & -1 \\ -1 & -1 & -1 & -1 & -1 & -1 \\ -1 & -1 & -1 & -1 & -1 & -1 \end{pmatrix} \quad (4.12)$$

This kernel can approximate the 2D Fourier spectrum high frequency band pass filter. Higher the response from the image, more focused the image is. For the proposed 6×6 kernel, its corresponding filter responses are shown in Figure 4.11. One can observe that well focus images have higher responses as compared to the

defocus images.

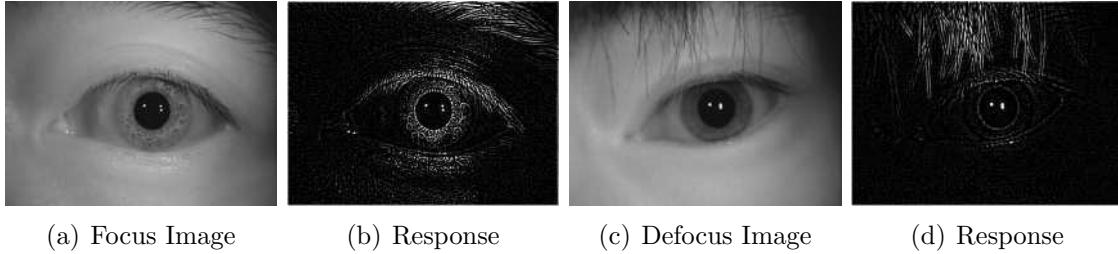


Figure 4.11: Focus Filter Response

4.2.2 Motion Blur (MB) based Quality Attribute

The iris acquisition often gets affected by motion blur because iris movement is very hard to control. The iris image becomes blurred whenever there is a relative movement between the acquisition sensor and subject's eye. The amount of blur is directly proportional to the amount of motion.

The edge width at any edge pixel is used to compute the motion blur. The edge pixels in an image are computed using sobel operators. The edge width at any edge pixel is estimated as the number of pixels between the local extremities at either side of the edge pixel as shown in Fig. 4.2.2. It is assumed that blurred edges are having more width than the sharper edges.

In [26], the amount of motion blur is computed by defining Just Noticeable Blur (JNB) which is the minimum amount of blur required to be perceived by humans. The edge width from which JNB becomes noticeable is called JNB_{width} . It is determined by intensity value range within a small neighborhood as given by

$$JNB_{width} = \begin{cases} 5 & \text{if } Intensity > 50 \\ 3 & \text{if } Intensity \leq 50 \end{cases} \quad (4.13)$$

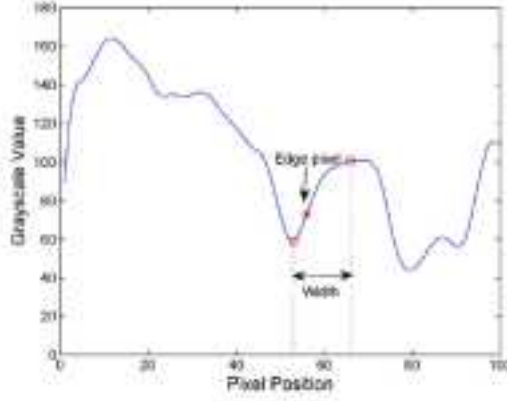


Figure 4.12: JNB Edge Width

The motion blur is computed for an image by dividing it into blocks of size 64×64 . The blocks having edge pixels more than a pre-defined threshold are called edge blocks and only these blocks are considered for computation. For every edge pixel in an edge block, the probability of blur is defined by a psychometric function

$$P(e_{ij}) = 1 - e^{-\left(\frac{\text{edgewidth}(e_{ij})}{JNB_{\text{width}}(B)}\right)^\beta} \quad (4.14)$$

where B is an edge block, $P(e_{ij})$ is the probability of blur, $\text{edgewidth}(e_{ij})$ is the edge width at e_{ij} and $JNB_{\text{width}}(B)$ is the just noticeable blur width for the block B . The parameter β is a value empirically selected as 3.6. As the edge width increases, the probability of blur increases. The motion blur becomes noticeable when $\text{edgewidth}(e_{ij})$ is greater than or equal to $JNB_{\text{width}}(B)$ for that block. From Eq. (4.14), it is seen that the probability of blur increases up to 63.42% when $\text{edgewidth}(e_{ij})$ becomes equal to $JNB_{\text{width}}(B)$.

Hence any edge pixel with the blur probability less than 64% is considered as a pixel of a sharp edge; otherwise, the pixel is considered as a blurred pixel. The motion blur parameter (MB) for any image is defined as the ratio of the total number of pixels belonging to blurred edges to the total number of edge pixels.

4.2.3 Contrast and Illumination (CI) based Quality Attribute

Contrast of an image is defined by the range of its intensity level. Any high contrast image generally obeys uniform distribution. Any such image becomes either too dark or too light. It predicts whether the image is uniformly illuminated or not. The contrast can be estimated by removing the extreme gray values which are basically noise. The range of pixel intensities is divided into three groups which are $(0, 35)$, $(36, 220)$, $(221, 255)$. The intensities in the region $(36, 220)$ indicate moderate intensity levels. The ratio of the pixels in this region to the total number of pixels is used to quantify the amount of uniformity in illumination in the image.

4.2.4 Dilation (D) based Quality Attribute

Dilation of the pupil is a natural process of expansion of the pupil area due to the lack of proper lightning within the surroundings that reduces the amount of iris area. The dilation metric is defined as the ratio of the available iris region to the total area of the iris outer boundary circle. The dilation of the image affects severely the normalization of the iris image. Higher the dilation in the iris image, more is the pixel value redundancy in the normalized image. This also causes the iris texture pattern to shift its spatial position within the normalized iris image. Thus, the dilation attribute can be estimated by

$$dilation = \frac{\text{Area of iris}}{\text{Area of iris outer circle}} = 1 - \frac{r_p^2}{r_i^2} \quad (4.15)$$

where r_i and r_p are the radius of the iris outer and pupil's outer boundary respectively.

4.2.5 Specular Reflection (SR) based Quality Attribute

Specular reflections are caused due to the light sources used to acquire a well illuminated iris image. But iris is very reflective; so the light reflection is visible in the acquired image. Reflection causes white spots in the image which affect the matching score due to missing/wrong data at that spot. The specular reflection can be identified by using an adaptive thresholding. The acquired image is successively thresholded to identify the most obvious reflection points in the image using a high pixel intensity threshold. Some area around the reflection may not be captured. The threshold is lowered by some value to obtain new threshold and the number of pixels is counted again. If the number of pixels is slightly increased, then the area of specular reflection patch is also improved a little. The threshold is further reduced and the process is repeated until the amount of specular reflection is saturated to ensure detection of all pixels affected by reflection.

4.2.6 Occlusion (O) based Quality Attribute

One of the major hurdles in iris recognition is occlusion (hiding of iris) which occurs due to eyelids, eyelashes, specular reflection and shadows as shown in Figure 4.13. Occlusion hides the useful iris texture and introduces irrelevant parts like eyelids and eyelashes which are not even an integral part of any iris image. Occlusion cannot be ignored because it may pose a difficulty to match intra-class irides and also may introduce false matches with other irides. Hence, it is important to locate and to segregate occlusion from a normalized image. Occlusion is detected from the normalized image, instead of original iris image, to reduce the working area which detects occlusion efficiently. It is done in three steps: eyelid detection followed by eyelash and reflection detection.

[A] **Eyelid Detection :**



Figure 4.13: Occlusion in Normalized Iris

Major portion of the occluded area in an iris image is constituted by lower and upper eyelids. Statistically, upper eyelid can be found at the center of left half while lower eyelid at the center of the right half of the normalized image. One cannot discard some area of eyelids heuristically from the normalized image because their sizes are different due to the degree of occlusion; also their locations are not perfectly determined. Eyelids have almost uniform texture and a boundary flooded with eyelashes and shadows. Traditional techniques of parabola/ellipse fitting over eyelids may fail due to the noisy edge information and non-standard shape of eyelids. Eyelids may be extended up to the pupil as well. It means that its upper boundary may not be visible in a normalized image. These challenges have motivated us to use region-growing approach to determine the eyelids. It uses only the texture information to separate eyelid region from the rest.

Region growing is a morphological flooding operation which helps to find objects of uniform texture. Since eyelids have uniform texture, this operation helps to find the eyelid region. In [4], a set S of seed points is selected from the image lying in the region S_d , that is required to be detected. All pixels in 8-neighborhood of any pixel in the set S are checked for their intensity difference with the mean intensity of the set S . Pixels which are having this difference less than a certain threshold are added to S . This process is iterated until no pixel can be added further. Finally, S covers the desired region S_d . Figure 4.14 shows the results of the region-growing algorithm on an image after a few iterations.

Eyelid detection from the normalized iris strip of size $r \times c$ requires two seed points for region-growing, one for each lower and upper eyelid. They are selected as $(r, \frac{c}{4})$

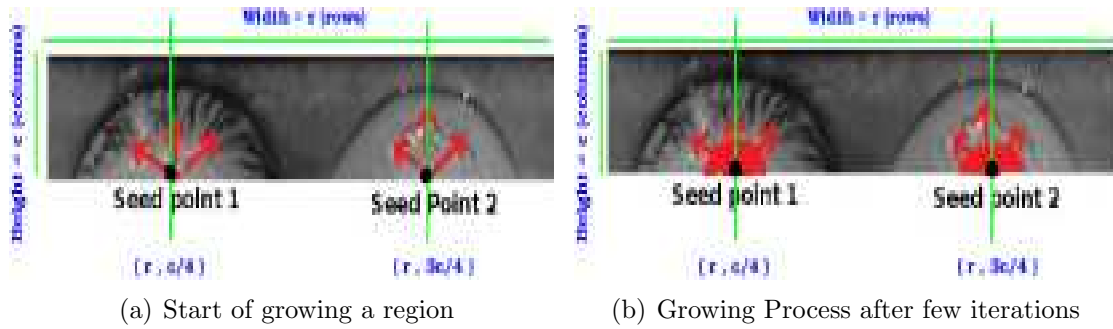


Figure 4.14: Application of Region-Growing

and $(r, \frac{3c}{4})$ for upper and lower eyelid respectively as shown in Fig. 4.14. These two seed points are chosen because after normalization, upper and lower eyelids are centered mostly at $(\frac{\pi}{2})^\circ$ and $(\frac{3\pi}{2})^\circ$ angles *w.r.t.* x -axis. Region-growing begins with these seeds using a low threshold and expands the region until a dissimilar region is encountered. This gives the expected lower and the expected upper eyelid regions. Detection eyelids are shown in Figure 4.15. To obtain both lower and upper eyelid regions, Algorithm 4.3 can be used with different seed points. Region-growing overcomes the shape irregularity of eyelids and gives the exact area which is occluded by eyelids. It fails when eyelid boundary does not have good contrast and hence, it grows outside the eyelid region. To prevent this, region-growing is repeated with a lower threshold so that it does not grow outside the statistical bounds for eyelid regions. If region grows beyond a limit, it indicates that there is no eyelid. Finally, a binary mask is generated in which all eyelid pixels are set to 1. An example is shown in Figure 4.15.



Figure 4.15: Eyelid Regions: Arrows Denote the Direction for Region-Growing

Algorithm 4.3 Eyelid Detection

Require: Normalized Iris image NI of dimension $m \times n$, $s : (s_x, s_y)$: initial seed point in NI , t : region-growing threshold

Ensure: Eyelid region LID , Eyelid Mask $Mask_{eyelid}$

```

1:  $S \leftarrow s$  // Seed point is added to eyelid set  $S$ 
2:  $M = NI(s_x, s_y)$  // Mean of set  $S$ 
3: while True do
4:    $min \leftarrow Infinity, minPoint \leftarrow \phi$ 
5:   for all unallocated neighboring pixels  $(x, y)$  of  $S$  do
6:     if  $|NI(x, y) - M| < min$  then
7:        $min \leftarrow |NI(x, y) - M|$  // absolute difference with region's mean
8:        $minPoint \leftarrow (x, y)$  // keep track of the best point
9:     end if
10:  end for
11:  if  $min > t$  or  $size(S) == size(NI)$  then
12:    break // stop region-growing
13:  end if
14:   $S \leftarrow S \cup minPoint$  // add the best point to the set
15:   $M \leftarrow mean(S)$  // update the mean value
16: end while
17:  $LID \leftarrow S$ 
18:  $Mask_{eyelid} \leftarrow NI(LID)$  // eyelid mask

```

[B] Eyelash Detection :

There are two types of eyelashes: separable and multiple. Separable eyelashes are like thin threads whereas multiple eyelashes constitute a shadow like region. Eyelashes have lower intensity compared to iris texture. But any predefined threshold which can be used to separate them from the rest of iris is difficult to be determined because it changes with illumination condition. Also, since the proportion of eyelashes in the image is not constant, histogram-based thresholding cannot be used. In this section, a new eyelash detection approach to detect both types of eyelashes has been proposed.

Eyelashes have high contrast with their surrounding pixels, but having low in-

tensity. As a result, standard deviation of gray values within a small region around separable eyelashes is high. The standard deviation for every pixel in a normalized image is computed using its 8-neighborhood. It is high in areas where there are separable eyelashes. Multiple eyelashes may have high standard deviation, but they also have dark intensity value. Hence, the low gray value intensity is also given some weight. The computed standard deviation for each pixel is normalized using *max – min* normalization method and is saved in a 2D-array *SD*. If *SD* is used alone for segregating eyelash regions, then multiple eyelashes may not be detected and iris texture which has large standard deviation at some points gets wrongly classified as eyelashes. Hence for each pixel, a fused value $F(i, j)$ is computed which considers both the computed standard deviation as well as the gray value intensity of that pixel defined as

$$F(i, j) = 0.5 \times SD(i, j) + 0.5 \times (1 - N(i, j)) \quad (4.16)$$

where $N(i, j)$ is the normalized gray intensity values (0 – 1) and $SD(i, j)$ is the standard deviation computed using 8 neighborhood pixel intensities for the pixel (i, j) . This fused value $F(i, j)$ boosts up the gap between eyelash and non-eyelash part. The image histogram F_H of F has two distinct clusters: a cluster of low values of F consisting of the iris pixels and the second cluster with high values of F representing eyelash pixels. To identify the two clusters, Otsu thresholding is applied on the histogram F_H of F to obtain binary eyelash mask. It determines two clusters in a histogram by considering all possible pairs of clusters and chooses that clustering threshold that minimizes the intra-cluster variance. It thus separates the eyelash portion from the iris portion. The detected eyelash of an iris image is shown in Figure 4.16. The algorithm for eyelash detection is presented in Algorithm 4.4.

[C] Reflection Detection :

Pixels which exceed a threshold value in gray-scale image are declared as reflec-

Algorithm 4.4 Eyelash Detection

Require: Normalized Iris image NI of dimension $r \times c$

Ensure: Eyelash Mask $Mask_{eyelash}$

- 1: $SD \leftarrow filter2D(NI, std(3, 3))$ // 2D filtering with 3x3 standard deviation filter
- 2: $SD \leftarrow \frac{SD}{max(SD)}$ // normalize w.r.t. maximum value
- 3: $N = \frac{NI}{255}$ // Normalized intensity values(0-1) of NI
- 4: $F = 0.5 \times SD + 0.5 \times (1 - N)$ // fusion of std. deviation and intensity values.
- 5: $F_H \leftarrow imhist(F)$ // image histogram
- 6: $Thresh \leftarrow Otsu(F_H)$ // determine Otsu threshold
- 7: $Mask_{eyelash} \leftarrow threshold(F_H, Thresh)$ // Otsu thresholding: $Mask_{eyelash}(x, y)$ is set only if (x, y) is an eyelash pixel



Figure 4.16: Determination of Eyelash Region

tions because reflections are very bright in every acquisition setting. Also, since occlusion due to reflection is not a major component, it is chosen not to do complex computation to remove reflection. Detected reflection from a sample image is shown in Figure 4.17. A binary mask $Mask_{reflection}$ (reflection mask) is generated in which pixels affected by reflection are set to 1.

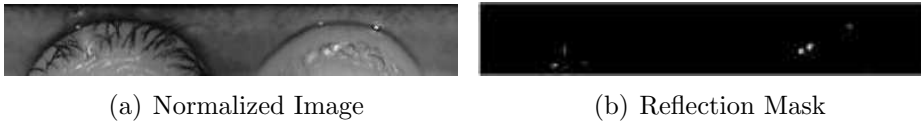


Figure 4.17: Reflection Detection by Thresholding

Final occlusion mask is generated by addition (logical OR) of the binary masks of eyelid, eyelash and reflection. The algorithm to determine occlusion mask $Mask_{occlusion}$ from a normalized image is described in Algorithm 4.5. Detected occlusion of a sam-

ple image is shown in Figure 4.18.

Algorithm 4.5 Occlusion Mask Determination

Require: Normalized Iris image NI of dimension $m \times n$, Eyelid mask $Mask_{eyelid}$, Eyelash Mask $Mask_{eyelash}$, Specular Reflection Mask $Mask_{reflection}$

Ensure: Occlusion Mask ($Mask_{occlusion}$)

- 1: $Mask_{occlusion} \leftarrow Mask_{eyelid} | Mask_{eyelash} | Mask_{reflection}$ // logical OR-ing
 - 2: return ($Mask_{occlusion}$)
-

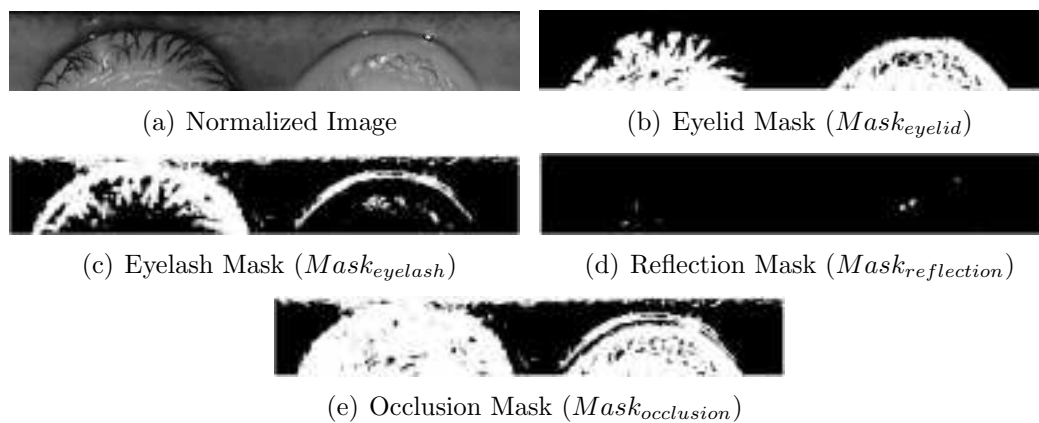


Figure 4.18: Overall Occlusion Mask

4.2.7 Quality Class Determination

The Support Vector Machine (SVM) is trained using a set of 1000 iris images from CASIA Lamp database. The actual quality classes (*i.e* ground truth) in the training set of images are assigned manually. This set of quality attributes along with the quality class label of the iris image is used to train the SVM to learn the function f as defined in Eq. (4.11). The trained classifier based model is used for future prediction of the quality. When a new iris image is given to the system, all quality parameters are normalized to the range (0,1) and are passed to the trained SVM classifier which provides the quality class corresponding to the iris image.

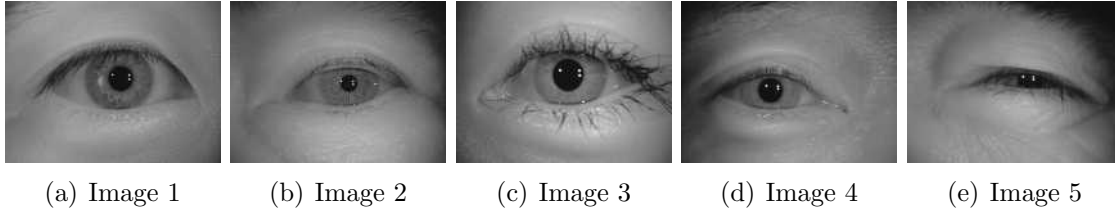


Figure 4.19: Quality Estimation

In Fig. 4.19, some images from the database are shown. Quality parameters of these images and the final quality score are given in Table 4.1. It shows that as the quality of image degrades, its overall quality score also reduces. A poor score is assigned to the image with higher occlusion.

Image	Focus	Blur	Occlusion	Contrast	Dilation	Reflection	Quality
Image 1	0.2034	0.6783	0.8834	0.8873	0.8348	0.9865	5
Image 2	0.1985	0.6138	0.7289	0.8915	0.8517	0.9937	4
Image 3	0.1536	0.4974	0.7049	0.7760	0.7739	0.9103	3
Image 4	0.1648	0.5088	0.6790	0.7954	0.7856	1.0000	2
Image 5	0.1156	0.4067	0.2819	0.6659	0.7840	0.9589	1

Table 4.1: Quality Parameters and Quality Class for Images in Fig. 4.19

4.3 Iris Image Preprocessing

The extracted region of interest (*ROI*) of iris contains texture information but generally is of poor contrast. Suitable image enhancement technique is required to apply on the *ROI*. In order to obtain a robust representation that can tolerate small amount of illumination variation in iris images are transformed. In this section, the technique that we have used to enhance and to transform the normalized iris images is discussed.

4.3.1 Iris Image Enhancement

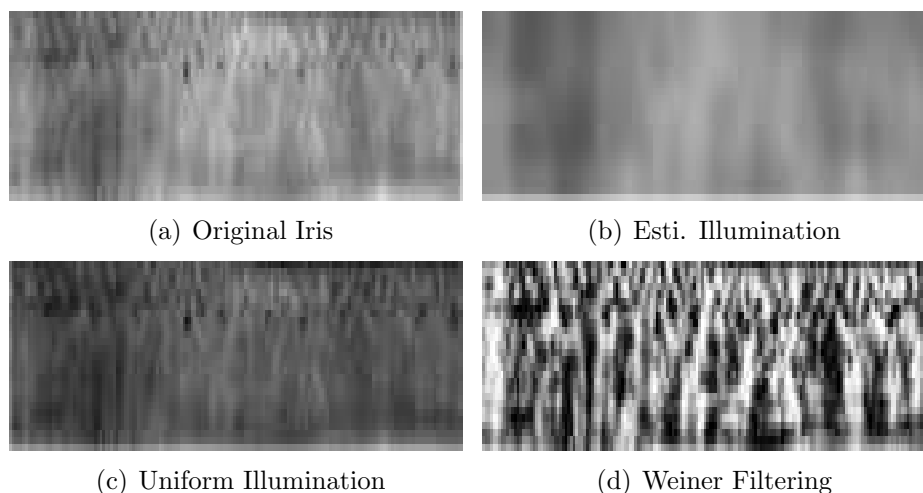


Figure 4.20: Iris Texture Enhancement

The iris texture is enhanced in such a way that it increases its richness as well as its discriminative power. The iris ROI is divided into blocks and the mean of each block is considered as the coarse illumination of that block. This mean is expanded to the original block size as shown in Fig. 4.20(b). Selection of block size plays an important role. It should be such that the mean of the block truly represents the illumination effect of the block. So, larger block may produce improper estimate. We have seen that a block size of 8×8 is the best choice for our experiment. The estimated illumination of each block is subtracted from the corresponding block of the original image to obtain the uniformly illuminated *ROI* as shown in Fig. 4.20(c). The contrast of the resultant *ROI* is enhanced using Contrast Limited Adaptive Histogram Equalization (*CLAHE*) [55]. It removes the artificially induced blocking effect using bilinear interpolation and enhances the contrast of image without introducing much external noise. Finally, Wiener filter [68] is applied to reduce constant power additive noise and the enhanced iris texture is obtained shown in Figure 4.20(d).

4.3.2 Iris Image Transformation

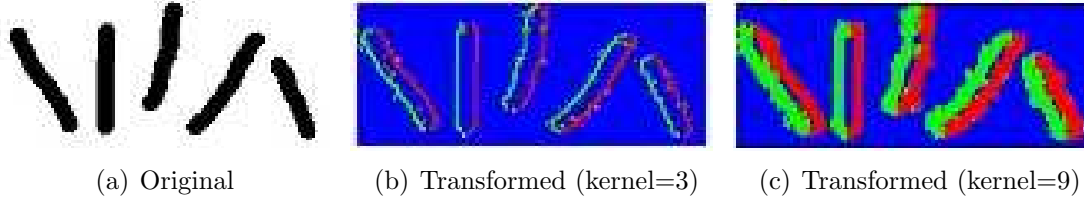


Figure 4.21: *LGBP* Transformation (Red: -ve gradient;Green: +ve grad.;Blue: zero grad.)

It transforms the iris *ROI* into a representation that can provide robust corner features. The gradient (approximated by pixel difference) of any edge pixel is positive if it lies on an edge created due to light to dark shade (*i.e. high to low gray value*) transition. Hence all edge pixels can be divided into three classes of *+ve*, *-ve* and *zero* gradient values as shown in Fig. 4.21. The *sobel* kernel fails to hold rotational symmetry; hence more consistent *scharr* kernels [61] which are obtained by minimizing the angular error is applied.

$$Scharr_x = \begin{bmatrix} 3 & 0 & -3 \\ 10 & 0 & -10 \\ 3 & 0 & -3 \end{bmatrix} \quad Scharr_y = \begin{bmatrix} 3 & 10 & 3 \\ 0 & 0 & 0 \\ -3 & -10 & -3 \end{bmatrix}$$

The *scharr* *x*-direction kernels of size 3×3 and 9×9 are applied to obtain the transformed image of Fig. 4.21(a). Resultant images are shown in Fig. 4.21(b) and 4.21(c). Bigger size kernel produces coarse level features as shown in Fig. 4.21(c). This gradient augmented information of each edge pixel can be more discriminative and robust. The transformation uses this information to calculate a 8-bit code for each pixel. It uses gradient values of *x*- direction and *y*-direction of its 8 neighboring pixels to obtain *vcode* and *hcode* respectively as discussed below.

The *vcode* and *hcode* Generation : Let $P_{i,j}$ be the $(i, j)^{th}$ pixel of any biometric image P and $Neigh[k]$, $k = 1, 2, \dots, 8$ are the gradients of 8 neighboring

pixels centered at pixel $P_{i,j}$ obtained by applying x - direction or y - direction *scharr* kernel to obtain *vcode* or *hcode* respectively. Then the k^{th} bit of the 8-bit code (termed as *lgbp_code*) is given by

$$lgbp_code[k] = \begin{cases} 1 & \text{if } Neigh[k] > 0 \\ 0 & \text{otherwise} \end{cases} \quad (4.17)$$

In *vcode* or *hcode*, every pixel is represented by its *lgbp_code* as shown in Fig. 4.22(d) and 4.22(g). The pattern of edges within a neighborhood is assumed to be robust; hence each pixel's *lgbp_code* is considered which is just an encoding of edge pattern in its 8-neighborhood. Also, *lgbp_code* of any pixel considers only the sign of the derivative within its specified neighborhood; hence it ensures the robustness of the proposed transformation in illumination variation.

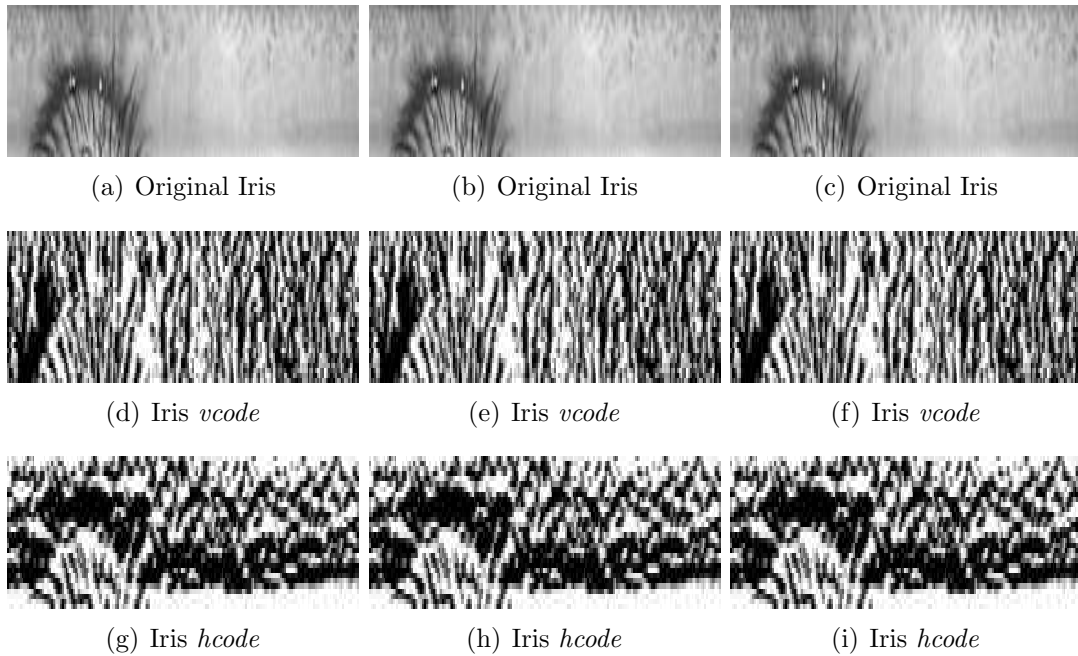


Figure 4.22: Original and Transformed (*vcode*, *hcode*) for Iris ROI's

4.4 Iris Feature Extraction and Matching

The corner features [63] are extracted from both *vcode* and *hcode* obtained from any iris *ROI*. The KL tracking [44] has been used to track the corner features in the corresponding images for matching two iris *ROIs*.

The KL tracking makes use of three assumptions, namely brightness consistency, temporal persistence and spatial coherency. Hence its performance depends completely on how well these three assumptions are satisfied. It can be safely assumed that these three assumptions are more likely to be satisfied while tracking is performed between features of same subject (genuine matching) and degrades substantially for others (imposter matching). Therefore, one can infer that the performance of KL tracking algorithm is good in genuine matching as compared to the imposter ones.

4.4.1 Corners having Inconsistent Optical Flow (CIOF)

The direction of pixel motion which termed as *optical flow* of that pixel, can be computed by KL-tracking algorithm. A dissimilarity measure *CIOF* (Corners having Inconsistent Optical Flow) has been proposed to estimate the KL-tracking performance. It evaluates two geometrical quantities for each potential matching feature pair given by KL-tracking algorithm.

[a] **Vicinity Constraints:** Euclidean distance between any corner and its estimated tracked location should be less than or equal to an empirically selected threshold (T_d), which depends upon the amount of translation and rotation in the sample images. High threshold value signifies more translation and vice-versa.

[b] **Patch-wise Dissimilarity:** Tracking error is defined as pixel-wise sum of absolute difference between a local patch centered at current corner and that of its estimated tracked location patch. This error should be less than or equal to an

empirically selected threshold (T_e), which ensures that the matching corners must have similar neighborhood patch around it.

However, all tracked corner features may not be the true matches because of noise, local non-rigid distortions in the biometric samples and also less difference in inter class matching and more in intra class matching. Hence, the direction of pixel motion (*i.e* optical flow) for each pixel is used to prune out some of the false matching corners.

Consistent Optical Flow: It can be noted that true matches have the optical flow which can be aligned with the actual affine transformation between two images that are being matched. The estimated optical flow angle is quantized into eight directions and the most consistent direction is the one which has the largest number of successfully tracked corner features. Any corner matching pair (*i.e* corner and its corresponding corner) having optical flow direction other than the most consistent direction is considered as false matching pair and has to be discarded.

4.4.2 Matching Algorithm

Given *vcode* and *hcode* of two iris, $Iris_a$ and $Iris_b$, Algorithm 4.6 can be used to compute a dissimilarity score using *CIOF* measure. The *vcode* of $Iris_a$ and $Iris_b$ are matched to obtain the vertical matching score while the respective *hcode* are matched to generate horizontal matching score. The corner features that are having their tracked position and local patch dissimilarity within the thresholds are considered as successfully tracked. Since both $Iris_a$ to $Iris_b$ and $Iris_b$ to $Iris_a$ matchings are considered, four sets of successfully tracked corners are computed *viz.* stc_{AB}^v , stc_{AB}^h , stc_{BA}^v and stc_{BA}^h . Out of these four corner sets, two correspond to vertical while other two correspond to horizontal matching. The optical flow which is the pixel motion direction is computed for each successfully tracked corner and is quantized into eight bins at an interval of $\frac{\pi}{8}$. Four histograms (of eight bins

each) are obtained, one for each set of successfully tracked corners represented by $H_{AB}^v, H_{AB}^h, H_{BA}^v$ and H_{BA}^h . The maximum value in each histogram represents the total number of corners having consistent optical flow and these are represented as $cof_{AB}^v, cof_{AB}^h, cof_{BA}^v$ and cof_{BA}^h . Finally they are normalized by the total number of corners and are converted into horizontal and vertical dissimilarity scores. The final score, $CIOF(Iris_a, Iris_b)$ is obtained by using sum rule of horizontal and vertical matching scores. Such a fusion can significantly boost-up the performance of the proposed system because some of the images are having more discrimination in vertical direction while others have it in horizontal direction.

Algorithm 4.6 $CIOF(Iris_a, Iris_b)$

Require:

- (a) The *vcode* I_A^v, I_B^v of two biometric sample images $Iris_a, Iris_b$ respectively
- (b) The *hcode* I_A^h, I_B^h of two biometric sample images $Iris_a, Iris_b$ respectively.
- (c) N_a^v, N_b^v, N_a^h and N_b^h are the number of corners in I_A^v, I_B^v, I_A^h , and I_B^h respectively.

Ensure: Return $CIOF(Iris_a, Iris_b)$.

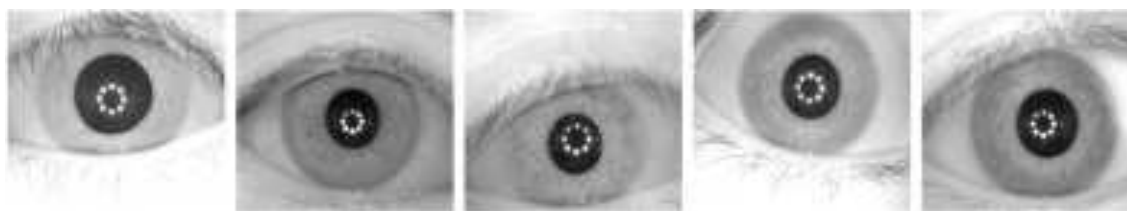
- 1: Track all the corners of *vcode* I_A^v in *vcode* I_B^v and that of *hcode* I_A^h in *hcode* I_B^h .
 - 2: Obtain the set of corners successfully tracked in *vcode* tracking (*i.e.* stc_{AB}^v) and *hcode* tracking (*i.e.* stc_{AB}^h) that have their tracked position within T_d and their local patch dissimilarity under T_e .
 - 3: Similarly compute successfully tracked corners of *vcode* I_B^v in *vcode* I_A^v (*i.e.* stc_{BA}^v) as well as *hcode* I_B^h in *hcode* I_A^h (*i.e.* stc_{BA}^h).
 - 4: Quantize optical flow direction for each successfully tracked corners into eight directions (*i.e.* at an interval of $\frac{\pi}{8}$) and obtain 4 histograms $H_{AB}^v, H_{AB}^h, H_{BA}^v$ and H_{BA}^h using these four corner set $stc_{AB}^v, stc_{AB}^h, stc_{BA}^v$ and stc_{BA}^h respectively.
 - 5: For each histogram, out of 8 bins the bin (*i.e.* direction) having the maximum number of corners is considered as the consistent optical flow direction. The maximum value obtained from each histogram is termed as corners having consistent optical flow represented as $cof_{AB}^v, cof_{AB}^h, cof_{BA}^v$ and cof_{BA}^h .
 - 6: $cof_{AB}^v = 1 - \frac{cof_{AB}^v}{N_a^v}$; [Corners with Inconsis. Optical Flow (*vcode*)]
 - 7: $cof_{BA}^v = 1 - \frac{cof_{BA}^v}{N_b^v}$; [Corners with Inconsis. Optical Flow (*vcode*)]
 - 8: $cof_{AB}^h = 1 - \frac{cof_{AB}^h}{N_a^h}$; [Corners with Inconsis. Optical Flow (*hcode*)]
 - 9: $cof_{BA}^h = 1 - \frac{cof_{BA}^h}{N_b^h}$; [Corners with Inconsis. Optical Flow (*hcode*)]
 - 10: **return** $CIOF(Iris_a, Iris_b) = \frac{cof_{AB}^v + cof_{AB}^h + cof_{BA}^v + cof_{BA}^h}{4}$;
-

4.5 Databases

Two publicly available iris databases have been used to analyze the proposed iris system. All possible inter-session matchings are done to perform various experiments.

4.5.1 Databases Used

CASIA V4 Interval Database [14]: It contains 2,639 iris images which are collected from 249 subjects. It has 395 distinct irises and contains at-most 7 images of each iris. Left and right eye of the same individual are considered as two distinct iris since these iris patterns are distinct. Iris images are taken in two sessions under controlled environment. The time gap between two sessions is at least one month. The acquired images are of resolution 320×280 and have very clear iris texture.



(a) CASIA Interval Iris Database



(b) CASIA Lamp Iris Database

Figure 4.23: Iris Images

CASIA V4 Lamp [14]: It consists of 16,212 images acquired from 411 subjects. It contains 819 distinct irises and at most 20 images of each iris. These iris images are obtained in only one session under controlled environment with lamp

on/off. The image resolution is 640×480 . These images are found to be challenging for our study because there exists nonlinear deformation due to variation of visible illumination. Also, size of this database is huge and it is a challenge to get good results on any large database because number of false acceptances grows very fast with the increase in database size [5]. For both iris databases, specifications of images are given in Table 4.2 and sample images are shown in Fig. 4.23.

Dataset	Traits	Subject	Pose	Total Imgs
CASIA-Interval	Left+Right Eye	395	7	2639
CASIA-Lamp	Left+Right Eye	819	20	16212

Table 4.2: Iris Database Specifications

4.5.2 Testing Strategy

CASIA V4 Interval database : Images of the first session are taken as training while the remaining images are used for testing. Hence a total of 3,657 genuine and 1,272,636 imposter matchings are performed for Interval database testing.

CASIA V4 Lamp database : First 10 images are considered as training while the rest are used for testing. Hence there are 78,300 genuine and 61,230,600 imposter matchings for Lamp database.

Subject	Pose	Total	Training	Testing	Genuine Match- ing	Imposter Match- ing
Casia V4 Interval (Iris)						
249 (395 Iris)	7	2,639	First 3	Rest	3,657	1,272,636
Casia V4 Lamp (Iris)						
411 (819 Iris)	20	16,212	First 10	Last 10	78,300	61,230,600

Table 4.3: Database and Testing Strategy Specifications

Default Parameters								
Db	s	t	pr_{min}	pr_{max}	ir_{min}	ir_{max}	W	$\alpha_{range}(radians)$
Interval	0.5	0.41	20	90	80	130	15	$(-\pi/4, \pi/6) \cup (5\pi/6, 5\pi/4)$
Lamp	0.5	0.125	16	70	65	120	11	$(-\pi/3, 0) \cup (\pi, 4\pi/3)$

Table 4.4: Values of Various Parameters used in Algorithm 4.1 and 4.2

Each database along with the testing strategy specifications is given in Table 4.3. One can observe that a large number of genuine as well as imposter matchings are considered to evaluate the performance of the proposed system.

4.6 Experimental Results

The experimental results of the proposed iris based authentication system are discussed in this section.

4.6.1 Iris Segmentation Analysis

The proposed iris segmentation algorithm has been used to segment iris. It has been found that the segmentation accuracy is 94.5% and 94.63% for Interval and Lamp database respectively. The parameters used for different databases are given in Table 4.4. Errors on these databases can be classified broadly into three categories:

1. Occlusion :
 - (a) Eyelid occlusion (affects outer boundary localisation)
 - (b) Eyelash occlusion (affects inner and outer boundary localisation)
2. Noise :
 - (a) Specular reflection (reflection on pupil boundary)
 - (b) Pupil Boundary Noise (Non-circular pupil shape or noise points)

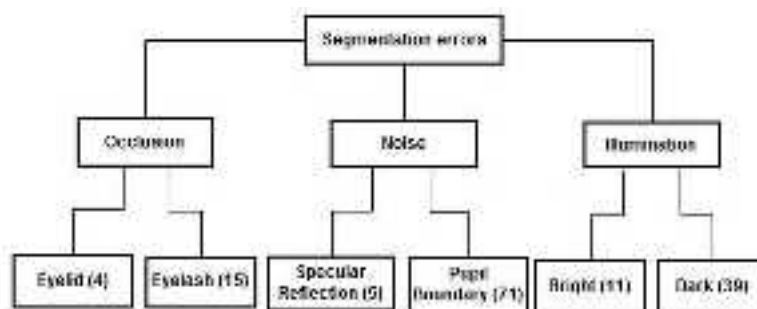


Figure 4.24: Segmentation Error Hierarchy (Numbers Mentioned for each Subcategory Specify the Number Images of that Category for Interval Database.)

Threshold parameter (t) value				
Sub-Category	Mean	Minimum	Maximum	Standard Deviation
Eyelid	0.39	0.36	0.41	0.022
Eyelash	0.39	0.3	0.43	0.040
Specular Reflection	0.44	0.36	0.5	0.066
Pupil Boundary Noise	0.4	0.26	0.5	0.056
Bright image	0.46	0.35	0.52	0.06
Dark image	0.36	0.25	0.51	0.052

Table 4.5: Variation in Threshold needed for Correct Segmentation

3. Illumination :

- (a) Bright image (excess illumination)
- (b) Dark image (lack of illumination)

The hierarchy of errors is shown in Figure 4.24. There are only two critical parameters viz. threshold (t) and angular range (α_{range}) that are required to be adjusted as suggested in Table 4.5 and Table 4.6 for accurate segmentation. The erroneous segmentations are critically analyzed and are corrected by adjusting these parameters. This adjustment helps to achieve an accuracy of more than 99.6% for both the databases. Some very critically occluded images are segmented manually ($< 0.4\%$). Some of the images where the proposed algorithm has been failed are

Sub-Category	t	α_{range}
Eyelid	-	↓
Eyelash	↓-	↓
Specular Reflection	↑	-
Pupil Boundary Noise	↑↓	-
Bright image	↑	-
Dark image	↓	-

Table 4.6: Required Parametric Variations: '-' stands for no change, '↑' stands for increasing and '↓' for decreasing the parameter value

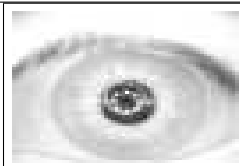
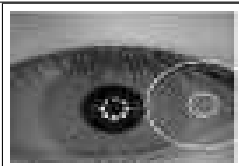
Eyelid Occlusion	Eyelash Occlusion	Specular Reflection
		
Interval=4,Lamp=300	Interval=15,Lamp=288	Interval=5,Lamp=68
Pupil Noise	Bright Image	Dark Image
		
Interval=71,Lamp=160	Interval=11,Lamp=1	Interval=39,Lamp=53

Table 4.7: Segmentation Error. (Rows Below Images: Errors Occurred in Interval, Lamp Databases)

shown in Table 4.7.

4.6.2 Threshold Selection

Matching performance has been obtained by varying two thresholds used to compute *CIOF* dissimilarity measure. These values for any database are selected in such a way that the performance of the system is maximized over the validation set, using only *vcode* matching. The validation set contains images of first 100 subjects only

T_d	T_e	DI	EER(%)	Accuracy(%)	EUC	CRR(%)
Casia V4 Interval Iris Database						
6	500	1.596	0.87499	99.368	0.2496	99.8359
7	550	1.8290	0.4102	99.7221	0.06821	99.9179
8	500	1.7033	0.24606	99.766	0.0138	100
8	550	1.8843	0.2187	99.8250	0.00912	100
9	500	1.7247	0.2734	99.7830	0.01551	100
9	550	1.9120	0.2187	99.8191	0.011963	100
9	600	2.0519	0.2187	99.80	0.0048	100
10	500	1.7351	0.2460	99.7836	0.010	100
10	550	1.9272	0.1677	99.832	0.0068	100
10	600	2.069	0.1659	99.837	0.0052	100
11	500	1.7398	0.1958	99.804	0.0029	100
11	600	2.077	0.2151	99.798	0.0071	100
12	500	1.7412	0.2461	99.7975	0.0040	100
12	550	1.9361	0.2450	99.8096	0.0051	100
Casia V4 Lamp Iris Database						
5	600	1.999	0.7619	99.4087	0.1772	100
5	700	2.2760	0.8571	99.3399	0.1729	99.8412
5	800	2.3272	1.2388	98.9611	0.2888	99.6825
7	600	2.0072	0.741992	99.4653	0.1418	100
7	700	2.2787	0.8714	99.3229	0.1592	99.8412
7	800	2.3062	1.3491	99.7938	0.2904	99.3650

Table 4.8: Threshold Selection for CASIA V4 Interval and Lamp Iris Database using only *vcode* Matching over Validation Set of First 100 Subjects.

from that database. One threshold T_e [used for patch-wise dissimilarity] depends upon the patch size while other one T_d [used for vicinity constraints] depends upon the amount of affine transformation in between database images; hence it varies for different databases.

The typical value of T_d for the system with maximum CRR and minimum EER is 7 for Lamp and 10 for Interval database with $T_e = 600$ having patch size of 5×5 . The results are shown in Fig. 4.26, Fig. 4.25 along with Table 4.8. This analysis has inferred that Interval database has more affine transformation in iris images of

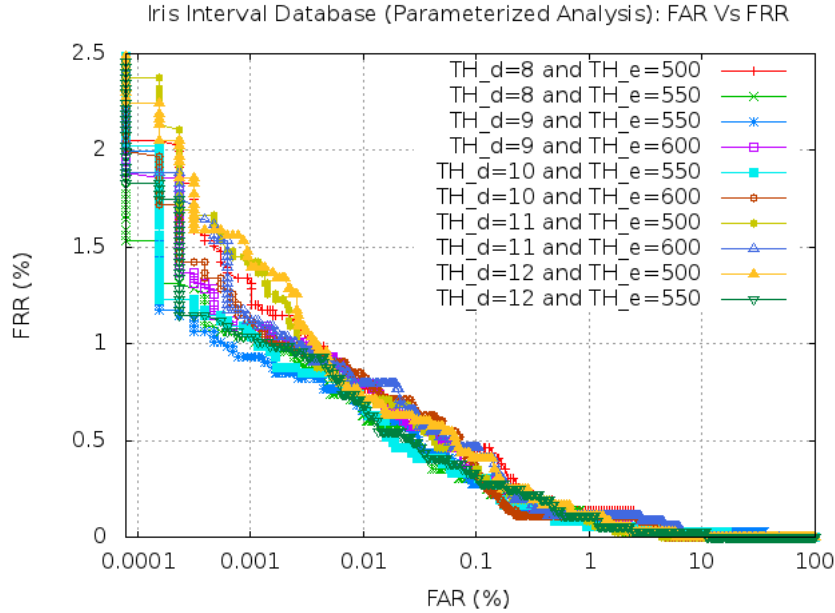


Figure 4.25: Parameterized ROC Curve of the Proposed System for Iris Interval Database (only *vcode* matching)

Description	DI	EER(%)	Accuracy(%)	EUC	CRR(%)
<i>vcode</i>	1.9663	0.4375	99.657	0.0433	99.917
Enhanced <i>vcode</i>	2.069	0.1659	99.837	0.0052	100
<i>hcode</i>	1.387	2.761	97.481	0.4782	99.343
Enhanced <i>hcode</i>	1.701	0.6835	99.357	0.0539	99.7538
<i>fusion</i>	1.8637	0.3280	99.719	0.026	99.917
Enhanced <i>fusion</i>	2.0182	0.1093	99.910	0.0009	100

Table 4.9: Enhancement based Performance boost-up over Iris Interval Databases (In the above Table fusion referred as *vcode+hcode*)

same subject than Lamp database.

4.6.3 Impact of Enhancement on System Performance

This section analyses the impact of enhancement on system performance boost-up over CASIA V4 Iris Interval [14] database to justify the use of enhancement

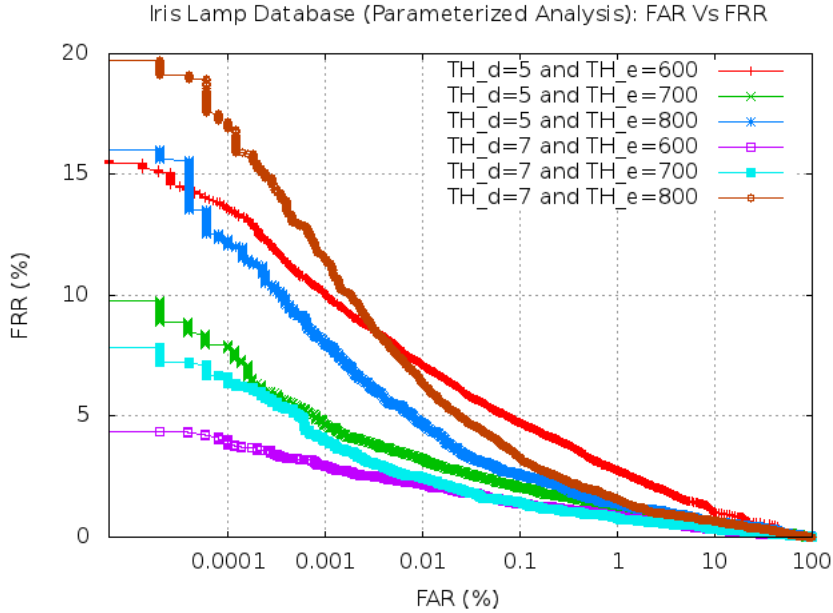


Figure 4.26: Parameterized *ROC* Analysis of the Proposed System for Iris Lamp Database (only *vcode* matching)

algorithm. It is observed that the enhancement method significantly improves the iris texture as evident from the graphs shown in Fig. 4.27 and Table 4.9. From ROC curve, it is seen that for *vcode*, *hcode* or fusion, the performance of the system is significantly improved after enhancement. One can observe clearly how the proposed enhancement can boost-up the dissimilarity score of imposters which reduces the errors effectively. From Table 4.9, it can be seen that *EER* obtained using *hcode* only is reduced by a factor of 4 times (*i.e* from 2.761% to 0.684%) and similar improvement has been observed in the case of *vcode* and *fusion* approaches.

4.6.4 Comparative Analysis

It is seen from Table 4.10 that *CRR* (**Rank 1** accuracy) of the proposed system is 100% and 99.87% for Interval and Lamp databases respectively. Further, *EER* for Interval and Lamp are 0.109% and 1.3% respectively. It can also be observed

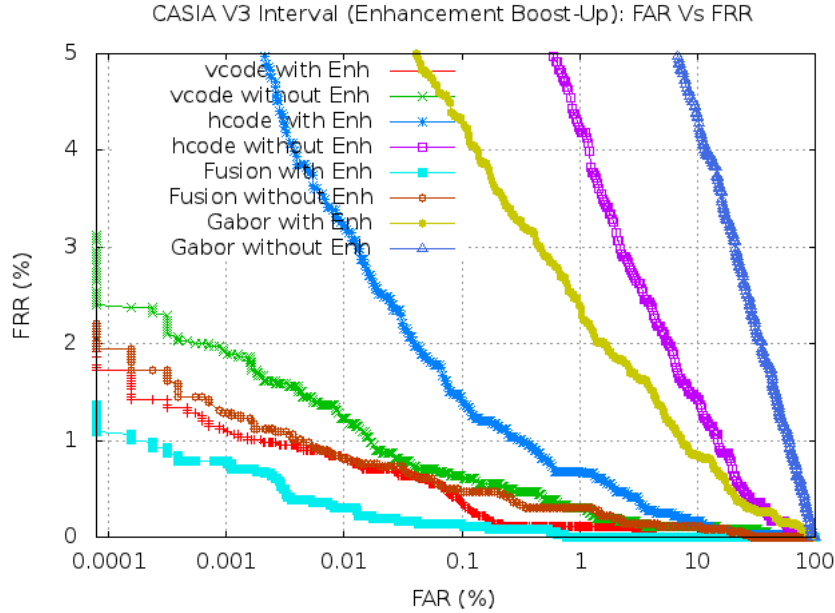


Figure 4.27: Enhancement based Performance boost-up in terms of Receiver Operating Characteristic Curves for the Proposed System

Database	Performance Parameters				
	DI	CRR%	EER%	Accuracy%	EUC
Interval	2.018	100	0.109	99.91	0.0009
Lamp	1.50	99.87	1.30	98.85	0.240

Table 4.10: Performance Analysis of Proposed System

that the genuine and the imposter scores are well separated as the decidability index is found to be 2.02 and 1.50 for Interval and Lamp databases respectively. *Accuracy* and error under the curve, *EUC*, for Interval and Lamp are observed as 99.91, 0.001 and 98.85, 0.24 respectively that can be considered as good for any verification system.

The proposed system has been compared with state-of-the-art iris recognition systems [19],[45],[46],[60]. We have implemented the systems proposed in [19],[46] while we have used the results stated in [60] of the systems in [45],[60]. The compar-

Systems	Interval		
	DI	CRR%	EER%
Daugman [19]	1.96	99.46	1.88
Li Ma [60]	-	95.54	2.07
Masek [46]	1.99	99.58	1.09
K. Roy [60]	-	97.21	0.71
Proposed	2.02	100	0.109
	Lamp		
Daugman [19]	1.2420	98.90	5.59
Proposed	1.50	99.87	1.300

Table 4.11: Comparative Performance Analysis over CASIA V4 Interval and Lamp Iris Database

Comparison of the proposed system with other state-of-the-art systems is shown in Table 4.11. The performance of the proposed system is found to be better than the reported systems. For both Interval and Lamp iris databases, Receiver Operating Characteristics (*ROC*) curves of the proposed system are shown in Fig. 4.28 and Fig. 4.29 respectively. *ROC* curves of the proposed system are compared with the open source Masek's system (Log-Gabor) [46] and Daugman's system (Gabor) [19]. It is observed that *vcode* results are always better than *hcode* results. Also fusion of *vcode* and *hcode* performs much better than *vcode* alone. This performance gain occurs because there are several images that are mis-classified as genuine or imposter by *vcode* features, but its corresponding *hcode* contains discrimination. Hence the ability of discrimination of fused score is enhanced. The Masek's system has not been tested on Lamp database as the optimal parameters are not known and with default set of parameters, it has performed very poorly.

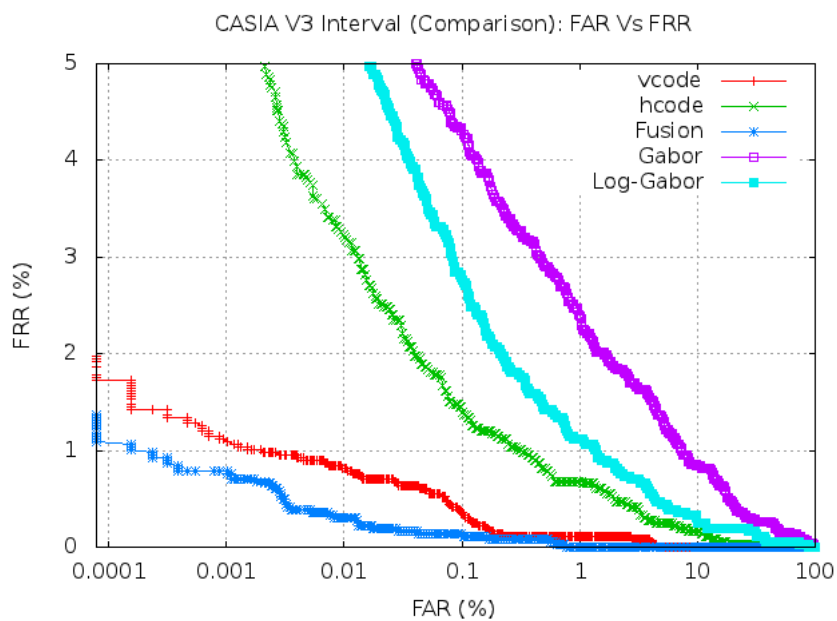


Figure 4.28: Comparative Analysis of Proposed System over Interval Database

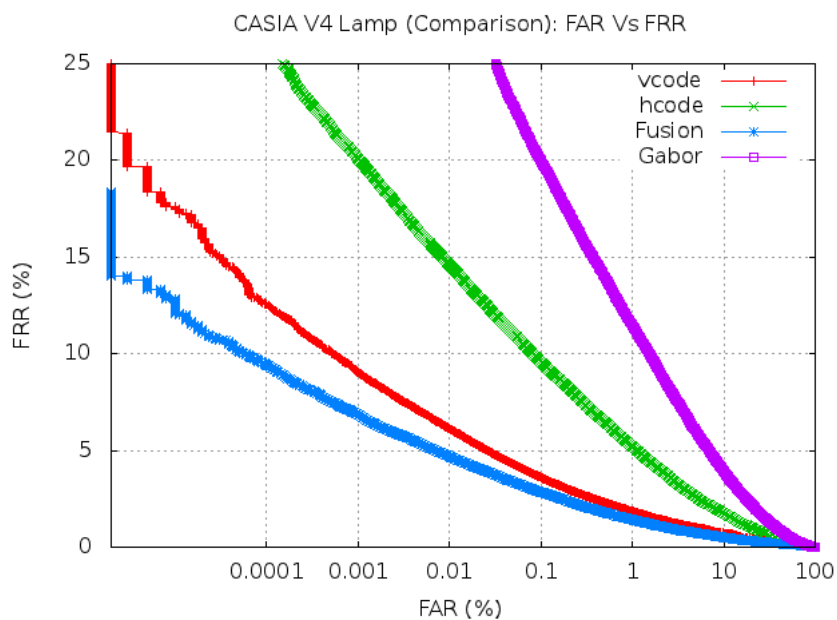


Figure 4.29: Comparative Analysis of Proposed System over Lamp Database

Chapter 5

Knuckleprint Recognition System

This chapter deals with the problem of designing an efficient knuckleprint based recognition system. The knuckleprint ROI is extracted by applying a modified version of gabor filter to estimate the central knuckle line and point as shown in Fig. 5.2(b). The central knuckle point is used to extract consistently the knuckleprint ROI from any image. The vertical and horizontal knuckle line based features may be of poor quality; hence they are required to be enhanced and transformed to achieve robustness against varying illumination. It consists of five major tasks, *viz.* ROI extraction, quality estimation, ROI preprocessing, feature extraction and matching. The overall architecture of the proposed knuckleprint based recognition system is shown in Fig. 5.1. The publicly available knuckleprint PolyU database [56] is used to test the proposed system. The PolyU database contains images that are acquired using normal web-cam of resolution 384×288 using their indigenous capturing device. The device allows the user to place only one finger at a time and acquires images that are horizontally aligned images. Therefore, at the time of ROI extraction, raw knuckleprint images are assumed to be horizontal and contain single finger knuckle.

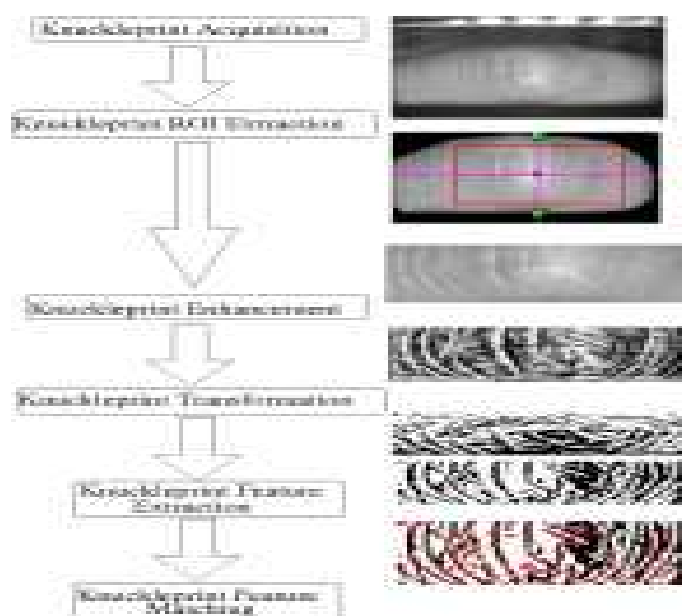


Figure 5.1: Overall Architecture of the Proposed Knuckleprint Recognition System

5.1 Knuckleprint ROI Extraction

This section proposes an efficient knuckleprint ROI extraction technique. The prime objective of any ROI extraction technique is to segment some region of interest consistently from all images. The central knuckle point as shown in Figure 5.2(b) can be used to segment any knuckleprint. Since knuckleprint is aligned horizontally, one can easily extract the central region of interest from any knuckleprint that contains rich and discriminative texture as shown in Fig. 5.2(c). The proposed ROI extraction algorithm performs in three steps; detection of knuckle area, central knuckle-line and central knuckle-point.

5.1.1 Knuckle Area Detection

In this step, the whole knuckle area is segmented from the background to discard background region. The acquired knuckleprint may be of poor quality. Each such

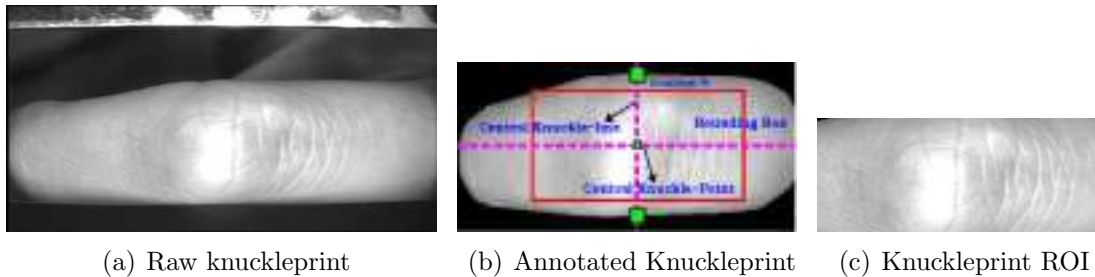


Figure 5.2: Knuckleprint ROI Annotation

knuckleprint is enhanced using contrast limited adaptive histogram equalization [55] (CLAHE) to obtain better edge representation which helps to detect the knuckle area. CLAHE divides the whole image into blocks of size 8×8 and applies histogram equalization over each block. The enhanced image is binarized using Otsu thresholding that segments the image into two clusters (knuckle region and background region) based on their gray values. Such a binary image is shown in Fig. 5.3(b). It can be observed that the knuckle region may not be accurate because of sensor noise and background clutter. This can be obtained by using canny edge detection. A resultant image is shown in Fig. 5.3(c) and the largest connected component is considered as the required knuckle boundary. The detected boundary is eroded to smoothen it as well as to remove any discontinuity as shown in Fig. 5.3(d). Finally all pixels within the convex hull of the knuckle boundary are considered as the knuckle area. Figure 5.3(e) shows a knuckle area. Some top and bottom rows are assumed to be background and are discarded from the raw image.

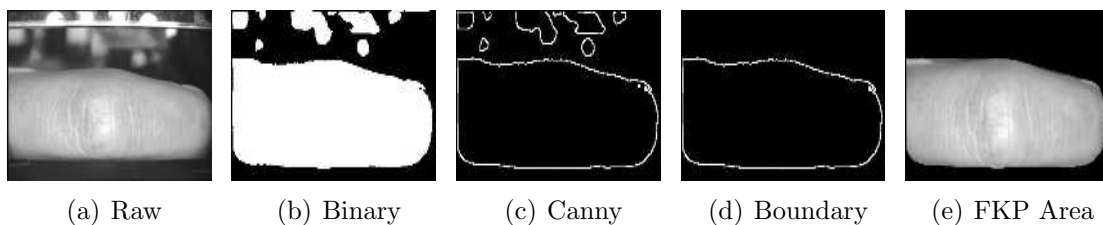


Figure 5.3: Knuckle Area Detection

5.1.2 Central Knuckle-Line Detection

The central knuckle line is defined as that column of the image with respect to which the knuckle can be considered as symmetric. It can be observed from Figure 5.2(b). This line is used to extract the knuckleprint ROI. A very specific and symmetric texture is observed around the central knuckle line which is used for its detection. To perceive such a specific texture, a knuckle filter is created by modifying the gabor filter which is defined below.

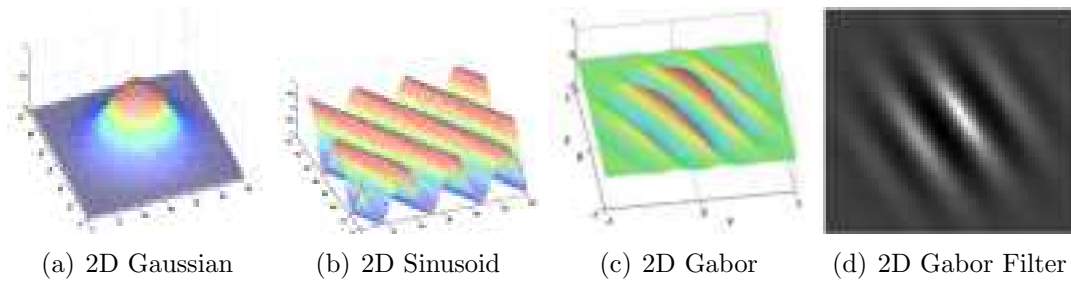


Figure 5.4: Conventional Gabor Filter

[A] **Knuckle Filter** : The conventional gabor filter is created when a complex sinusoid is multiplied with a Gaussian envelope as defined in Eq .(5.1) and is shown in Figure 5.4(c).

$$G(x, y; \gamma, \theta, \psi, \lambda, \sigma) = \underbrace{e^{-\left(\frac{X^2+Y^2 \cdot \gamma^2}{2 \cdot \sigma^2}\right)}}_{\text{Gaussian Envelope}} \times \underbrace{e^{i\left(\frac{2\pi X}{\lambda} + \psi\right)}}_{\text{Complex Sinusoid}} \quad (5.1)$$

where x and y are the spatial co-ordinates of the filter and X, Y are obtained by rotating x, y by an angle θ using the following equations :

$$X = x * \cos(\theta) + y * \sin(\theta) \quad (5.2)$$

$$Y = -x * \sin(\theta) + y * \cos(\theta) \quad (5.3)$$

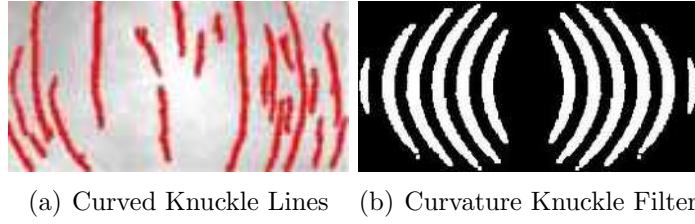


Figure 5.5: Curvature Knuckle Filter

In order to model the curved convex knuckle lines, a knuckle filter is obtained by introducing curvature parameter in the conventional gabor filter. The basic gabor filter equation remains to be the same (as in Eq. (5.1)). Only X and Y co-ordinates are modified as follows :

$$X = x * \cos(\theta) + y * \sin(\theta) + c * (-x * \sin(\theta) + y * \cos(\theta))^2 \quad (5.4)$$

$$Y = -x * \sin(\theta) + y * \cos(\theta) \quad (5.5)$$

The curvature of the gabor filter can be modulated by the curvature parameter. This curved gabor filter with parameters ($\gamma = 1, \theta = \pi, \psi = 1, \lambda = 20, \sigma = 20$) is used for knuckle filter creation. The value of curvature parameter is varied as shown in Fig. 5.6 and its optimal value for our database is selected heuristically. The proposed knuckle filter is obtained by concatenating two such curved gabor filters (f_1, f_2) ensuring that the distance between them is d . The first filter (f_1) is obtained using the above mentioned parameters while the second filter ($f_2 = f_1^{flip}$) is just the vertically flipped version of the first filter because knuckleprints are vertically symmetric. In Figure 5.6, several knuckle filters are shown with varying curvature and distance parameters. One can observe that increasing curvature parameter (c) introduces more and more curvature in the filter. Finally $c = 0.01$ and $d = 30$ are considered in the knuckle filter ($F_{kp}^{0.01,30}$).

[B] Knuckle Line Extraction : All pixels belonging to knuckle area are con-

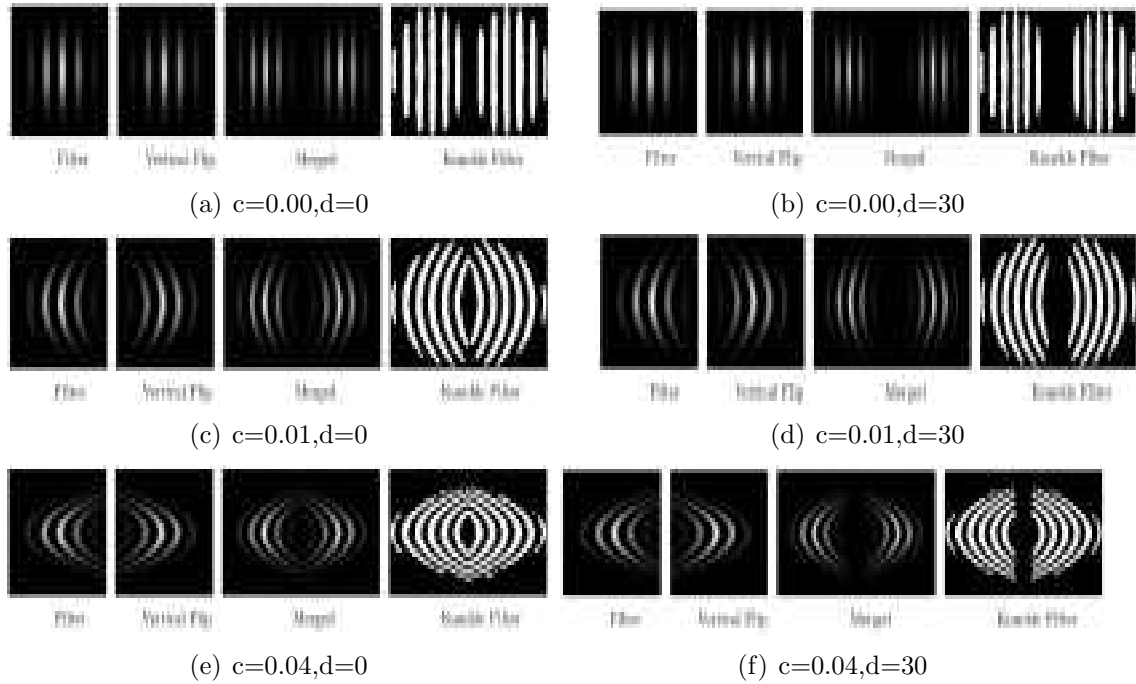


Figure 5.6: Knuckle Filter

involved with the knuckle filter $F_{kp}^{0.01,30}$. Pixels over the central knuckle line must be having the higher response as compared to others because of filter's shape and construction. The filter response for each pixel is binarized using threshold as $f * max$ where max is the maximum knuckle filter response and $f \in 0$ to 1 is a fractional value. The binarized filter response is shown in Fig. 5.7(a) in which it is super imposed over knuckle area with blue color. The column-wise sum of the filter response for each column is computed. The central knuckle line is considered as that column which is having the maximum knuckle filter response as shown in Fig. 5.7(b).

5.1.3 Central Knuckle-Point Detection

The central knuckle point is required to crop the knuckle-print ROI that must lie over central knuckle line. Hence the top and the bottom point over central knuckle line, belonging to the knuckle area, are computed and their mid-point is considered

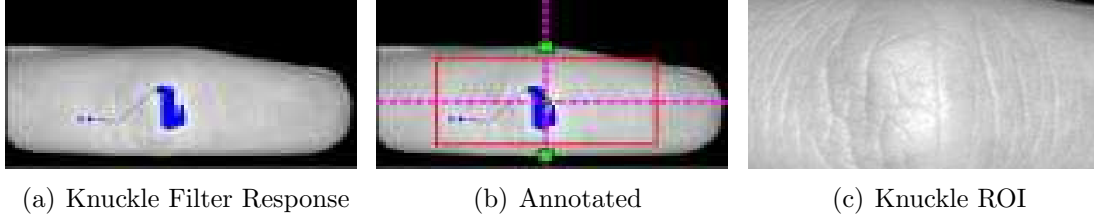


Figure 5.7: Knuckleprint ROI detection. (a) Knuckle filter response is super impose over the knuckle area with blue color, (b) Full Annotated and (c) FKP (FKP_{ROI})

as the central knuckle point. It is shown in Figure 5.7(b). The required knuckleprint ROI is extracted as a region of size $(2 * w + 1) \times (2 * h + 1)$ considering central knuckle point as the center. It is shown in Fig. 5.7(c).

Algorithm 5.1 Knuckleprint ROI Detection

Require:

Raw Knuckleprint image I of size $m \times n$.

Ensure:

The knuckleprint ROI FKP_{ROI} , of size $(2 * w + 1) \times (2 * h + 1)$.

- 1: Enhance the FKP image I to I_e using CLAHE;
 - 2: Binarize I_e to I_b using Otsu thresholding;
 - 3: Apply Canny edge detection over I_b to get I_{edges} ;
 - 4: Extract the largest connected component in I_{edges} as FKP raw boundary, (FKP_{Bound}^{raw});
 - 5: Erode the detected boundary FKP_{Bound}^{raw} to obtain continuous and smooth FKP boundary, FKP_{Bound}^{smooth} ;
 - 6: Extract the knuckle area $K_a = \text{All pixels in image } I \in \text{the } ConvexHull(FKP_{Bound}^{smooth})$;
 - 7: Apply the knuckle filter $F_{kp}^{0.01,30}$ over all pixels $\in K_a$;
 - 8: Binarize the filter response using $f * max$ as the threshold;
 - 9: The central knuckle line (c_{kl}), is assigned as that column which is having the maximum knuckle filter response;
 - 10: The mid-point of top and bottom boundary points over $c_{kl} \in K_a$, is defined as the central knuckle point (c_{kp}).
 - 11: The knuckle ROI (FKP_{ROI}) is extracted as the region of size $(2 * w + 1) \times (2 * h + 1)$ from raw knuckleprint image I , considering c_{kp} as its center point.
-

Given a raw knuckleprint image I , Algorithm 5.1 can be used to extract the knuckleprint ROI (FKP_{ROI}) from it. Some of the segmented PolyU knuckleprint

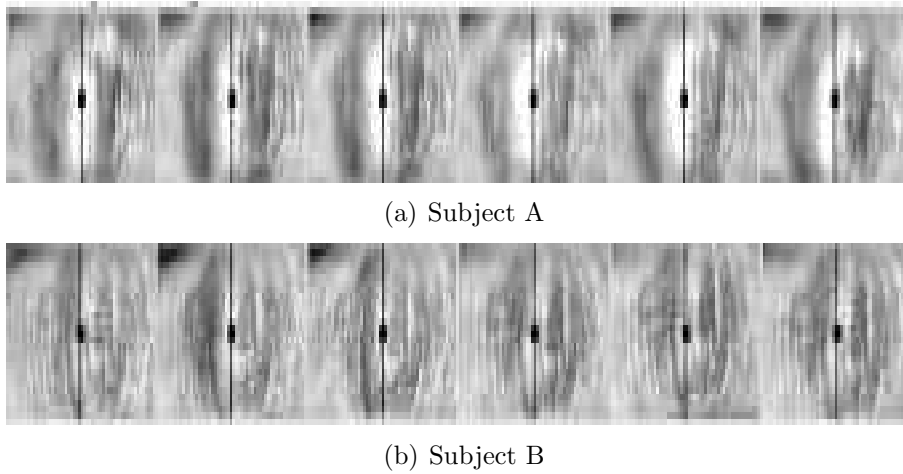


Figure 5.8: Some Segmented Knuckleprints

database images are shown in Fig. 5.8. One can observe that the proposed algorithm can extract consistently the ROI of images in the database.

5.2 Knuckleprint Image Quality Extraction

The images acquired from the sensors have inevitably wide distribution of quality. Hence quality assessment should be done during early phases such as data acquisition so that one can discard the bad quality images and recapture the better one. Also quality parameters can reveal the type of deficiency in the image which can be used to apply the suitable enhancement technique to reduce its effect. The image quality of knuckleprint is degraded mostly due to fewer or blurred line like features, defocus, poor contrast and high or low illumination and reflection produced by the camera flash as shown in Fig.5.9. In this section an algorithm has been proposed for knuckleprint quality assessment.

Quality of the knuckleprint image has been modeled as a function of the following six attributes: Focus (F), Clutter (C), Uniformity (S), Entropy (E), Reflection (Re), Contrast and Illumination (Con). Hence overall quality of the knuckleprint

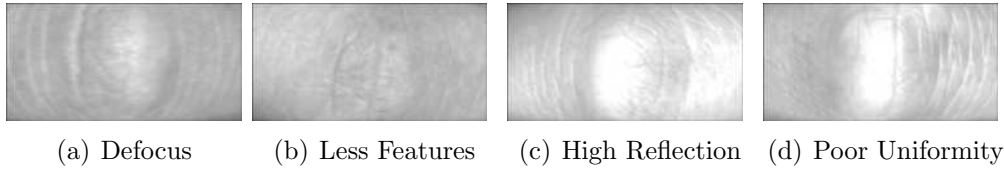


Figure 5.9: Poor Quality Knuckleprint ROI Samples

image can be represented by

$$Quality = f(F, C, S, E, Re, Con) \quad (5.6)$$

where f is a function which is learned from the training data using a Support Vector Machine (SVM). Quality attributes from the training set of knuckleprints along with their respective true quality label are used to train the SVM classifier. This creates a model based classifier which can be used to predict the quality of a knuckleprint image using its quality attributes. The six quality attributes, are amount of well focus edges \mathbf{F} , amount of clutter \mathbf{C} , distribution of focused edges \mathbf{S} , block-wise entropy of focused edges \mathbf{E} , reflection caused by light source and camera flash \mathbf{Re} and the amount of contrast \mathbf{Con} .

The most important and vital features in knuckleprint images are vertical long edges (\mathbf{vle}) as shown in Fig. 5.10(a); hence most of the quality parameters tend to analyse initially \mathbf{vle} for knuckleprint quality assessment. The set of pixels that corresponds to only vertical strong edge pixels is computed using sobel y -direction kernel from the input image (I) and the connected components are computed. Finally, out of all connected components, only long components (more than an empirically selected threshold t_{cc}) are retained that constitute the set of pixels which are “long” and vertical termed as \mathbf{vle} .

5.2.1 Focus (F)

The defocus blurring effect occurs when the focal point of the sensor's lens is not at the reference object during image acquisition as shown in Fig. 5.9(a). The frequency analysis of defocus images has revealed that its 2D Fourier spectrum is usually dense towards lower frequencies while well focused image possesses uniform spectrum. The number of well focused edge pixels is considered for quality assessment. It is computed by convolving the image by the proposed 6×6 kernel K as defined in Eq (5.7) that can well approximate the 2D Fourier spectrum's high frequency band pass filter. Then only those pixels are retained that are well focused (*i.e* having convolved value more than an empirically selected threshold t_f) constituting the set of pixels which are well focused, termed as wf , as shown in Fig. 5.10(b).

$$K = \begin{pmatrix} 1 & 1 & 1 & 1 & 1 & 1 \\ 1 & 1 & 1 & 1 & 1 & 1 \\ 1 & 1 & -8 & -8 & 1 & 1 \\ 1 & 1 & -8 & -8 & 1 & 1 \\ 1 & 1 & 1 & 1 & 1 & 1 \\ 1 & 1 & 1 & 1 & 1 & 1 \end{pmatrix} \quad (5.7)$$

The set of pixels F_{map} obtained by taking the set intersection of pixel sets vle and wf , as shown in Fig. 5.10(c) is later used as the most significant region. Finally, focus quality parameter F is defined as the number of well focused vertically aligned long edge pixels which is computed by counting the number of pixels in F_{map} .

5.2.2 Clutter (C)

The short vertical edge pixels that are well focused can be considered as clutter as shown in Fig. 5.10(d) because that can degrade the quality of the image. They are usually present due to abrupt discontinuity in the edge structure due to several

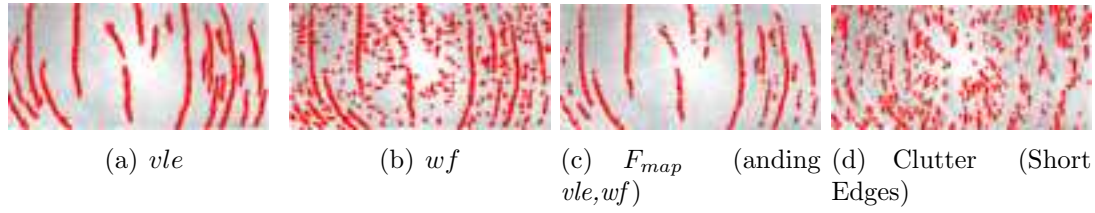


Figure 5.10: Defocus based Quality Attribute F and C

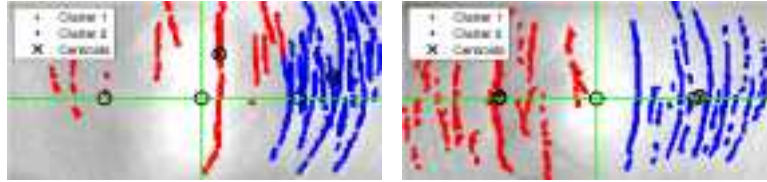
possible extrinsic factors. Clutter creates false features that can confuse any recognition algorithm. The quality parameter, clutter (C), is defined as the ratio of short vertically aligned strong edge pixels to the longer ones. It is inversely proportional to the image quality.

5.2.3 Uniformity based Quality Attribute (S)

In any good quality image, the texture based features should be distributed uniformly through out the whole image. There are several images in the database that are having well focused left or right half only. Some images are shown in Fig. 5.9(d). The focus parameter F may consider as good quality even though half of the image is of very poor quality. Hence uniformity in texture distribution should be given some importance. The quality attribute (S) is proposed which is directly proportional to the uniformity in texture distribution as shown in Fig. 5.11. The pixel set F_{map} as defined in focus parameter is clustered using K-Means algorithm using $K = 2$, because knuckleprint images have some symmetry along Y - axis. Some statistical and geometrical parameters of the two clusters that are obtained as output of 2-mean clustering, are used to obtain the value of S and are described in Algorithm 5.2.

Algorithm 5.2 Uniformity based Quality Attribute (S)**Require:** The vle and wf pixel set for the input image (I) of size $m \times n$.**Ensure:** Return the value S for the input image (I).

1. $F_{map} = and(wf, vle); [focus\ mask]$
2. $M_1, M_2 = \text{Mid-point of Left half } (\frac{n}{2}, \frac{n}{2}) \text{ and Right half } (\frac{m+n}{2}, \frac{n}{2})$ of the input image (I);
3. Apply 2-Mean Clustering over pixel set F_{map} ;
4. $C_1, C_2, nc_1, nc_2, std_1, std_2 = \text{Mean loc., Number of pixels and Standard dev. of Left and Right cluster respectively};$
5. $d_1, d_2 = \text{Euclidean Distance between point } C_1 \text{ and } M_1 \text{ and that of between } C_2 \text{ and } M_2 \text{ respectively};$
6. $d = 0.7 * max(d_1, d_2) + 0.3 * min(d_1, d_2);$
7. $p_r = \frac{max(nc_1, nc_2)}{min(nc_1, nc_2)}; [\text{Cluster Point Ratio}]$
8. $std_r = \frac{max(std_1, std_2)}{min(std_1, std_2)}; [\text{Cluster Standard Dev. Ratio}]$
9. $comb_r = 0.8 * p_r + 0.2 * std_r;$
10. $D_{std} = 1 - \frac{d}{\sqrt{std_1^2 + std_2^2}};$
11. $D_{nc} = 1 - \frac{d}{\sqrt{nc_1^2 + nc_2^2}};$
12. $S = 0.5 * d + 0.2 * comb_r + 0.15 * D_{std} + 0.15 * D_{nc}$



(a) Non Uniform Texture (0.221) (b) Uniform Texture (0.622)

Figure 5.11: Uniformity based Quality Attribute (S)**5.2.4 Entropy based Quality Attribute (E)**

The most common statistical measure that is used to quantify the amount of information in any gray scale image (I) is the entropy value defined by:

$$e = - \sum_{i=0}^{255} hist[i] * \log(2 * hist[i]) \quad (5.8)$$

where $hist[i]$ is the i^{th} element of the 256 valued gray level histogram, $hist$, of the input image I . The image is divided into blocks of size 5×5 and block-wise entropy is calculated using Eq. (5.8) (as shown in Figs. 5.12(b) and 5.12(e)). Since all blocks do not carry the same amount of importance, only blocks that are having well focused long vertically aligned edge pixels (using F_{map} as defined in Section 5.2.1) more than a predefined empirically selected threshold t_{fm} are considered as significant blocks. Finally, the entropy based quality attribute (E) is obtained by summing up the entropy values of all significant blocks. They are shown in Figs. 5.12(c) and 5.12(f).

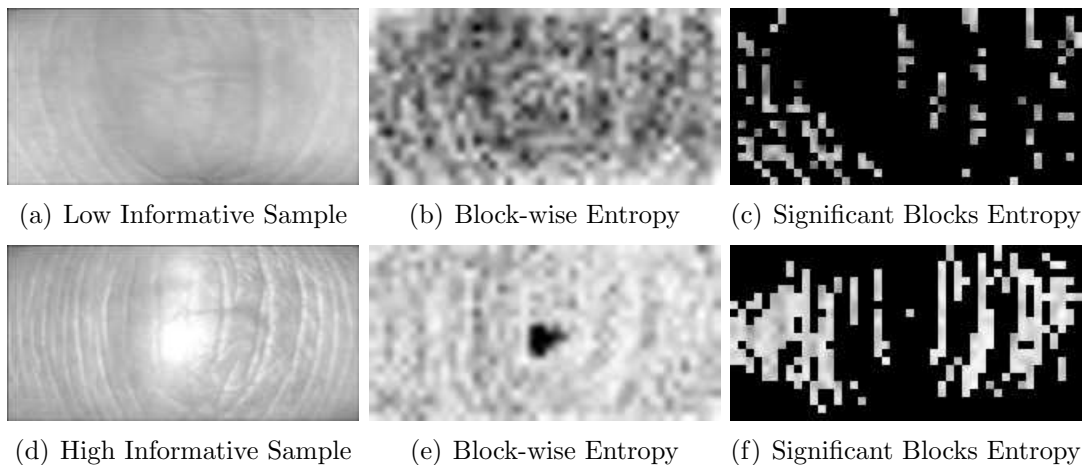


Figure 5.12: Entropy based Quality Attribute E

5.2.5 Reflection based Quality Attribute (Re)

High reflection can be caused due to light source or camera flash and creates a patch of very high intensity gray values. The unique line based information within this patch is completely ruined leading to severe image quality degradation. This reflection patch is identified by using adaptive thresholding and it can be ignored while matching. The sample knuckleprint is repeatedly thresholded to estimate the most accurate reflection patch intensity level, starting from a high gray level and

gradually reducing it. After each thresholding step, number of pixels that are having gray value more than the threshold is calculated. This count keeps on changing significantly because some of the nearby area around the reflection patch may not be captured by the previous threshold. This thresholding procedure gets terminated when this count is saturated (*i.e* when the difference in the count before and after thresholding is less than an empirically selected value t_r). After termination, the full reflection patch is identified. It is shown in Fig. 5.13(b). The reflection based quality attribute (Re) is defined as the fraction of pixels belonging to the reflection patch; hence it is inversely proportional to the image quality.

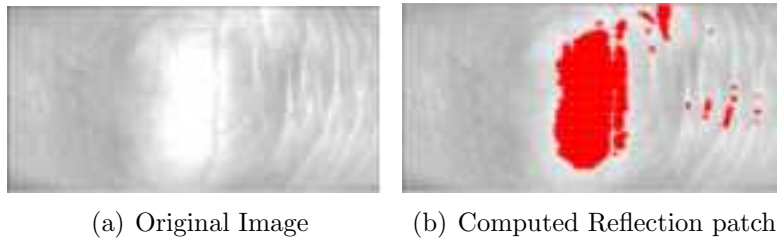


Figure 5.13: Reflection based Quality Attribute Re

5.2.6 Contrast based Quality Attribute (Con)

Often quality of the knuckleprint image gets severely affected by very poor or rich lighting condition. Large illumination variation can reduce the discriminative line based features and hence can degrade the overall uniqueness of biometric images. The contrast of the input image (I) can give some information about the dynamic gray level range present in the image. Hence, it can be used to infer that image is either too dark or light. Basically, we can use it to estimate the uniformity in illumination through-out the image. The whole gray level range is divided into three groups $(0, 75)$, $(76, 235)$, $(236, 255)$. The contrast based quality attribute (Con) is defined as the fraction of pixels belonging to the mid gray level range (*i.e* $(76, 235)$) because it indicates the moderated intensity range.

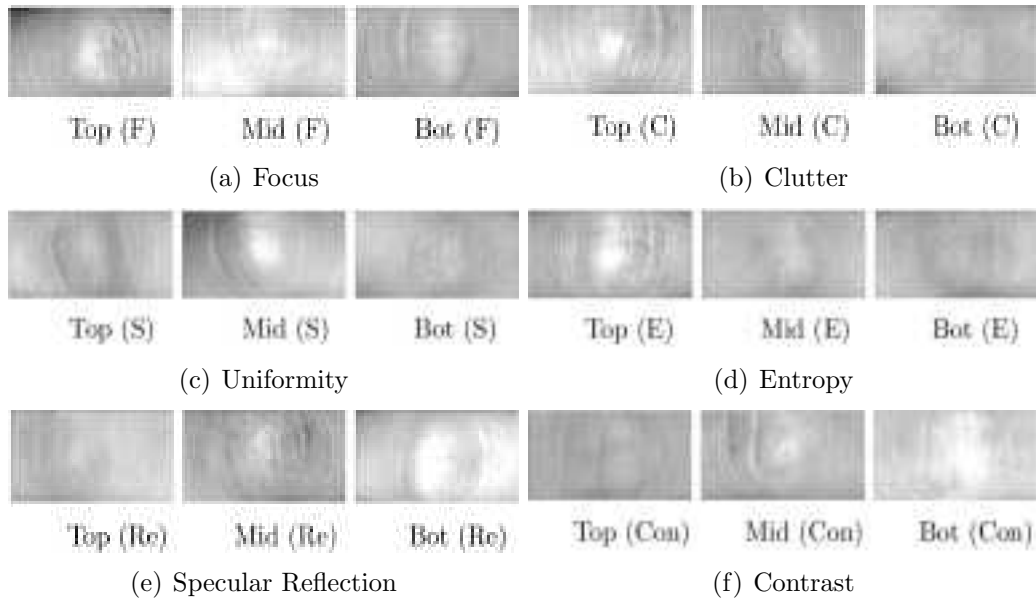


Figure 5.14: Knuckleprint Quality Estimation. Top, Middle, Bottom Images for each Proposed Quality Parameter.

5.2.7 Quality Class Determination

Similar to the iris quality attribute fusion as discussed in Section 4.2.7, Support Vector Machine (*SVM*) is trained using images from first 100 subjects from the database. The actual quality classes (*i.e* ground truth) in the training set of images are assigned manually. This set of quality attributes along with the quality class label of the knuckleprint image is used to train the *SVM* to learn the function f as defined in Eq. (5.6). The trained classifier based model is used for the prediction of the quality. Whenever a new knuckleprint image is given to the algorithm, all quality parameters are normalized to the range (0,1) and are passed to the trained *SVM* classifier. The *SVM* classifier provides the quality class corresponding to the knuckleprint image. In Fig. 5.14 some *top*, *middle* and *bottom* quality images with respect to each proposed quality parameters are shown.

5.3 Knuckleprint Image Preprocessing

The extracted region of interest (*ROI*) of knuckleprint is generally of poor contrast. Hence image enhancement algorithm as discussed in Section 4.3.1 is applied over the *ROI*. The enhanced knuckleprint image possesses better quality texture. It is shown in Fig. 5.15.

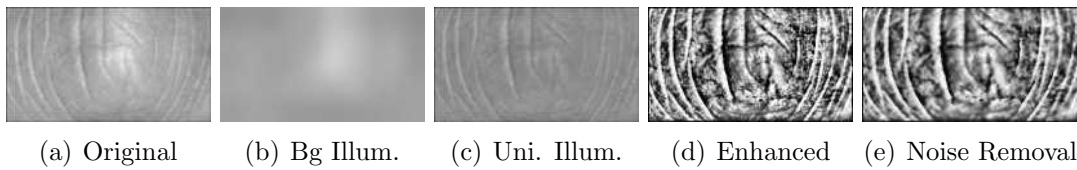


Figure 5.15: Enhanced Knuckleprint

In order to obtain robust representations (*vcode* and *hcode*) that can tolerate small amount of illumination variation, images are transformed using the proposed *LGBP* transformation as discussed in Section 4.3.2 and is shown in Fig. 5.16. An original knuckle along with its *vcode* and *hcode* are shown in Fig. 5.16.

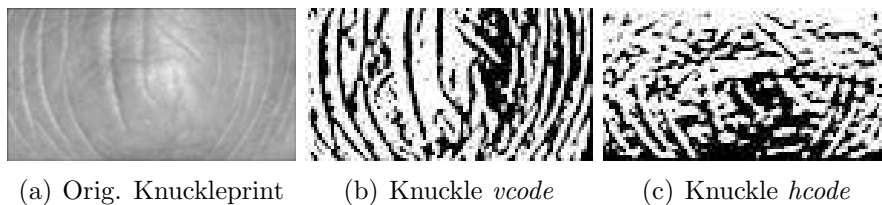


Figure 5.16: Original and Transformed (*vcode*, *hcode*) for Knuckleprint ROI's

In Fig. 5.17, one raw knuckleprint image is considered under varying illumination and is shown along with the corresponding *vcode*. One can observe that the original knuckleprint (as shown in Fig. 5.17(a)) has undergone very severe illumination variation (as shown in Figs. 5.17(b)-5.17(f)). But the corresponding *vcodes* may not be varying much (as shown in Figs. 5.17(g)-5.17(l)). This justifies the use of the proposed transformation and its robustness against varying illumination.

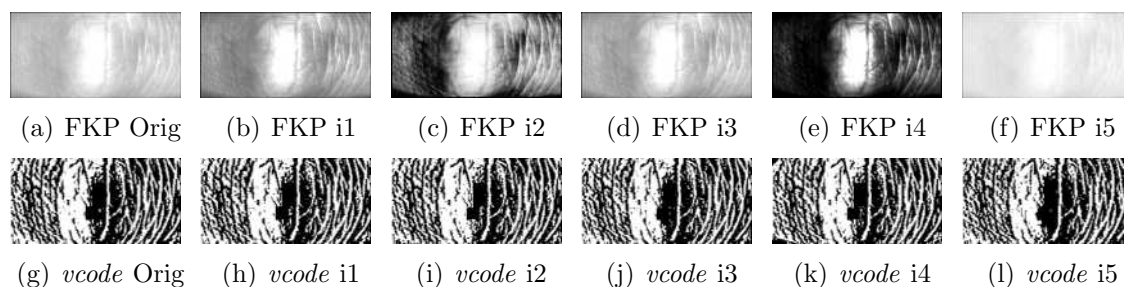


Figure 5.17: Illumination Invariance of *LGBP* transformation. First row shows same image under five different illumination conditions. Second row shows their corresponding *vcode*'s

5.4 Knuckleprint Feature Extraction and Matching

The feature extraction and matching algorithm used in iris based recognition system can be used for knuckleprint as well. The corner based features [63] are extracted from both *vcode* and *hcode* obtained from any knuckleprint *ROI*. The KL tracking [44] has been used to track the corner features in the corresponding images for matching two knuckleprint *ROI*. The proposed *CIOF* dissimilarity measure is used to estimate the performance of KL tracking to differentiate between genuine and imposter matching. The performance of the KL tracking algorithm is good for genuine matching and bad for imposter matchings. All steps applied over any raw knuckleprint image for its recognition are shown in Fig. 5.18.

5.4.1 Corners having Inconsistent Optical Flow (CIOF)

The direction of pixel motion is termed as *optical flow* of that pixel. It can be computed using KL-tracking algorithm. A dissimilarity measure *CIOF* (Corners having Inconsistent Optical Flow) proposed in Section 4.4.1 is used to estimate the KL-tracking performance. Apart from vicinity constraint and patch-wise dissimi-

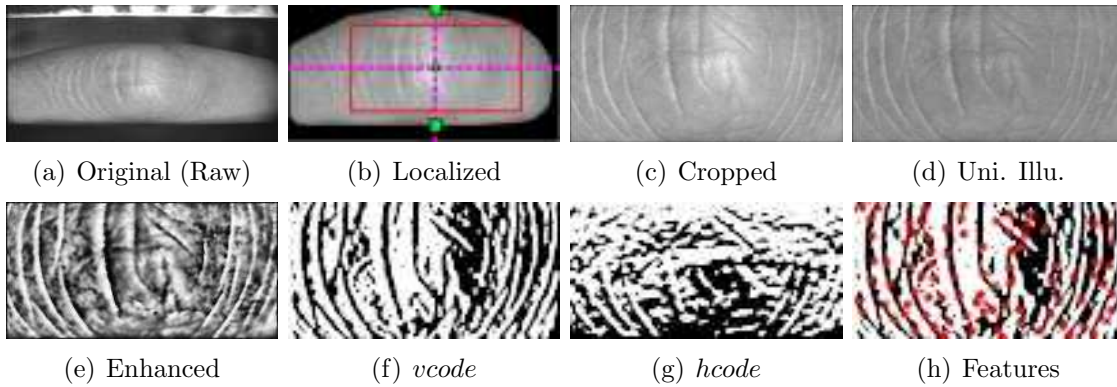


Figure 5.18: Knuckleprint Recognition

larity, one more statistical constraint *viz.* correlation bound is evaluated for each potential matching feature pair given by KL-tracking algorithm defined as follows:

Correlation Bound : The phase only correlation (*POC*) [47] (as defined in Section 3.4) between a local patch centered at any feature and that of its estimated tracked location patch should be at-least equal to an empirically selected threshold T_{cb} . This bound is used to ensure that local patch around each potential matching feature pair is correlated.

Given *vcode* and *hcode* of two images $knuckle_a$ and $knucle_b$, Algorithm 5.3 can be used to compute a dissimilarity score using *CIOF* measure. The *vcode*s are matched to obtain the vertical matching score, while the respective *hcode*s are matched to generate the horizontal matching score. The corner features that are having their tracked position which satisfy the above mentioned three constraints (*viz.* vicinity constraint, patch-wise dissimilarity and correlation bound) are considered as successfully tracked. Consistent global corner optical flow is further used to prune out some of the false matching corners as mentioned in Section 4.4.1. The estimated optical flow angle for each potential matching pair is quantized into eight directions and the most consistent direction is chosen. Any corner matching pair with different optical flow direction is discarded. Finally, the ratio of unsuccessfully

tracked corners to the total number of corner is considered as the dissimilarity measure, $CIOF$. Algorithm 5.3 illustrates all steps. Some of the properties of $CIOF$ distance measure computed between two images A, B are show below :

1. $CIOF(A, B) = CIOF(B, A)$.
2. $CIOF(A, A) = 0$.
3. $CIOF(A, B)$ always lies in the range $[0, 1]$.
4. $CIOF(A, B)$ value will be high if A, B belongs different subjects.

5.5 Database Specifications

The largest publicly available knuckleprint database has been used to analyze the performance of the proposed knuckleprint system. Inter-session matchings are done to perform various experimentation.

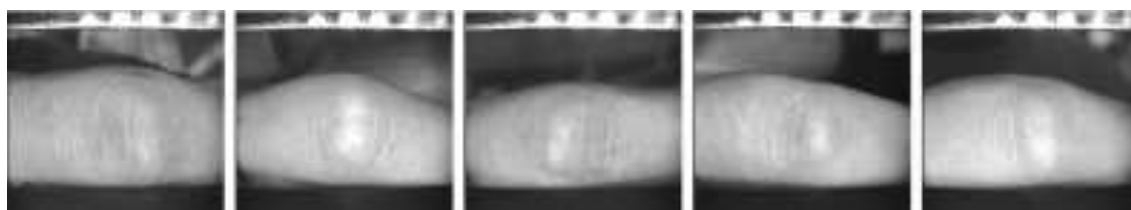


Figure 5.19: Some Images from Knuckleprint Database [56] used in this work

PolyU [56] : It is a huge Knuckleprint database consisting of 7,920 FKP sample images obtained from 165 subjects in two sessions. On an average, time interval between the sessions has been 25 days. In each session, 6 images from 4 fingers (distinct index and middle fingers of both hands) are collected. Hence, a total of $165 \times 4 = 660$ distinct knuckleprints data is collected. Out of 165, 143

Algorithm 5.3 $CIOF(knuckle_a, knuckle_b)$

Require:

- (a) The *vcode* I_A^v, I_B^v of two knuckleprint images $knuckle_a, knuckle_b$ respectively.
- (b) The *hcode* I_A^h, I_B^h of two knuckleprint images $knuckle_a, knuckle_b$ respectively.
- (c) N_a^v, N_b^v, N_a^h and N_b^h are the number of corners in I_A^v, I_B^v, I_A^h and I_B^h respectively.

Ensure: Return $CIOF(knuckle_a, knuckle_b)$.

- 1: Track all the corners of *vcode* I_A^v in *vcode* I_B^v and that of *hcode* I_A^h in *hcode* I_B^h .
 - 2: Obtain the set of corners successfully tracked in *vcode* tracking (*i.e.* stc_{AB}^v) and *hcode* tracking (*i.e.* stc_{AB}^h) that have their tracked position within T_d , their local patch dissimilarity under T_e and also the patch-wise correlation is at-least equal to T_{cb} .
 - 3: Similarly compute successfully tracked corners of *vcode* I_B^v in *vcode* I_A^v (*i.e.* stc_{BA}^v) as well as *hcode* I_B^h in *hcode* I_A^h (*i.e.* stc_{BA}^h).
 - 4: Quantize optical flow direction for each successfully tracked corners into eight directions (*i.e.* at an interval of $\frac{\pi}{8}$) and obtain 4 histograms $H_{AB}^v, H_{AB}^h, H_{BA}^v$ and H_{BA}^h using these four corner sets $stc_{AB}^v, stc_{AB}^h, stc_{BA}^v$ and stc_{BA}^h respectively.
 - 5: For each histogram, out of 8 bins, the bin (*i.e.* direction) which is having the maximum number of corners is considered as the consistent optical flow direction. The maximum value obtained from each histogram is termed as corners having consistent optical flow represented as $cof_{AB}^v, cof_{AB}^h, cof_{BA}^v$ and cof_{BA}^h .
 - 6: $ciof_{AB}^v = 1 - \frac{cof_{AB}^v}{N_a^v}$; [Corners with Inconsis. Optical Flow (*vcode*)]
 - 7: $ciof_{BA}^v = 1 - \frac{cof_{BA}^v}{N_b^v}$; [Corners with Inconsis. Optical Flow (*vcode*)]
 - 8: $ciof_{AB}^h = 1 - \frac{cof_{AB}^h}{N_a^h}$; [Corners with Inconsis. Optical Flow (*hcode*)]
 - 9: $ciof_{BA}^h = 1 - \frac{cof_{BA}^h}{N_b^h}$; [Corners with Inconsis. Optical Flow (*hcode*)]
 - 10: **return** $CIOF(Knuckle_a, Knuckle_b) = \frac{ciof_{AB}^v + ciof_{AB}^h + ciof_{BA}^v + ciof_{BA}^h}{4}$;
-

subjects are belonging to an age group 20 – 30 and others are belonging to 30 – 50 age group.

5.5.1 Testing Strategy

For testing, all 6 images of first session are taken for training while images of second session are taken for testing. Hence, a total of 23,760 genuine and 15,657,840 imposter matchings is considered. The database along with the specifications of testing strategy is given in Table 5.1. One can observe that a large number of

Table 5.1: Database Specifications

Subject	Pose	Total	Training	Testing	Genuine Matching	Imposter Matching
PolyU (Knuckleprint)						
165 (660 Knuckles)	12	7920	First 6	Last 6	23,760	15,657,840

genuine as well as imposter matching is needed to evaluate the performance of the proposed knuckleprint system.

5.6 Performance Analysis

5.6.1 Knuckleprint Segmentation

The PolyU knuckleprint database contains 12 images of 660 subjects each, out of which 7484 images are correctly segmented. Therefore, the proposed segmentation algorithm performs with an accuracy of 94.49% over PolyU [56] knuckleprint database. One can observe that the proposed algorithm can extract the ROI consistently. Some images for which the proposed algorithm fails to segment are shown in Fig. 5.20. The algorithm fails mainly due to poor image quality. Some other reasons for segmentation failure include lack of assumed horizontal knuckle alignment and missing symmetric knuckle texture which is captured using knuckle filter. Also, multiple finger knuckle in an image leads to improper segmentation. Such images are segmented manually.

5.6.2 Threshold Selection

The matching performance of the proposed *CIOF* dissimilarity measure depends on three thresholds *viz.* T_e , T_d and T_{cb} . The values of these parameters are selected

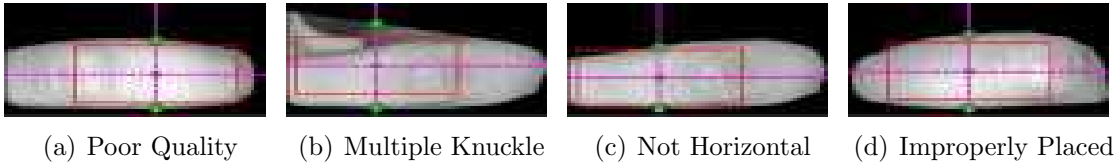


Figure 5.20: Failed Knuckle ROI detection

to maximize the system performance over a validation set containing only left index images of first 50 subjects and using only *vcode* matchings. Several sets of thresholds are considered during testing and the best parametric set in terms of performance is selected and is reported along with few other information in Table 5.2.

Table 5.2: Parameterized Performance Analysis of the proposed system on PolyU Knuckleprint Database. (only *vcode* matching)

PolyU Knuckleprint Database							
T_d	T_e	T_{cb}	DI	EER(%)	Accuracy(%)	EUC	CRR(%)
22	2000	0.17	3.50	1.51	98.83	0.60	99.69
24	2000	0.17	3.51	1.51	98.83	0.60	99.69
22	2000	0.3	3.37	1.31	99.24	0.33	99.79
24	2000	0.3	3.379	1.313	99.24	0.337	99.79
22	2000	0.4	2.56	1.01	99.29	0.376	99.79
22	2200	0.3	3.279	1.11	99.29	0.291	99.79
20	2200	0.3	3.274	1.11	99.24	0.306	99.79
17	2200	0.3	3.268	1.212	99.19	0.384	99.79
31	2600	0.4508	2.183	1.212	99.141	0.381	99.79

The threshold values for which the proposed knuckleprint system is achieved maximum *CRR* and minimum *ERR* are $T_e = 2000$ with patch size of 11×11 with $T_d = 22$ along with $T_{cb} = 0.4$ over PolyU Knuckleprint databases. They are shown in Fig. 5.21 and in Table 5.2. It has bigger patch size along with higher T_d values for knuckleprint images as compared to iris images, because knuckleprint images have long line like coarser features. Also, they are not normalized as in the case of iris.

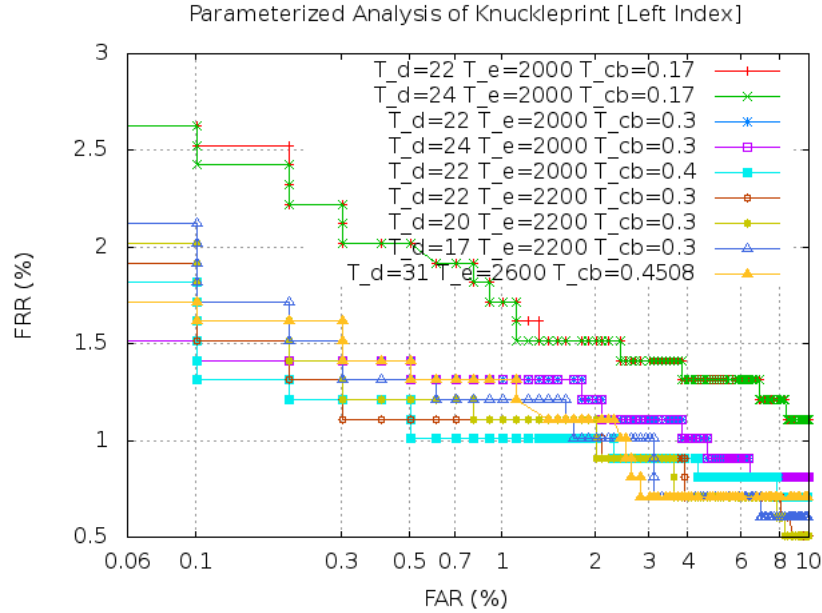


Figure 5.21: Parameterized ROC Analysis of the Proposed System for PolyU Knuckleprint Database. First 50 subject's left index images are used. (only *vcode* matchings)

5.6.3 Comparative Analysis

Table 5.3: Comparative Performance Analysis over PolyU Knuckleprint (Results as reported in [27])

Algorithm	Equal Error Rate
Compcode [35]	1.386
BOCV [1]	1.833
ImCompcode and MagCode [71]	1.210
MoriCode [27]	1.201
MtexCode [27]	1.816
MoriCode and MtexCode [27]	1.0481
<i>vcode</i>	1.5151
<i>hcode</i>	4.2929
<i>vcode</i> + <i>hcode</i>	0.934343

The performance of the proposed system over PolyU knuckleprint database is

compared with some well known systems. It is given in Table 5.3. The EER values as reported in [27] are used for the comparison as they have also adopted the same testing strategy. The ROC curve for performance analysis of the proposed system over PolyU Database is shown in Fig. 5.22. One can observe from Table 5.3 and Fig. 5.22 that the individual $hcode$ performance is not as impressive as $vcode$, but fusion of both ($vcode$ and $hcode$) significantly boost-up the system performance. Such a fusion is very useful because some images may have more discrimination in vertical direction while others have it in horizontal direction. Also, it is observed that the lowest EER is achieved with the proposed fusion which is much better than fusion of $MoriCode$ and $MtexCode$ [27].

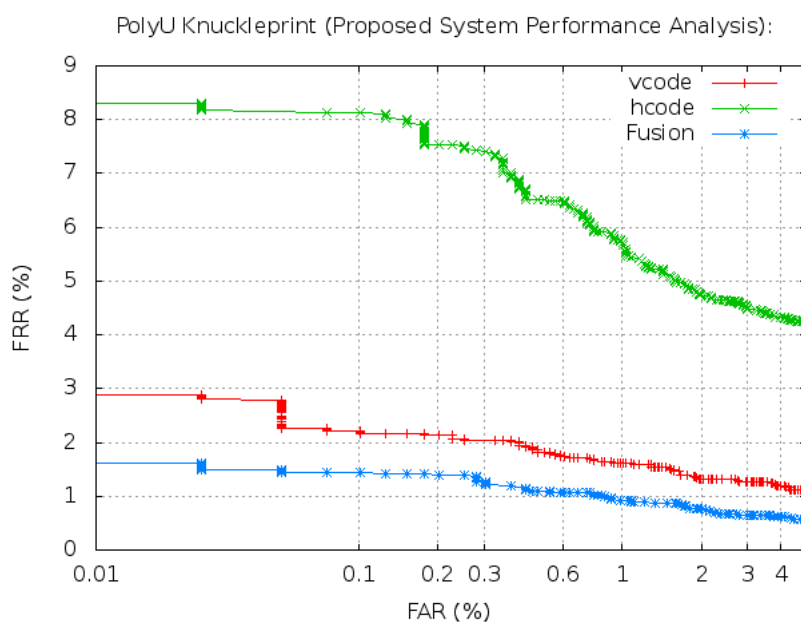


Figure 5.22: Performance of the Proposed System over Knuckleprint PolyU Database

Chapter 6

Palmprint Recognition System

This chapter deals with the problem of designing an efficient palmprint based recognition system. The palmprint ROI is extracted using key-point segmentation algorithm proposed in [9]. Features like palm principle lines, wrinkles and ridges are used for matching between two palmprints. Like any other biometric system, palmprint based recognition system consists of five major tasks, *viz.* ROI extraction, quality estimation, ROI preprocessing, feature extraction and matching. The overall architecture of the proposed system is shown in Fig. 6.1. Two publicly available palmprint databases CASIA [15] and PolyU [57], are used to analyse the performance of the proposed system.

6.1 Palmprint ROI Extraction

The algorithm proposed in [9] for palmprint *ROI* extraction has been used. The hand images are thresholded to obtain the binarized image and the hand contour is extracted. Four key-points (X_1, X_2, V_1, V_2) in the hand contour are computed as shown in Fig. 6.2(b) where X_1, X_2 and V_1, V_2 are left and right-most hill and valley points respectively. Two more key-points, C_1 and C_2 where C_1 is the intersection

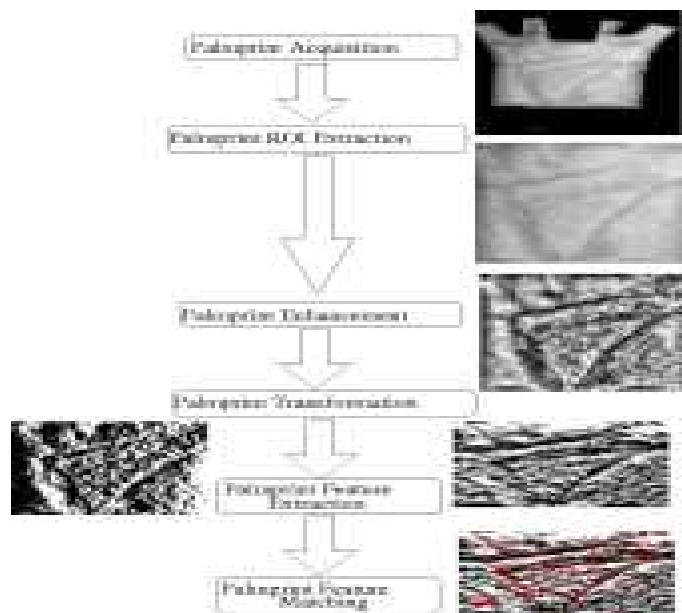


Figure 6.1: Overall Architecture of the Proposed Palmprint Recognition System

point of hand contour and the line passing from V_1 with a slope of 45° and C_2 is the intersection point of hand countour and the line passing from V_2 with a slope of 60° as shown in Fig. 6.2(c). Finally, the midpoints of the line segment V_1C_1 and V_2C_2 are joined which is considered as one side of the square ROI. The final extracted palmprint ROI is shown in Fig. 6.2(d). The various steps involved in ROI extraction are shown in Fig. 6.2. Algorithm 6.1 can be used to extract the ROI from any palmprint image.

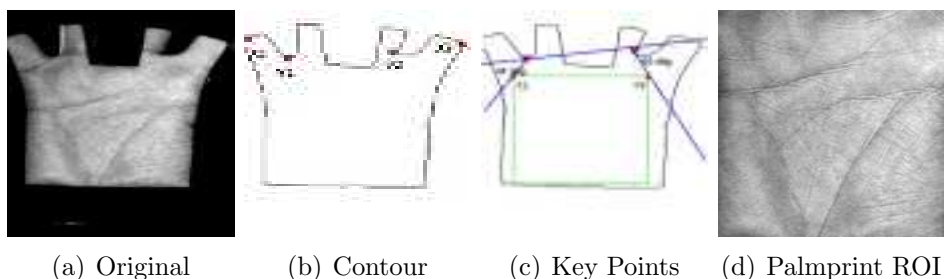


Figure 6.2: Palmprint ROI Extraction (Images are taken from [9])

Algorithm 6.1 Palmprint ROI Extraction**Require:**

Full acquired palmprint image I of dimension $m \times n$ as shown in Fig. 6.2(a).

Ensure:

The cropped palmprint ROI as shown in Fig. 6.2(d).

- 1: Threshold the palmprint image I_p to extract the hand contour C .
- 2: Over the hand contour C find the coordinates of four key points X_1, X_2, V_1, V_2 as shown in Fig.6.2(b).
- 3: Compute C_1 as the intersection point of hand contour and line passing from V_1 with a slope of 45° .
- 4: Compute C_2 as the intersection point of hand contour and line passing from V_2 with a slope of 60° .
- 5: Midpoints of the line segments V_1C_1 and V_2C_2 are considered as one side of the required square palmprint ROI.
- 6: Extract the required square palmprint ROI as shown in Fig. 6.2(d).

6.2 Palmprint Preprocessing

The extracted region of interest (ROI) of palmprint is generally of poor contrast. The image enhancement algorithm discussed in Section 4.3.1 is applied over the ROI . The enhanced palmprint has better quality texture as shown in Fig. 6.3. It uses local block average as the background illumination which is subtracted from the original ROI to obtain uniformly illuminated ROI which is shown in Fig. 6.3(c). Finally image is enhanced using *CLAHE* [55] and noise is removed using weiner filtering [68]. The enhanced palmprint ROI is shown in Fig. 6.3(e).

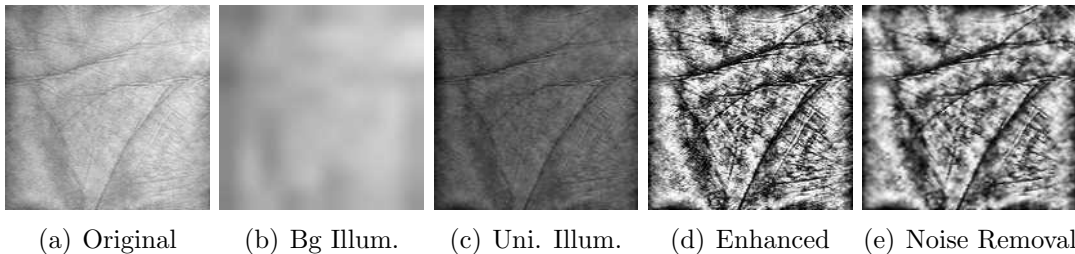


Figure 6.3: Palmprint Image Enhancement

In order to obtain robust representation ($vcode$ and $hcode$) that can tolerate

small amount of illumination variation, images are transformed using the *LGBP* transformation . An original palm along with its *vcode* and *hcode* is shown in Fig. 6.4. It uses the sign of local gradient (vertical and horizontal) around any pixel to obtain a 8 bit *lgbp_code*. This is robust to small illumination variation.

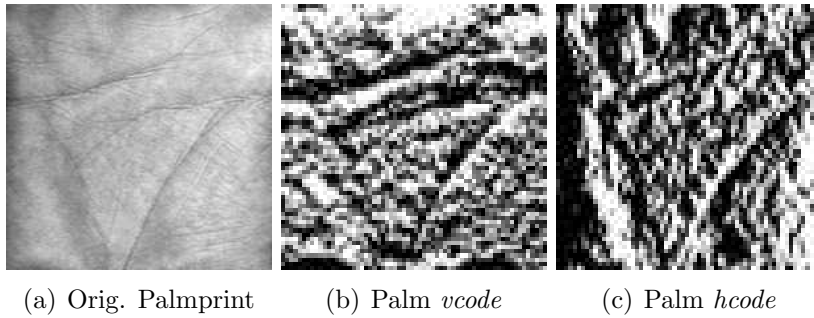


Figure 6.4: Original and Transformed (*vcode*, *hcode*) for Palmprint ROI

6.3 Palmprint Feature Extraction and Matching

The feature extraction and matching algorithm used for knuckleprint in Section 5.4 is also used for palmprint. Both of them possess similar type of features. In order to match two palmprint *ROIs*, corner features [63] are extracted from both *vcode* and *hcode* and are tracked using KL tracking [44] algorithm in the corresponding images. The performance of the KL tracking algorithm is assumed to be good for genuine matching and bad for imposter matching. Hence, a dissimilarity measure, Corners having Inconsistent Optical Flow *CIOF*, can be used to estimate the performance of KL tracking which can differentiate between genuine and imposter matching. Steps that are applied over any raw palmprint image for its recognition are shown in Fig. 6.5.

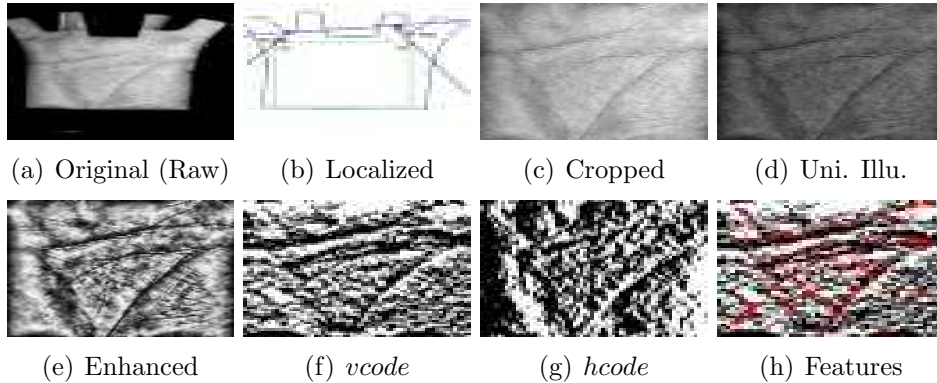


Figure 6.5: Steps of the Palmprint Recognition System

6.3.1 Corners having Inconsistent Optical Flow (CIOF)

All corners are tracked using KL-tracking. The direction in which any corner has moved is termed as its *optical flow* direction. A dissimilarity measure *CIOF* (Corners having Inconsistent Optical Flow) has been proposed to estimate the KL-tracking performance. The *CIOF* measure is defined using three constraints *viz.* vicinity, patch-wise dissimilarity and correlation bound defined as :

[a] **Vicinity Constraints:** Euclidean distance between any corner and its estimated tracked location should not be more than an empirically selected threshold T_d . The parameter T_d depends upon the amount of translation and rotation in the sample images. High T_d signifies more translation and vice-versa.

[b] **Patch-wise Dissimilarity:** Tracking error defined as pixel-wise sum of absolute difference between a local patch centered at current corner and that of its estimated tracked location patch. This error should not be more than an empirically selected threshold T_e . The parameter T_e ensures that the matching corners must have similar neighborhood patch around it.

[c] **Correlation Bound :** The phase only correlation (*POC*) [47] between a local patch centered at any feature and that of its estimated tracked location patch should be at-least equal to an empirically selected threshold T_{cb} . This bound is used

to ensure that local patch around each potential matching feature pair is correlated.

Given $vcode$ and $hcode$ of $palm_a$ and $palm_b$, Algorithm 6.2 is used to compute a dissimilarity score using $CIOF$ measure. The $vcode$ s are matched to obtain the vertical matching score, while the respective $hcode$ s are matched to generate the horizontal matching score. The corners having their tracked position satisfying the above mentioned three constraints (*viz.* vicinity constraint, patch-wise dissimilarity and correlation bound) are considered as successfully tracked. Consistent global corner optical flow is further used to prune out some of the false matching corners as discussed in Section 4.4.1. The estimated optical flow direction (*i.e.* angle in *degrees*) for each potential matching pair is quantized into eight directions and the most consistent direction is chosen. Any corner matching pair with different optical flow direction is discarded. Finally, the ratio of unsuccessfully tracked corners to the total number of corners is considered as the dissimilarity measure between two palmprints.

6.4 Database

The proposed system has been tested on two publicly available databases, *viz.* CASIA [15] and PolyU [57]. All possible inter-session matchings are performed to analyze the system.

CASIA [15] : The CASIA palmprint database has 5502 palmprints taken from 312 subjects (*i.e.* 312 left and right palms is 624 distinct palms). From each subject around 8 images are collected from both hands. The acquisition device uses CMOS based sensor and is pegs free; hence anyone can place his hand easily. However, there are a few subjects who have less than 8 images and they are discarded from the experiment.

PolyU [57] : The PolyU palmprint database has 7752 palmprints of 193

Algorithm 6.2 $CIOF(palm_a, palm_b)$ **Require:**

- (a) The *vcode* I_A^v, I_B^v of two palmprint images $palm_a, palm_b$ respectively.
- (b) The *hcode* I_A^h, I_B^h of two palmprint images $palm_a, palm_b$ respectively.
- (c) N_a^v, N_b^v, N_a^h and N_b^h are the number of corners in I_A^v, I_B^v, I_A^h and I_B^h respectively.

Ensure: Return $CIOF(palm_a, palm_b)$.

- 1: Track all the corners of *vcode* I_A^v in *vcode* I_B^v and that of *hcode* I_A^h in *hcode* I_B^h .
- 2: Obtain the set of corners successfully tracked in *vcode* tracking (*i.e.* stc_{AB}^v) and *hcode* tracking (*i.e.* stc_{AB}^h) that have their tracked position within T_d , their local patch dissimilarity under T_e and also the patch-wise correlation is at-least equal to T_{cb} .
- 3: Similarly compute successfully tracked corners of *vcode* I_B^v in *vcode* I_A^v (*i.e.* stc_{BA}^v) as well as *hcode* I_B^h in *hcode* I_A^h (*i.e.* stc_{BA}^h).
- 4: Quantize optical flow direction for each successfully tracked corners into eight directions (*i.e.* at an interval of $\frac{\pi}{8}$) and obtain 4 histograms $H_{AB}^v, H_{AB}^h, H_{BA}^v$ and H_{BA}^h using these four corner sets $stc_{AB}^v, stc_{AB}^h, stc_{BA}^v$ and stc_{BA}^h respectively.
- 5: For each histogram, out of 8 bins, the bin (*i.e.* direction) which is having the maximum number of corners is considered as the consistent optical flow direction. The maximum value obtained from each histogram is termed as corners having consistent optical flow represented as $cof_{AB}^v, cof_{AB}^h, cof_{BA}^v$ and cof_{BA}^h .
- 6: $cof_{AB}^v = 1 - \frac{cof_{AB}^v}{N_a^v}$; [Corners with Inconsis. Optical Flow (*vcode*)]
- 7: $cof_{BA}^v = 1 - \frac{cof_{BA}^v}{N_b^v}$; [Corners with Inconsis. Optical Flow (*vcode*)]
- 8: $cof_{AB}^h = 1 - \frac{cof_{AB}^h}{N_a^h}$; [Corners with Inconsis. Optical Flow (*hcode*)]
- 9: $cof_{BA}^h = 1 - \frac{cof_{BA}^h}{N_b^h}$; [Corners with Inconsis. Optical Flow (*hcode*)]
- 10: **return** $CIOF(palm_a, palm_b) = \frac{cof_{AB}^v + cof_{AB}^h + cof_{BA}^v + cof_{BA}^h}{4}$;

subjects (*i.e.* 192 left and right palms *i.e.* 386 distinct palms). From each subject, 20 images from both hands and in two sessions (10 images per session) are collected. The acquisition device uses CCD based sensor with spatial resolution of 75 dots per inch. But it contains pegs; hence user has to place his hand accordingly.

There are some palms in both CASIA and PolyU databases with incomplete or missing data. These palms are also discarded for this experiment. Some of the sample images taken from both databases are shown in Fig. 6.6 and specifications of each image are given in Table 6.1. Testing is done over the left and the right

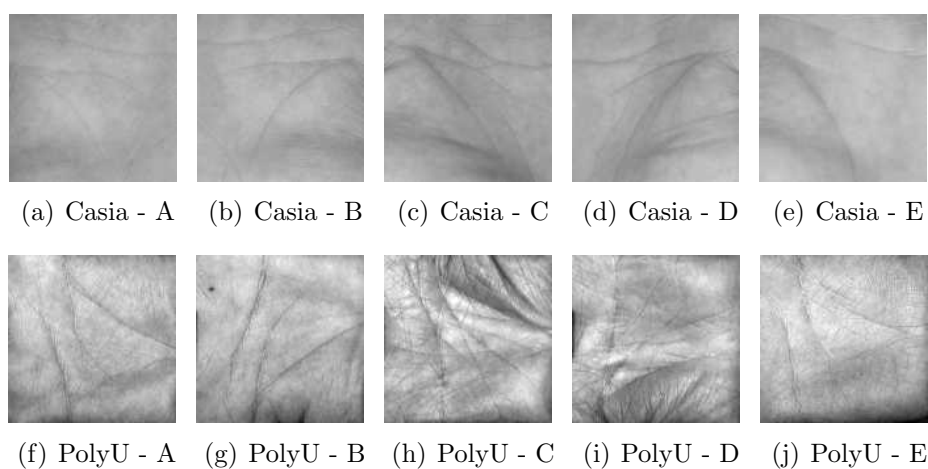


Figure 6.6: Sample Palmprint Images from Casia and PolyU Databases

Table 6.1: Database Specifications

Subject	Pose	Total	Training	Testing	Genuine Matching	Imposter Matching
Casia (Palmprint Left hand)						
290 Palms	8	2,320	First 4	Last 4	4,640	1,340,960
Casia (Palmprint Right hand)						
276 Palms	8	2,208	First 4	Last 4	4,416	1,214,400
Casia (Palmprint Left + Right hand)						
566 Palms	8	4,528	First 4	Last 4	9,056	5,116,640
PolyU (Palmprint Left hand)						
193 Palms	20	3,860	First 10	Last 10	19,300	3,705,600
PolyU (Palmprint Right hand)						
193 Palms	20	3,860	First 10	Last 10	19,300	3,705,600
PolyU (Palmprint Left + Right hand)						
386 Palms	20	7,720	First 10	Last 10	38,600	14,861,000

palm images of both databases to analyse the hand-wise system performance.

6.4.1 Testing Strategy

All intersession matchings are done for performance analysis. Four images of CASIA [15] palmprint database are taken for training while rest of them are kept for testing. Hence, there are 9,056 genuine and 5,116,640 imposter matchings. For PolyU [57] palmprint database, ten images are used for training while rest are taken for testing. Hence, a total of 38,600 genuine and 14,861,000 imposter matchings are performed. The database along with specifications of the testing strategy is given in Table 6.1. One can observe that a large number of genuine as well as imposter matchings are considered to evaluate the performance of the proposed system.

6.5 Performance Analysis

The palmprint ROIs are extracted using the algorithm proposed in [9]. It is observed that the segmentation accuracy depends upon the key point extraction. In both databases, we have seen in several images. It may fail to get key points automatically. Hence, for those images key points are marked manually and segmentation is done. The threshold values for which the proposed palmprint system performs with maximum CRR and minimum ERR are $T_e = 750$ with patch size of 5×5 with $T_d = 18$ along with $T_{cb} = 0.4$ for CASIA and PolyU palmprint databases. The graphs shown in Fig. 6.7 and Fig. 6.8 show the performance achieved by fusing $vcode$ and $hcode$ information as compared with only $vcode$ matchings, for both palmprint databases.

CASIA Database : In Fig. 6.7, the ROC characteristics for all different categories (*i.e* Left, Right and All) of CASIA palmprint database are shown. Table 6.1 shows the total number of genuine as well as imposter matchings. One can see that the proposed system has performed equally well over all three categories of CASIA databases and has shown huge performance boost-up after fusion of $vcode$

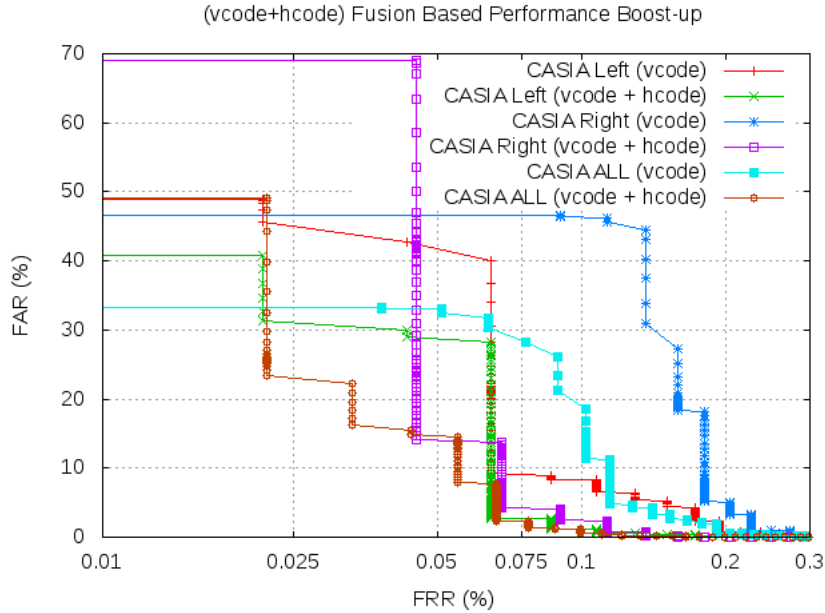


Figure 6.7: Vertical and Horizontal Information Fusion based Performance Boost-up for CASIA Palmprint Databases (X – axis in Log scale)

and $hcode$. It has achieved EER of 0.2006, 0.1537 and 0.1551 with CRR of 100% over Left, Right and All CASIA palmprint databases as shown in Table 6.2.

	Hand Information	d'	CRR	EER
PALM (CASIA)	LEFT HAND	2.55	100	0.2006
PALM (CASIA)	RIGHT HAND	2.59	100	0.1537
PALM (CASIA)	FULL DB (LEFT + RIGHT)	2.43	100	0.1551
PALM (POLYU)	LEFT HAND	2.38	99.89	0.5699
PALM (POLYU)	RIGHT HAND	2.56	100	0.2072
PALM (POLYU)	FULL DB (LEFT + RIGHT)	2.46	99.95	0.4145

Table 6.2: Palmprint Results ($L=LEFT$ Hand, $R=RIGHT$ Hand, $ALL=L + R$)

PolyU Database : In Fig. 6.8 the ROC characteristics for various PolyU palmprint databases are shown. One can infer that overall system's performance with respect to EER is very good but as compared with CASIA database it is poor. This is because our ROI cropping algorithm fails to segment accurately for

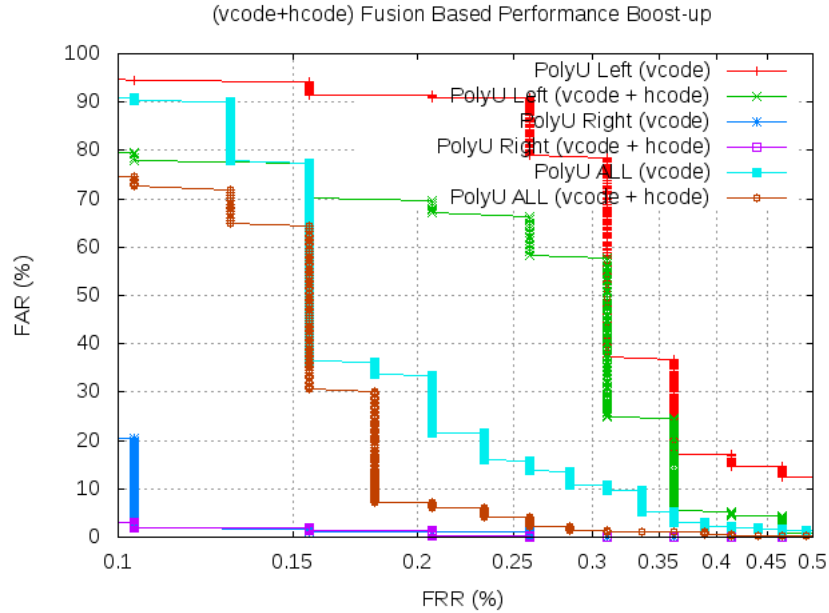


Figure 6.8: Vertical and Horizontal Information Fusion based Performance Boost-up for PolyU Palmprint Databases (X – axis in Log scale)

some subjects. Also the PolyU database is subject-wise much bigger than CASIA database. Hence huge number of imposter and genuine matching are performed for PolyU (as shown in Table 6.1) database. An EER of 0.5699, 0.2072 and 0.4145 with CRR more than 99.89% has been achieved over Left, Right and All PolyU palmprint databases as shown in Table 6.2. Huge performance boost-up after fusion has been observed.

Performance of the system when it is used the right palm is observed to be better. This is mainly because of the fact that most of the subjects are right handers and hence they are comfortable to provide their right hand data. The generalized experimental analysis reveals that $vcode$ is more discriminative than $hcode$ mainly because palms have mostly vertical edges. But for the matchings where $vcode$ fails to discriminate, $hcode$ information has been used to enhance the system performance as it can reduce the falsely accepted imposters. For both databases,

Approach	Database	CRR %	EER %
PalmCode [76]	Palm (CASIA)	99.62	3.67
PalmCode [76]	Palm (PolyU)	99.92	0.53
CompCode [35]	Palm (CASIA)	99.72	2.01
CompCode [35]	Palm (PolyU)	99.96	0.31
OrdinalCode [65]	Palm (CASIA)	99.84	1.75
OrdinalCode [65]	Palm (PolyU)	100.00	0.08
Palm-Zernike [7]	Palm (CASIA)	99.75	2.00
Palm-Zernike [7]	Palm (PolyU)	100.00	0.2939
Proposed	Palm (CASIA)	100.00	0.1551
Proposed	Palm (PolyU)	99.95	0.4145

Table 6.3: Comparative Performance with Other Systems

one can observe a significant performance boost-up by fusing *vcode* and *hcode* scores. The analysis suggests that fusion can effectively reduce false acceptance rate and hence significantly enhance the system performance.

The proposed palmprint recognition system is compared with some well known systems like [7],[35],[65],[76]. It can be seen that the *EER* of the fusion of the proposed (*vcode* and *hcode*) over CASIA palmprint database is 0.1551 which is better than all of these systems. But for PolyU database, the performance of *Ordinal code* [65] is found to be better than all other systems. This performance is due to the huge number of genuine/imposter matchings as shown in Table 6.1. Also, some PolyU images are cropped inaccurately due to translation and illumination variation. Hence, the overall performance of the proposed system is found to be better or comparable with the most of known systems.

Chapter 7

Multimodal Based Recognition System

In this chapter, details of multi-modal based recognition system have been discussed. The major focus is over the creation of multimodal database and its experimental results. Several multimodal systems are *viz.* iris and knuckleprint, knuckleprint and palmprint and finally iris, knuckleprint and palmprint have been proposed. Testing strategies such as intersession matching, one training and one testing and multiple training and multiple testing are adopted. Two publicly available iris databases (CASIA Interval [15] and LAMP [14]) are fused with two public palmprint databases (CASIA [15], PolyU [57]) while for knuckleprint, the publicly available PolyU [57] database is used.

Threshold Selection : In all the proposed multimodal systems the iris, knuckleprint and palmprint matchings are performed using the proposed *CIOF* dissimilarity measure as proposed previously. The threshold values (such as T_d , T_e , T_{cb}) used for each database are obtained by optimizing the proposed system over a validation set (that considers only first few subjects) of that database in terms of performance as explained in Chapters 4, 5, 6.

7.1 Knuckleprint and Palmprint Fusion

In this section, knuckleprint and palmprint images are considered for authentication by fusing them at score level. The proposed system is tested over various combination of two publicly available benchmark palmprint databases CASIA [15] and PolyU [57] along with the largest publicly available PolyU knuckleprint database [75]. The CASIA palmprint database has 5502 palmprint images taken from 312 subjects (*i.e* 624 distinct palms). Eight, images are collected from both hands of each subject. The PolyU palmprint database has 7752 palmprint images of 193 subjects (*i.e* 386 distinct palms). From each subject, 20 images are collected from both hand in two sessions (10 images per session). The PolyU knuckleprint database consists of 7920 knuckleprint images taken from 165 subjects. Each subject has given 6 knuckleprint images of left index (LI), left middle (LM), right index (RI) and right middle (RM) finger in two sessions (*i.e* 660 distinct knuckles). There are some palms in both CASIA and PolyU databases with incomplete or missing data. Such palms are discarded for this experiment. Some of the sample images taken from each database are shown in Fig. 7.1 and detailed database specifications are given in Table 7.1.

7.1.1 Multi-modal Databases Creation

Eight multi-modal databases (*viz.* $A1$ to $A8$) consisting of palm and knuckleprint images are constructed as defined below. Specifications of these databases are given in Table 7.1. In $A1$ and $A2$, only two modalities are fused while in $A4$, $A5$, $A7$, $A8$ three modalities are considered for fusion. In $A3$ and $A6$, six modalities are fused to analyze the performance boost-up.

Databases - $A1$ and $A2$: The $A1$ dataset is created by considering 566 palm subjects from CASIA databases along with first 566 knuckle subjects (out of 660)

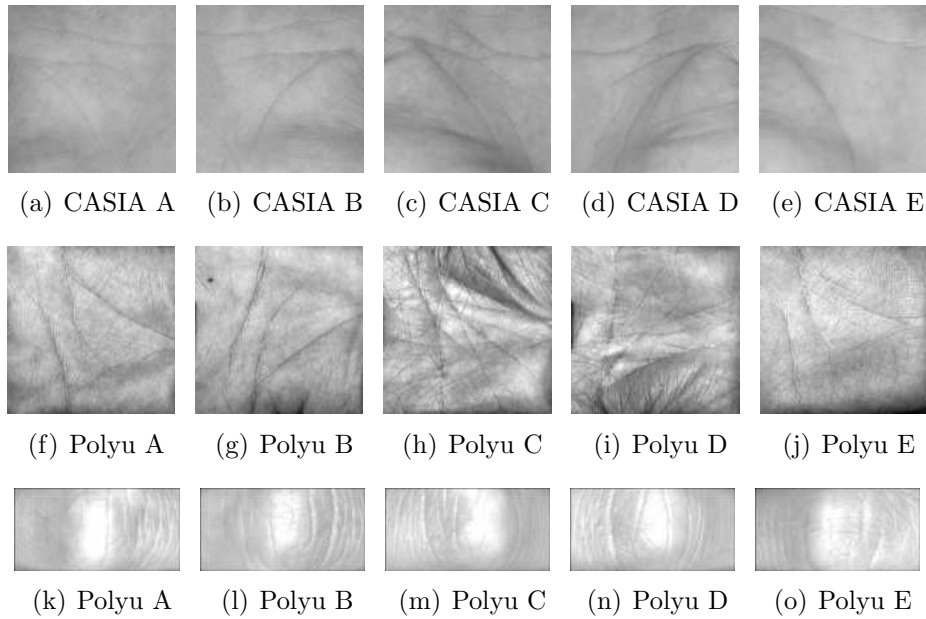


Figure 7.1: Sample Images from all Databases (Five Distinct Users)

from PolyU knuckleprint database. The CASIA palmprint database consists of 8 images per subject while knuckleprint database consists of 12 images per subject; hence to make *A1* database consistent, first and last 4 images per subject are considered to ensure inter-session matching. Therefore *A1* dataset has 4528 palm and knuckle-print images collected from 566 distinct palm and knuckle, with 8 palm as well as knuckle images per subject. The first 4 images per trait of every subject are considered as training images and last 4 images are considered as testing images.

In the similar way, *A2* dataset has been constructed by considering all 386 palms from PolyU palm databases and only first 386 (out of 660) knuckles from PolyU knuckle database. The PolyU palmprint database consists of 20 images per subject while knuckleprint database consists of 12 images per subject; to make *A2* database consistent, first and last 6 images per subject are considered to ensure inter-session matching. First 6 images per trait for every subject are considered as training images and last 6 images are considered as testing images.

Databases - A3 and A6 : The databases $A3$ and $A6$ are constructed by considering all 6 distinct traits per person *viz.* left and right palm (LP, RP) along with left index, left middle, right index and right middle (LI, LM, RI, RM) knuckleprint images, where palmprint images are taken from CASIA and PolyU palmprint databases. All four distinct knuckleprints collected from 165 subjects of knuckleprint database along with only first 165 subject from CASIA and PolyU palm databases are used to obtain $A3$ and $A6$ respectively. First and last 4 images are considered as training and testing images respectively for $A3$ database while for $A6$ database, first and last 6 images are used for training and for testing images respectively.

Databases - A4 and A7 : These databases are constructed by considering 3 distinct traits per subject *viz.* left and right palm (LP, RP) from CASIA and PolyU palmprint databases along with the knuckleprints of first 276 and 193 subjects (out of 660) respectively. First and last 4 images are considered as training and testing images respectively for $A4$ database. For $A7$ database, first and last 6 images are used for training and testing images respectively.

Databases - A5 and A8 : These databases also consider 3 distinct traits that includes all 330 knuckles from left and right hand along with the palmprint data of first 330 palms from CASIA and PolyU palmprint databases respectively. First and last 4 images are considered as training and testing images respectively for $A5$ database while for $A8$ database, first and last 6 images are used for training and testing images.

7.1.2 Testing Strategy

The proposed fusion strategy is used over the databases $A1 - A8$ inter session matchings which is defined as follows. For each database, only inter session matchings are performed to ensure that the two images participating in any matching are temporally distant. The detailed testing specifications for all databases are given in

		Traits / Fusion Specifications	Sub	Pos	Total
Dataset		UNIMODAL			
		PALM (CASIA)	290	8	2320
		PALM (CASIA)	276	8	2208
		PALM (CASIA)	566	8	4528
		PALM (POLYU)	193	20	3860
		PALM (POLYU)	193	20	3860
		PALM (POLYU)	386	20	7720
		KNUCKLE (POLYU)	330	12	3960
		KNUCKLE (POLYU)	330	12	3960
		KNUCKLE (POLYU)	660	12	7920
Dataset	Traits Fused	MULTIMODAL			
A1	2	ALL.PALM(CASIA), ALL.KNUCKLE(POLYU)	566	8	2×4528 = 9056
A2	2	ALL.PALM(POLYU), ALL.KNUCKLE(POLYU)	386	12	2×4632 = 9264
A3	6	L.PALM(CASIA), R.PALM(CASIA), L.INDEXKNUCKLE(POLYU), L.MIDDLEKNUCKLE(POLYU), R.INDEXKNUCKLE(POLYU), R.MIDDLEKNUCKLE(POLYU)	165	8	6×1320 = 7920
A4	3	L.PALM(CASIA), R.PALM(CASIA), ALL.KNUCKLE(POLYU)	276	8	3×2208 = 6624
A5	3	ALL.PALM(CASIA), L.KUNCKLE(POLYU)[LI+LM], R.KUNCKLE(POLYU)[RI+RM]	330	8	3×2640 = 7920
A6	6	L.PALM(POLYU), R.PALM(POLYU), L.INDEXKNUCKLE(POLYU), L.MIDDLEKNUCKLE(POLYU), R.INDEXKNUCKLE(POLYU), R.MIDDLEKNUCKLE(POLYU)	165	12	6×1980 = 11880
A7	3	L.PALM(POLYU), R.PALM(POLYU), ALL.KNUCKLE(POLYU)	193	12	3×2316 = 6948
A8	3	ALL.PALM(POLYU), L.KNUCKLE(POLYU)[LI+LM], R.KUNCKLE(POLYU)[RI+RM]	330	12	3×3960 = 11880

Table 7.1: Database Specifications (L=*LEFT Hand*,R=*RIGHT*,ALL=*L + R*)

Table 7.2. A matching is termed as genuine matching if both of the constituting images are of the same subject; otherwise, it is termed as an imposter matching.

The number of imposter matchings considered for the performance analysis of the proposed system ranges from half a million to 16 million along with the genuine matchings ranging from 3 to 40 thousand. One can observe that huge number of matchings is considered to compute performance parameters of the system. This testing strategy is considered because most of the state-of-the-art systems of palm-print and knuckleprint uses the same for the performance analysis of their systems.

7.1.3 Performance Analysis

All results obtained for unimodal and multi-modal systems are presented in Table 7.3. It has been found that the proposed multimodal system performs much better than the unimodal systems that clearly justifies the fusion strategy. It is found that *CRR* of the proposed multi-modal system is 100.00% with an *EER* less than 0.01% over all eight multi-modal databases which is much better than their corresponding unimodal systems.

Also, the performance of the proposed system is observed to be better than other proposed state-of-the-art multimodal based biometric systems [64], [58], [81] mainly because they have fused face and iris. Their performance got restricted primarily due to several face trait specific issues and challenges (such as pose, expression, aging, illuminations *e.t.c.*). In this work, palm and knuckleprint are considered for fusion as both of them have huge amount of unique and discriminative texture information to compliment each other. Also, both of them are hand based which reduce the data acquisition time, user cooperation and increases the user acceptance and data quality.

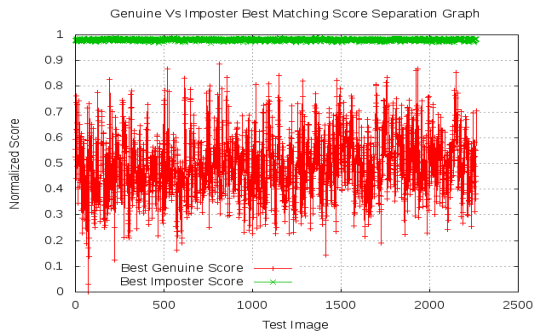
The *EER* of the proposed multi-modal system for all 8 multi-modal databases (*A1* to *A8*) is found to be either zero or very low as given in Table 7.3. Hence, all *ROC* curves look very similar to each other. Generally for such highly accurate systems, in order to draw any significant conclusion, decidability index d' and genuine

		Traits / Fusion Specifications	Training Images	Testing Images	Genuine Matches	Imposter Matches
Dataset		UNIMODAL				
PALM (CASIA)		LEFT HAND	290×4 = 1160	290×4 = 1160	4640	1340960
PALM (CASIA)		RIGHT HAND	276×4 = 1104	276×4 = 1104	4416	1214400
PALM (CASIA)		FULL DB (LEFT + RIGHT)	566×4 = 2264	566×4 = 2264	9056	5116640
PALM (POLYU)		LEFT HAND	193×10 = 1930	193×10 = 1930	19300	3705600
PALM (POLYU)		RIGHT HAND	193×10 = 1930	193×10 = 1930	19300	3705600
PALM (POLYU)		FULL DB (LEFT + RIGHT)	386×10 = 3860	386×10 = 3860	38600	14861000
KNUCKLE (POLYU)		LEFT HAND	330×6 = 1980	330×6 = 1980	11880	3908520
KNUCKLE (POLYU)		RIGHT HAND	330×6 = 1980	330×6 = 1980	11880	3908520
KNUCKLE (POLYU)		FULL DB (LEFT + RIGHT)	660×6 = 3960	660×6 = 3960	23760	15681600
Dataset	Traits Fused	MULTIMODAL				
A1	2	ALL.PALM(CASIA), ALL.KNUCKLE(POLYU)	566×4 = 2264	566×4 = 2264	9056	5116640
A2	2	ALL.PALM(POLYU), ALL.KNUCKLE(POLYU)	386×6 = 2316	386×6 = 2316	13896	5349960
A3	6	L.PALM(CASIA), R.PALM(CASIA), L.INDEXKNUCKLE(POLYU), L.MIDDLEKNUCKLE(POLYU), R.INDEXKNUCKLE(POLYU), R.MIDDLEKNUCKLE(POLYU)	165×4 = 660	165×4 = 660	2640	432960
A4	3	L.PALM(CASIA), R.PALM(CASIA), ALL.KNUCKLE(POLYU)	276×4 = 1104	276×4 = 1104	4416	1214400
A5	3	ALL.PALM(CASIA), L.KUNCKLE(POLYU)[LI+LM], R.KUNCKLE(POLYU)[RI+RM]	330×4 = 1320	330×4 = 1320	5280	1737120
A6	6	L.PALM(POLYU), R.PALM(POLYU), L.INDEXKNUCKLE(POLYU), L.MIDDLEKNUCKLE(POLYU), R.INDEXKNUCKLE(POLYU), R.MIDDLEKNUCKLE(POLYU)	165×6 = 990	165×6 = 990	5940	974160
A7	3	L.PALM(POLYU), R.PALM(POLYU), ALL.KNUCKLE(POLYU)	193×6 = 1158	193×6 = 1158	6948	1334016
A8	3	ALL.PALM(POLYU), L.KNUCKLE(POLYU)[LI+LM], R.KUNCKLE(POLYU)[RI+RM]	330×6 = 1980	330×6 = 1980	11880	3908520

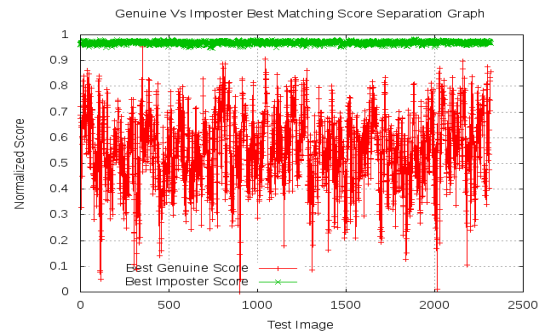
Table 7.2: Testing Strategy Specifications (L=LEFT,R=RIGHT,ALL=L + R)

		Traits / Fusion Specifications	d'	CRR	EER
Dataset		UNIMODAL			
	PALM (CASIA)	LEFT HAND	2.57	99.91	0.30
	PALM (CASIA)	RIGHT HAND	2.53	100	0.34
	PALM (CASIA)	FULL DB (LEFT + RIGHT)	2.30	99.96	0.29
	PALM (POLYU)	LEFT HAND	1.72	99.89	2.09
	PALM (POLYU)	RIGHT HAND	1.79	100	1.34
	PALM (POLYU)	FULL DB (LEFT + RIGHT)	1.71	99.95	1.5
	KNUCKLE (POLYU)	LEFT HAND	2.07	99.40	3.22
	KNUCKLE (POLYU)	RIGHT HAND	2.06	99.55	3.22
	KNUCKLE (POLYU)	FULL DB (LEFT + RIGHT)	2.08	99.41	3.06
Dataset	Traits Fused	MULTIMODAL			
A1	2	ALL.PALM(CASIA), ALL.KNUCKLE(POLYU)	2.78	100	0.02
A2	2	ALL.PALM(POLYU), ALL.KNUCKLE(POLYU)	2.43	100	0.12
A3	6	L.PALM(CASIA), R.PALM(CASIA), L.INDEXKNUCKLE(POLYU), L.MIDDLEKNUCKLE(POLYU), R.INDEXKNUCKLE(POLYU), R.MIDDLEKNUCKLE(POLYU)	4.62	100	0.0
A4	3	L.PALM(CASIA), R.PALM(CASIA), ALL.KNUCKLE(POLYU)	3.90	100	0.0
A5	3	ALL.PALM(CASIA), L.KUNCKLE(POLYU)[LI+LM], R.KUNCKLE(POLYU)[RI+RM]	3.39	100	0.0
A6	6	L.PALM(POLYU), R.PALM(POLYU), L.INDEXKNUCKLE(POLYU), L.MIDDLEKNUCKLE(POLYU), R.INDEXKNUCKLE(POLYU), R.MIDDLEKNUCKLE(POLYU)	2.89	100	0.02
A7	3	L.PALM(POLYU), R.PALM(POLYU), ALL.KNUCKLE(POLYU)	2.95	100	0.0
A8	3	ALL.PALM(POLYU), L.KNUCKLE(POLYU)[LI+LM], R.KUNCKLE(POLYU)[RI+RM]	2.53	100	0.04

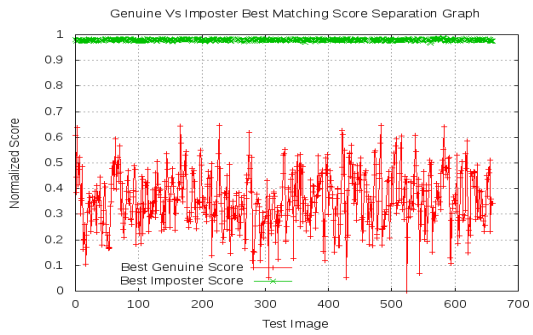
Table 7.3: Consolidated Results (L=*LEFT Hand*,R=*RIGHT Hand*,ALL=*L + R*)



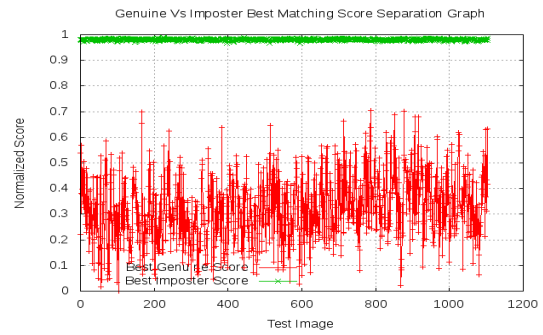
(a) A1



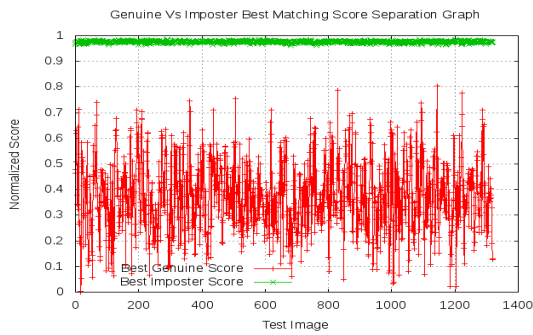
(b) A2



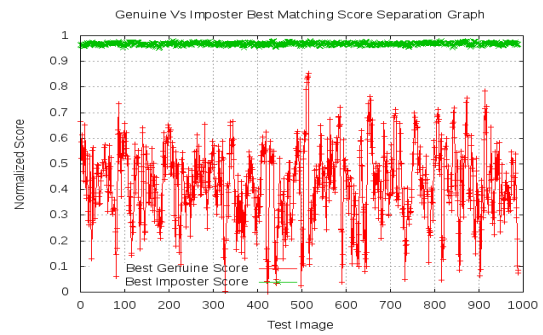
(c) A3



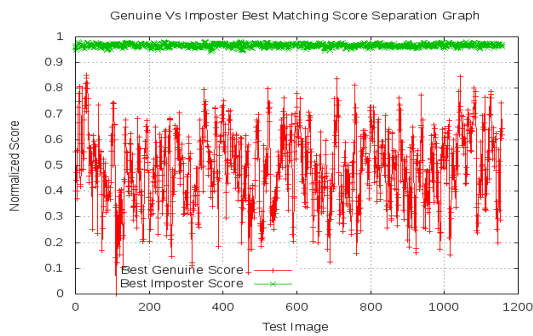
(d) A4



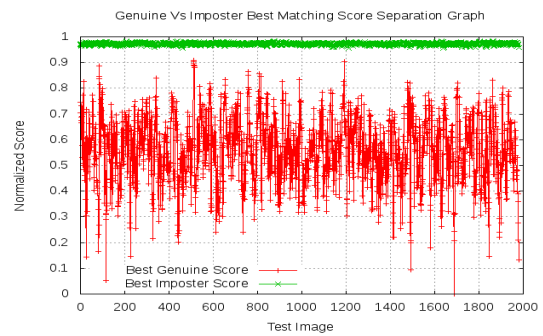
(e) A5



(f) A6



(g) A7



(h) A8

Figure 7.2: Genuine Vs Imposter Best Matching Score Separation Graphs

vs imposter best matching score separation graphs are used.

Decidability Index (d') : The decidability index d' measures the separability of all genuine and imposter matching scores. Higher d' signifies better separation and hence superior performance. From Table 7.3, it is observed that d' value for all multi-modal databases is more than 2.5 and for some databases (databases consisting more than two traits fusion) it is as high as 4.6 which is supposed to be very good.

Genuine vs Imposter Best Match Graph : Genuine vs imposter best matching score separation graph plots the best genuine and the best imposter score for all probe images. From these graphs, the best genuine and the best imposter matching score separation can be analyzed visually. Such graphs for all multi-modal databases (A1 to A8) are shown in Fig. 7.2. It can be observed that only for one or two probe images, the genuine and imposters scores are comparable. For all other multi-modal databases, clear-cut and discriminative separation between genuine and imposter best matchings for all probe images can be seen; hence the overall performance of the proposed system is formed to be very good.

7.2 Iris and Knuckleprint Fusion

In this section iris and knuckleprint images are considered for authentication by fusing them at score level. The proposed system is tested on two publicly available CASIA V4 Interval [14] and Lamp [14] iris databases along with the largest publicly available PolyU [56] knuckleprint database. The CASIA V4 Interval database contains 2,639 iris images collected from 249 subjects having 395 distinct irises with about 7 images per iris. Left and right eye of the same individual are considered as different subjects since iris patterns are formed randomly. Interval iris images are taken in two sessions under indoor environment. The CASIA V4 Lamp is a huge database consisting of 16,212 images collected from 411 subjects having 819 distinct

irises and 20 images per iris. The Lamp iris images are taken in only one session under indoor environment with lamp on/off. Iris images in the Lamp database are more challenging than the Interval database because of nonlinear deformation due to variation of visible illumination. The PolyU Knuckleprint is a database consisting of 7,920 *FKP* images obtained from 165 subjects in two sessions. At each session, 6 images from 4 fingers (distinct index and middle fingers of both hands) are collected. Hence a total of $165 \times 4 = 660$ distinct knuckleprints is collected. Later two chimeric multimodal databases are created for testing. The database specifications are given in Table 7.4. There are very few subjects in CASIA V4 Interval and Lamp iris database which do not have sufficient images for matching (not even a single test image). Such subjects are discarded for this experiment.

7.2.1 Multimodal Database Creation

Two chimeric multimodal databases are created by fusion of the above mentioned iris and knuckleprint databases. The iris samples are totally uncorrelated with knuckleprint samples; both data taken from different subjects are merged and scores are fused. Both of the created multimodal chimeric database contains huge amount of images and hence it is a big challenge to achieve good results over them, because the number of falsely accepted sample rate (*FAR*) grows very fast with the database size [5].

CASIA Interval and PolyU (MM1) : All of the CASIA V4 Interval database images are considered along with the knuckleprint of first 395 subjects from PolyU knuckleprint database. Hence, a total of 2,639 iris images as well as knuckleprints are need to define a multimodal database. This database is named as **MM1**. Specifications of this database are given in Table 7.4.

CASIA Lamp and PolyU (MM2) : All PolyU Knuckleprints along with the first and last 6 images (*i.e* a total of 12 samples) of initial 660 iris samples from

Table 7.4: Database Specifications

Subject	Pose	Total	Training	Testing	Genuine Matching	Imposter Matching
Casia V4 Interval (Iris)						
249 (395 Iris)	7	2,639	First 3	Rest	3,657	1,272,636
Casia V4 Lamp (Iris)						
411 (819 Iris)	20	16,212	First 10	Last 10	78,300	61,230,600
PolyU (Knuckleprint)						
165 (660 Knuckleprint)	12	7920	First 6	Last 6	23,760	15,657,840
Multimodal (Iris Interval + Knuckleprint PolyU) MM1						
395 (Iris Fused Knuckleprint)	7	2,639 Iris and 2,639 Knuckleprint	First 3	Rest	3,657	1,272,636
Multimodal (Iris Lamp + Knuckleprint PolyU) MM2						
660 (Iris Fused Knuckleprint)	12	16,212 Iris and 16,212 Knuckleprint	First 6	Last 6	23,760	15,657,840

CASIA V4 Lamp iris database are considered to define a modified database. A total of 7,920 iris as well as knuckleprint sample images from 660 distinct irises as well as knuckleprints are used in this multi-modal database which is named as **MM2**. Specifications of the database are given in Table 7.4.

7.2.2 Testing Strategy

CASIA V4 Interval database : For testing, images of first session are taken as training while remaining images are considered for testing. Hence, a total of 3,657 genuine and 1,272,636 imposter matchings are considered for Interval database testing.

CASIA V4 Lamp database : For testing, first 10 images are considered as training and rest are taken for testing. Hence, a total of 78,300 genuine and 61,230,600 imposter matchings are used for Lamp database.

PolyU Knuckleprint database : For testing, all 6 images of first session are taken as training while images of second session are taken as testing. It has

considered a total of 23,760 genuine and 15,657,840 imposter matchings for Lamp database.

CASIA V4 Interval fused with PolyU database (MM1): For testing the system in chimeric multimodal database same strategy for Interval testing is used. Iris images of first session are fused with first 3 PolyU knuckleprint images and are considered as training data while remaining iris images of that subject are fused with the same number of PolyU knuckleprint of second session for testing. Hence, a total of 3,657 genuine and 1,272,636 imposter matchings are considered for *MM1* database.

CASIA V4 Lamp fused with PolyU database (MM2): For testing the system in chimeric multimodal database same strategy of PolyU Knuckleprint testing is considered. Knuckleprint of first session are fused with first 6 iris Lamp images and are considered as training data while remaining knuckleprints of that subject are fused with the last 6 iris Lamp images for testing. Hence, it has considered a total of 23,760 genuine and 15,657,840 imposter matchings for testing on *MM2* database.

The database as well as testing specifications are given in Table 7.4. One can observe that a huge amount of imposter as well as genuine matchings are performed for the performance evaluation we have adopted this testing strategy because all state-of-the-art systems [80], [60], [46] have used the same strategy.

7.2.3 Performance Analysis

The proposed multimodal system is rigorously tested over chimerically self created multimodal database *viz.* *MM1* and *MM2* by fusing iris samples with knuckleprint samples. It is found that *CRR* (**Rank 1** accuracy) of the proposed system is 100% over both databases. For both *MM1* and *MM2* databases, Receiver Operating Characteristics (*ROC*) curves are shown in Fig. 7.3. *ROCs* over all five database

viz. CASIA V4 Interval, CASIA V4 Lamp, PolyU Knuckle, *MM1* and *MM2* are plotted for comparative analysis. It is evident that multimodal fusion enhances the system performance significantly. Since this is the first attempt in which iris and knuckleprint samples are fused; hence there does not exist any system which can be compared with. Comparison with some existing multimodal systems like [64], [58], [81], [59], [38], [39], [49], [48], [82], [53], [47] that are fusing, face and iris or knuckle and palm is not justified as their results are restricted due to their selected biometric modalities. Also all the above referred multimodal systems lack of uniformity in the selected modality, database as well as testing strategies. But still the proposed system's performance is much better than all of the above stated state-of-the-art multimodal as well as unimodal systems.

One can clearly see from Fig. 7.3 and Table 7.5 how well the proposed fusion based multimodal system has performed. Any system can be considered generally as a highly secure system if matching error per 1000 matching is less than 1. The verification accuracy is evaluated in terms of *EER* and is found to be 0.027% over *MM1* and 0.083% over *MM2*. It means that the proposed system performs only two and eight errors per ten thousand matching over *MM1* and *MM2* respectively, which can be considered as very good performance. The decidability index (d') is found to be 2.31 and 2.25 for *MM1* and *MM2* databases respectively. One can see that *MM2* is really a big database; hence huge amount of matchings are performed (23,760 genuines against /15,657,840 imposters) as compared with *MM1* (3,657 genuines against /1,272,636 imposters). Also, the iris images of Lamp database are severely affected due to lighting variation, but still after fusion with knuckleprint, the system performance has been tremendously improved as seen in Fig 7.3 and Table 7.5. Apart from the performance, the system has shown its scalability as the performance does not vary much with the increased size of the database. Negligible error under *ROC* curve is obtained for both multimodal databases *viz.* *MM1* (*i.e.*

Description	DI	EER(%)	Accuracy(%)	EUC	CRR(%)
Iris Casia Interval Database					
<i>vcode</i>	2.069	0.1659	99.837	0.0052	100
<i>hcode</i>	1.701	0.6835	99.357	0.0539	99.7538
<i>fusion</i>	2.0182	0.1093	99.910	0.0009	100
Iris Casia Lamp Database					
<i>vcode</i>	1.5799	1.5732	98.615	0.3553	99.7828
<i>hcode</i>	1.3013	3.2207	97.017	0.815	99.7062
<i>fusion</i>	1.5045	1.3005	98.859	0.2407	99.8722
Knuckleprint PolyU Database					
<i>vcode</i>	2.1712	1.5151	98.8636	0.4955	99.6464
<i>hcode</i>	1.6998	4.2929	96.7424	2.8553	97.1464
<i>fusion</i>	2.0374	0.9343	99.2550	0.2566	99.7979
Multimodal (Iris Interval + Knuckleprint PolyU) MM1 Database					
<i>fusion</i>	2.3191	0.0273	99.975	0.0006	100
Multimodal (Iris Lamp + Knuckleprint PolyU) MM2 Database					
<i>fusion</i>	2.2545	0.08330	99.927	0.002	100

Table 7.5: Performance Analysis of the Proposed System over Iris Interval and Lamp Databases along with Knuckleprint PolyU Database (In the above Table fusion referred as vcode+hcode)

6×10^{-4}) and *MM2* (*i.e.* 2×10^{-3}) ensuring the robustness and perfection of the proposed multimodal system.

7.3 Iris, Knuckleprint and Palmprint Fusion

In this section, iris, knuckleprint and palmprint images are considered for authentication by fusing them at score level. The proposed system is tested on two publicly available CASIA V4 Interval [14] and Lamp [14] iris databases, two publicly available CASIA [15] and PolyU [57] palmprint databases along with the largest publicly available PolyU [56] knuckleprint database. The CASIA V4 Interval database contains 2,639 iris images collected from 395 distinct irises while the Lamp database contains 16,212 images collected from 819 distinct irises. The PolyU Knuckleprint

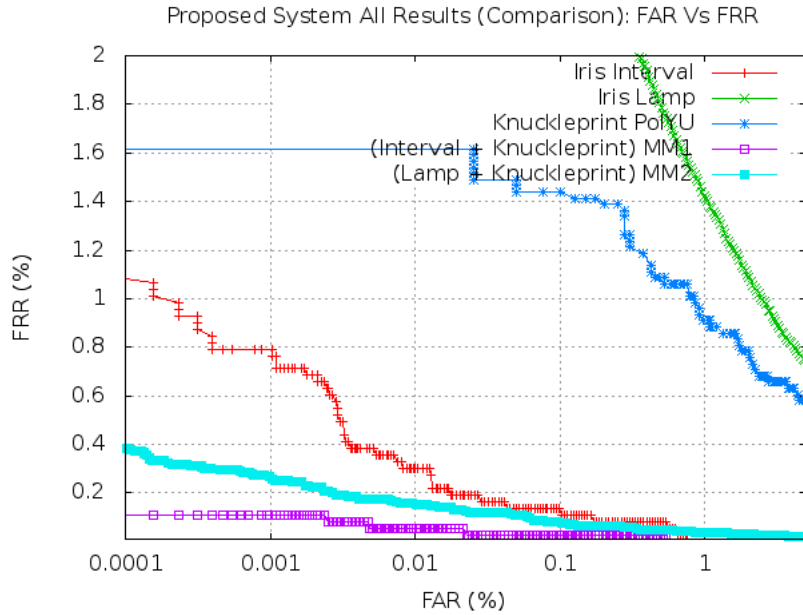


Figure 7.3: ROC Characteristics Comparison of the Unimodal Vs Multimodal Databases for the Proposed System

Database	Iris	Knuckleprint	Palmprint	Subject	Training	Testing	Total Imgs
db1	Interval	PolyU	Casia	349	3	4	2443
db2	Interval	PolyU	PolyU	349	3	4	2443
db3	Lamp	PolyU	Casia	566	4	4	4528
db4	Lamp	PolyU	PolyU	386	6	6	4632

Table 7.6: Database Specifications of Four Self Created Tri-Modal Database using Iris, Knuckleprint and Palmprint.

database consists of 7,920 *FKP* images obtained from 660 distinct knuckleprints. The CASIA palmprint database has 5502 palmprints taken from 624 distinct palms while PolyU palmprint database has 7752 palmprints of 386 distinct palms. Later, four multimodal databases are created for testing. Specifications of the databases are given in Table 7.6.

7.3.1 Multimodal database creation

Two iris databases are fused with two palmprint databases and single knuckleprint database, that means, four different multimodal databases are created *viz.* db1, db2, db3 and db4 which are described in Table 7.6.

db1 : The dataset is constructed by considering all iris images of the interval database belonging to all subjects. These iris samples are fused with first 349 subjects of knuckleprint (PolyU) and palmprint (CASIA) databases. First 3 images are considered for training while first 4 images of second session are used for testing for both knuckleprint and palmprint.

db2 : The dataset is constructed by considering every iris image of all interval subjects. These iris samples are fused with first 349 subjects of knuckleprint (PolyU) and palmprint (PolyU) databases. First 3 images are considered for training while first 4 images of second session are considered as testing images for both knuckleprint and palmprint.

db3 : The dataset is constructed by considering 8 palmprint images taken from all CASIA palmprint subjects. These palmprint of first 566 subjects are fused with knuckleprints (PolyU) and iris (Lamp) databases. First 4 images are considered for training while first 4 images of second session are used for testing for both knuckleprint and iris.

db4 : The dataset is constructed by considering 12 palmprint images taken from all PolyU palmprint subjects. These palmprints are fused with first 386 subjects of knuckleprint (PolyU) and iris (Lamp) databases. For both knuckleprint and iris first 6 images are used for training while first 6 images of second session are considered for testing.

7.3.2 Testing Strategy

In order to test the multimodal system, testing strategy harder than previously used inter-session matching is devised which is described as follows. Any system typically enrolls only one image per subject during the enrollment phase. Hence one training and one testing image per subject (*i.e* 1 – *Training* and 1 – *Testing*) can be a suitable testing strategy for more general system setting. Also 1 – *Training* and multiple testing images per subject are used to analyze the average system behavior. Apart from single image training, multiple training image strategy is also considered. Multiple training images facilitate the identification and hence, affect *CRR* favorably.

On the other hand, multiple image testing scenario is dependent upon the variability in the testing samples. If the database contains less variation and the subsequent testing samples are almost similar to each other than multiple testing images may effect the system performance favorably. But if the testing images are having more texture variation and are different to each other, than performance may be adversely affected.

For every database, the case where only single testing image is used, it always considers the first image of the second session. But while for training, either under single or multiple image strategy, several possible combinations are considered and average result is used. Specifications of the database are given in Table 7.6.

7.3.3 Performance Analysis

The proposed multimodal system is tested over four self created databases. The performance parameters for all three traits individually along with the fusion are given in Table 7.7 -Table 7.10. One training and one testing along with multiple training and testing strategy are considered and four performance parameters *viz.*

FA = Falsely Accepted imposters, FR = Falsely rejected genuine, EER = Equal error rate and CRR = Correct recognition rate are reported.

Biometric Traits \Rightarrow			Iris		Knuckle		Palmprint		Fusion	
Testing Strategy	Total Genuine	Total Imposter	FA	FR	FA	FR	FA	FR	FA	FR
			EER	CRR	EER	CRR	EER	CRR	EER	CRR
1Tr-1Test	349	121452	240	0.66	1849	5	235.33	0.66	0	0
			0.19	99.80	1.47	97.80	0.19	99.90	0	100
1Tr-4Test	1219	424212	476.33	1.33	7300	21	948.66	2.66	0	0
			0.11	99.91	1.72	97.62	0.22	99.83	0	100
2Tr-1Test	698	242904	464	1.33	3670	10.66	464	1.66	0	0
			0.19	100	1.51	99.13	0.19	100	0	100
2Tr-4Test	2438	848424	1033	3	14616	42	1971.33	5.66	0	0
			0.12	100	1.72	99.23	0.23	99.91	0	100
3Tr-1Test	1047	364356	696	2	5568	16	694	2	0	0
			0.19	100	1.72	99.67	0.24	99.91	0	100
3Tr-4Test	3657	1276293	1392	4	21923	63	3007	9	0	0
			0.10	100	1.72	99.67	0.24	99.91	0	100

Table 7.7: Database Specifications for Interval_CASIA (*db1*) containing images from 349 Subjects in $(3+4) = 7$ different poses. First 3 images are considered for training and Last 4 are taken as testing.

One can observe that after fusion, results obtained for all databases under all different testing strategies tend to become almost perfect (*i.e* $CRR = 100\%$ with $EER = 0\%$).

Moreover, one can also observe that with the increase in the number of training and testing images, the genuine and the imposter matchings are increased significantly that affect the performance of any unimodal system but the performance of each fused system remains almost invariant. Hence, one can also infer that the fusion of multiple traits introduces great amount of scalability with respect to system performance. More and more matching can be considered without much performance degradation. This is achieved because many different uncorrelated biometric traits are fused that enhances the uniqueness and the discriminative power of the combined sample and the fused score becomes more and more discriminative.

Biometric Traits \Rightarrow			Iris		Knuckle		Palmprint		Fusion	
Testing Strategy	Total Genuine	Total Imposter	FA	FR	FA	FR	FA	FR	FA	FR
			EER	CRR	EER	CRR	EER	CRR	EER	CRR
1Tr-1Test	349	121452	240	0.66	1849	5	617.66	1.66	0	0
			0.19	99.80	1.47	97.80	0.49	99.33	0	100
1Tr-4Test	1219	424212	476.33	1.33	7300	21	1564.66	4.33	0	0
			0.11	99.91	1.72	97.62	0.36	99.67	0	100
2Tr-1Test	698	242904	464	1.33	3670	10.66	1325	3.66	0	0
			0.19	100	1.51	99.13	0.53	99.52	0	100
2Tr-4Test	2438	848424	1033	3	14616	42	3188.66	9	0	0
			0.12	100	1.72	99.23	0.37	99.86	0	100
3Tr-1Test	1047	364356	696	2	5568	16	2088	6	0	0
			0.19	100	1.72	99.67	0.57	99.71	0	100
3Tr-4Test	3657	1276293	1392	4	21923	63	4872	14	0	0
			0.10	100	1.72	99.67	0.38	99.91	0	100

Table 7.8: Database Specifications for Interval_PolyU (*db2*) containing images from 349 Subjects in $(3+4) = 7$ different poses. First 3 images are considered for training and Last 4 are taken as testing.

Also as discussed in the testing strategy, some interesting observations can be made about the unimodal results.

Iris (Interval) and Palmprint (PolyU) databases : The testing images of both these databases do not possess much variation; as a result, their individual performances are good. Since lesser variation in testing images, the multiple image testing strategy affects favorably as one can observe it from Tables 7.7, 7.8 and 7.10 where results of multiple training and testing image strategy are seen better than their corresponding single image testing scenario.

Iris (Lamp) : Testing images of this database possess much variation because images of the second session are taken under lamp light which makes it difficult for subjects to focus. Also, it is observed that first image (image used for testing) of the second session is of poor quality as it is the first image under lamp illumination and every subject's eye takes some time to adjust to that light. Since more variation in testing images in the multiple image testing strategy affects adversely as one can

Biometric Traits \Rightarrow			Iris		Knuckle		Palmprint		Fusion	
Testing Strategy	Total Genuine	Total Imposter	FA EER	FR CRR	FA EER	FR CRR	FA EER	FR CRR	FA EER	FR CRR
1Tr-1Test	566	319790	4970.33	8.66	6027.66	10.66	385.33	0.66	0	0
			1.54	97.29	1.88	97.17	0.11	99.94	0	100
1Tr-4Test	2264	1279160	16521.33	29.33	24268.66	43	2260	4	0	0
			1.29	97.76	1.8982	97.15	0.17	99.83	0	100
2Tr-1Test	1132	639580	10735.6	19	12338.6	22	753.3	1.33	0	0
			1.67	98.93	1.93	98.70	0.11	100	0	100
2Tr-4Test	4528	2558320	33465.6	59.33	48589	86	4906.3	8.66	0	0
			1.30	99.23	1.89	98.86	0.19	99.94	0	100
3Tr-1Test	1698	959370	14690	26	20118.5	35.5	1130	2	0	0
			1.53	99.38	2.09	98.85	0.11	100	0	100
3Tr-4Test	6792	3837480	51091.5	90.5	74019.5	131	6095	11	0	0
			1.33	99.51	1.92	99.18	0.16	99.97	0	100
4Tr-1Test	2264	1279160	18189	32	27119	48	1130	2	0	0
			1.41	99.64	2.12	99.29	0.08	100	0	100
4Tr-4Test	9056	5116640	66217	117	99902	177	7912	14	0	0
			1.29	99.77	1.95	99.55	0.15	100	0	100

Table 7.9: Database Specifications for Lamp_Casia (*db3*) containing images from 566 Subjects in $(4 + 4) = 8$ different poses. First 4 images are considered for training and Last 4 are taken as testing.

Biometric Traits \Rightarrow			Iris		Knuckle		Palmprint		Fusion	
Testing Strategy	Total Genuine	Total Imposter	FA	FR	FA	FR	FA	FR	FA	FR
			EER	CRR	EER	CRR	EER	CRR	EER	CRR
1Tr-1Test	386	148610	2435	6.33	2181	5.66	1026.6	2.66	0	0
			1.64	97.23	1.46	98.01	0.69	99.13	0	100
1Tr-6Test	2316	891660	11896.6	31	16168.6	42	5647	14.66	0	0
			1.33	97.85	1.81	97.39	0.63	99.4	0	100
2Tr-1Test	772	297220	5135	13.33	4107	10.66	2053.3	5.33	0	0
			1.72	98.87	1.38	99.22	0.69	99.48	0	100
2Tr-6Test	4632	1783320	23873	62	32818	85.33	1293.6	29.33	0.66	0
			1.33	99.32	1.84	98.90	0.63	99.78	0.000019	100
3Tr-1Test	1158	445830	4715.5	12.25	7122.7	18.5	4138.2	10.75	0	0
			1.05	99.64	1.59	99.61	0.92	99.54	0	100
3Tr-6Test	6948	2674980	36720.2	95.5	44253.7	115	22522.2	58.5	103.2	0.5
			1.37	99.08	1.65	99.56	0.84	99.8	0.0055	100
4Tr-1Test	1544	594440	6288.6	16.33	9624	25	5580.3	14.66	0	0
			1.05	99.91	1.61	99.65	0.94	99.74	0	100
4Tr-6Test	9264	3566640	48894	127	58804.3	152.6	30028.3	78	191.33	0.66
			1.37	99.35	1.64	99.78	0.84	99.83	0.00628	100
5Tr-1Test	1930	743050	8661.5	22.5	1551.1	30	6929	18	0	0
			1.16	100	1.55	99.74	0.93	99.74	0	100
5Tr-6Test	11580	4458300	60251	156.5	72765	189	37416	97	374	1
			1.35	99.65	1.63	99.87	0.83	99.91	0.0085	100
6Tr-1Test	2316	891660	10780	28	13090	34	8065	21	0	0
			1.20	100	1.46	99.74	0.9	99.74	0	100
6Tr-6Test	13896	5349960	70833	184	87401	227	43504	113	385	1
			1.32	99.87	1.63	99.87	0.81	99.91	0.0071	100

Table 7.10: Database Specifications for Lamp_PolyU (*db4*) containing images from 386 Subjects in $(6 + 6) = 12$ different poses. First 6 images are considered for training and Last 6 are taken as testing.

observe it from Table 7.10 that the results of multiple training and testing strategy are poorer than their corresponding single testing image scenario.

But some time for very poor quality of some initial test images it is found that the single testing performs slightly poor because with multiple test samples result got averaged out.

Palmprint (CASIA) : Testing images of this databases posses much variation. So, the multiple image testing strategy affect adversely as one can observe it from Tables 7.7, and 7.9 that results of multiple training and testing strategy are poorer than their corresponding single image testing scenario.

Chapter 8

Conclusions

This thesis has presented a multimodal based recognition system by fusing iris, knuckleprint and palmprint biometric traits. Personal authentication is required in several financial and security related applications running in real time and highly accurately. Several state-of-the-art systems use unimodal approach using any one biometric trait such as face, iris, palm, fingerprint, ear, knuckleprint *etc.* But each trait has its own challenges and trait specific issues hence none of them can be considered as the best.

But the performance of any unimodal system has been restricted by varying environmental and non-controlled conditions. Also, it depends upon the sensor precision, reliability and the data quality severely. Apart from them, challenges like pose, expression, age for face or occlusion for iris are some other factors that are responsible for poor performance. Hence, fusion of multiple traits is proposed and is tested. Multimodal systems are highly accurate and harder to be compromised. They are less vulnerable to spoofing and can also deal with missing data. Fusion itself improves the system performance significantly. Hence, tuning of the individual unimodal performance is not required. It is also observed that fusion makes, the system scalable; hence it can handle more and more matchings without much

performance degradation. But this performance boost-up is achieved over the cost of more hardware and time.

Chapter 4 of the thesis has proposed an iris based recognition system. The iris segmentation is done efficiently using an improved circular hough transform for inner iris boundary (*i.e.* pupil) detection. The robust integro-differential operator has been used to detect outer iris boundary that makes use of pupil location. The iris segmentation accuracy is found to be 94.5% and 94.63% for Interval and Lamp database respectively. The erroneous segmentations are categorized in three categories *viz.* occlusion, noise, illumination. A segmentation error hierarchy is created and parametric variations are discussed to segment iris correctly. These parametric adjustment has helped to achieve an accuracy of more than 99.6% for both the databases. The quality of acquired iris sample is estimated using six proposed quality assessment parameters *viz.* Focus (F), Motion Blur (MB), Occlusion (O), Contrast and Illumination (CI), Dilation (D), Specular Reflection (SR). If iris quality is found to be less than a predefined threshold then it is recaptured. This early quality assessment is very crucial to tackle poor quality and non-ideal imagery. The segmented iris is normalized to polar coordinates (*i.e.* rectangular strips). A local image enhancement is also applied to obtain improved iris texture. The enhanced images are preprocessed using the proposed *LGBP* (Local Gradient Binary Pattern) to obtain robust features. The *KLT* based corners features are extracted and matched using the proposed dissimilarity measure *CIOF* (Corners having Inconsistent Optical Flow). The proposed system has been tested over two publicly available CASIA 4.0 Interval and Lamp iris databases consisting of 2,639 and 16,212 images respectively. The parameters are selected in such a way that the performance of the system is maximized over the validation set. The proposed enhancement has shown significant performance improvement in terms of *EER*. It is found that CRR (Rank 1 accuracy) of the proposed system is 100% and 99.87%

for Interval and Lamp databases respectively. Further, its *EER* for Interval and Lamp are 0.109% and 1.3% respectively which is better than several state-of-the-art systems.

Chapter 5 has proposed a knuckleprint based recognition system. The knuckleprint ROI is extracted by applying a modified version of gabor filter to estimate the central knuckle line and point. The central knuckle point is used to extract the knuckleprint ROI from any image consistently. The quality of the acquired knuckleprint sample is estimated using the proposed six quality assessment parameters *viz.* Focus (F), Clutter (C), Uniformity (S), Entropy (E), Reflection (Re), Contrast and Illumination (Con). If the quality is less than a predefined threshold then image is recaptured. The vertical and horizontal knuckle line based features may be of poor quality; hence they are enhanced to obtain better texture. The segmented knuckleprint ROI has been preprocessed using the proposed *LGBP* (Local Gradient Binary Pattern) to obtain robust features. The *KLT* based corners features are extracted and matched using the proposed dissimilarity measure *CIOF* (Corners having Inconsistent Optical Flow). The proposed system has been tested over publicly available PolyU knuckleprint databases consisting of 7,920 images. For testing, 6 images of all first session are taken as training while images of second session are used for testing. Hence total of 23,760 genuine and 15,657,840 imposter matchings are performed. The segmentation algorithm performs with an accuracy of 94.494% over PolyU knuckleprint database and is observed to extract the ROI consistently throughout the database. However, algorithm may fail due to poor image quality, lack of assumed horizontal knuckle alignment, missing symmetric knuckle texture and multiple finger knuckle in an image. Such images are segmented manually. Parameters are selected in such a way that the performance of the system is maximized over the validation set. It is found that *CRR* of the proposed system is 99.79% with an *EER* of 0.93% over PolyU knuckleprint database which is better

than state-of-the-art systems.

Chapter 6 has proposed a palmprint based recognition system. The palmprint segmentation has been done by obtaining the two valley points and by clipping a square shaped ROI using these parts. The palm principle lines, wrinkles and ridges based features are enhanced using the proposed enhancement. The segmented palmprint is preprocessed using the proposed *LGBP* (Local Gradient Binary Pattern) to obtain robust features. The *KLT* based corners features are extracted and matched using the proposed dissimilarity measure *CIOF* (Corners having Inconsistent Optical Flow). The proposed system has been tested over publicly available CASIA and PolyU palmprint databases consisting of 4,528 and 7,720 images respectively. All intersession matchings are done for performance analysis. First 4 images of CASIA palmprint database are taken as training while rest of them are kept for testing. Hence, total of 9,056 genuine and 5,116,640 imposter matchings are performed. For PolyU palmprint database, first 10 images are used for training while rest are taken as testing. Hence a total of 38,600 genuine and 14,861,000 imposter matchings is considered. Parameters are selected in such a way that the performance of the system is maximized over the validation set. It is found that *CRR* (Rank 1 accuracy) of the proposed system is 100% and 99.95% for CASIA and PolyU palmprint databases respectively. Further, its *EER* for CASIA and PolyU are 0.15% and 0.41% respectively which is better than state-of-the-art systems.

Chapter 7 has discussed the multi-modal based recognition system. The major focus is to create multimodal database and its experimental analysis. We have performed different multimodal systems by fusing iris and knuckleprint, knuckleprint and palmprint and iris and finally iris, knuckleprint and palmprint. Different testing strategies have been adopted which include intersession matching, one training and one testing and multiple training and multiple testing. Two publicly available iris databases (CASIA Interval and LAMP) are fused with two public palmprint

databases (CASIA, PolyU) while for knuckleprint, the publicly available PolyU database has been used. Hence, 4 tri-modal databases are generated for testing. It has been observed that the performance of the trimodal system shows almost perfect *ROC* behavioral (*i.e* $CRR = 100\%$ and $EER = 0\%$) for different testing strategies.

References

- [1] Palmprint verification using binary orientation co-occurrence vector. *Pattern Recognition Letters*, 30(13):1219 – 1227, 2009.
- [2] A. Abhyankar, L. Hornak, and S Schuckers. Off-angle iris recognition using bi-orthogonal wavelet network system. In *Fourth IEEE Workshop on Automatic Identification Advanced Technologies*, pages 239–244, 2005.
- [3] A. Abhyankar and S Schuckers. Active shape models for effective iris segmentation. In *Society of Photographic Instrumentation Engineers (SPIE)*, volume 6202, 2006.
- [4] R. Adams and L Bischof. Seeded region growing. *IEEE Transactions on Pattern Analysis and Machine Intelligence*, 16(6):641–647, 1994.
- [5] Sharat Chikkerur Amit J. Mhatre, Srinivas Palla and Venu Govindaraju. Efficient search and retrieval in biometric databases. In *Society of Photographic Instrumentation Engineers (SPIE)*, volume 5779, pages 265–273, 2005.
- [6] G. S. Badrinath and P Gupta. Stockwell transform based palmprint recognition. *Applied Soft Computing*, 11(7):4267–4281, 2011.
- [7] G. S. Badrinath, N K. Kachhi, and P Gupta. Verification system robust to occlusion using low-order zernike moments of palmprint sub-images. *Telecommunication Systems*, 47(3-4):275–290, 2011.

- [8] G. S. Badrinath, Kamlesh Tiwari, and Phalguni Gupta. An efficient palmprint based recognition system using 1d-dct features. In *International Conference on Intelligent Computing (ICIC)*, volume 7389, pages 594–601. LNCS, 2012.
- [9] G.S. Badrinath and Phalguni Gupta. Palmprint based recognition system using phase difference information. *Future Generation Computer Systems*, 28:287–305, 2010.
- [10] D.H Ballard. Generalizing the hough transform to detect arbitrary shapes. *Pattern Recognition*, 13(2):111–122, 1981.
- [11] B. Bonney, R. Ives, D. Etter, and Y Du. Iris pattern extraction using bit planes and standard deviations. In *Thirty-Eighth Asilomar Conference on Signals, Systems and Computers*, volume 1, pages 582–586. IEEE, 2004.
- [12] Kevin W. Bowyer, Karen Hollingsworth, and Patrick J. Flynn. Image understanding for iris biometrics: A survey. *Computer Vision and Image Understanding*, 110(2):281 – 307, 2008.
- [13] T.A. Camus and R Wildes. Reliable and fast eye finding in close-up images. In *16th International Conference on Pattern Recognition*, volume 1, pages 389–394. IEEE, 2002.
- [14] CASIA. The casia iris database. <http://biometrics.idealtest.org/dbDetailForUser.do?id=4>.
- [15] CASIA. The casia palmprint database. <http://biometrics.idealtest.org/dbDetailForUser.do?id=5>.
- [16] Ryan Connaughton, KevinW. Bowyer, and PatrickJ Flynn. Fusion of face and iris biometrics. In Mark J. Burge and Kevin W Bowyer, editors, *Handbook of*

- Iris Recognition*, Advances in Computer Vision and Pattern Recognition, pages 219–237. Springer London, 2013.
- [17] J. Cui, Y. Wang, J.Z. Huang, T. Tan, and Z Sun. An iris image synthesis method based on pca and super-resolution. In *17th International Conference on Pattern Recognition (ICPR)*, volume 4, pages 471–474. IEEE, 2004.
- [18] J Daugman. Statistical richness of visual phase information: update on recognizing persons by iris patterns. *International Journal of Computer Vision*, 45(1):25–38, 2001.
- [19] J.G Daugman. High confidence visual recognition of persons by a test of statistical independence. *IEEE Transactions on Pattern Analysis and Machine Intelligence*, 15(11):1148–1161, 1993.
- [20] John Daugman. How iris recognition works. In *IEEE International Conference on Image Processing (ICIP)*, pages 33–36, 2002.
- [21] John Daugman and Cathryn Downing. Epigenetic randomness, complexity and singularity of human iris patterns. *Royal Society London Biological Sciences*, 268(1477):1737–1740, 2001.
- [22] V. Dorairaj, N.A. Schmid, and G Fahmy. Performance evaluation of non-ideal iris based recognition system implementing global ica encoding. In *IEEE International Conference on Image Processing (ICIP)*, volume 3, pages III–285–5, 2005.
- [23] Nicolae Duta, A K. Jain, and K V. Mardia. Matching of palmprints. *Pattern Recognition Letters*, 23(4):477–485, 2002.

- [24] R.M. Farouk. Iris recognition based on elastic graph matching and gabor wavelets. *Computer Vision and Image Understanding*, 115(8):1239 – 1244, 2011.
- [25] X. Feng, C. Fang, X. Ding, and Y Wu. Iris localization with dual coarse-to-fine strategy. In *18th International Conference on Pattern Recognition (ICPR)*, volume 4, pages 553–556. IEEE, 2006.
- [26] R. Ferzli and L.J Karam. A no-reference objective image sharpness metric based on the notion of just noticeable blur (jnb). *IEEE Transactions on Image Processing*, 18(4):717–728, 2009.
- [27] Guangwei Gao, Jian Yang, Jianjun Qian, and Lin Zhang. Integration of multiple orientation and texture information for finger-knuckle-print verification. *Neurocomputing*, 135:180–191, 2014.
- [28] C C Han, H L Cheng, C L Lin, and K C Fan. Personal authentication using palm-print features. *Pattern Recognition*, 36(2):371–381, 2003.
- [29] X.F. He and P.F Shi. A novel iris segmentation method for hand-held capture device. *Advances in Biometrics*, pages 479–485, 2005.
- [30] Z. He, T. Tan, and Z Sun. Iris localization via pulling and pushing. In *18th International Conference on Pattern Recognition (ICPR)*, volume 4, pages 366–369. IEEE, 2006.
- [31] Y.P. Huang, S.W. Luo, and E.Y Chen. An efficient iris recognition system. In *International Conference on Machine Learning and Cybernetics*, volume 1, pages 450–454. IEEE, 2002.

- [32] A.K. Jain, S. Pankanti, S. Prabhakar, L. Hong, and A. Ross. Biometrics: A grand challenge. In *17th International Conference on Pattern Recognition (ICPR)*, volume 2, pages 935–942. IEEE, 2004.
- [33] P.A. Johnson, B. Tan, and S. Schuckers. Multimodal fusion vulnerability to non-zero effort (spoof) imposters. In *IEEE International Workshop on Information Forensics and Security (WIFS)*, pages 1–5, Dec 2010.
- [34] T. Ko. Multimodal biometric identification for large user population using fingerprint, face and iris recognition. In *34th Applied Imagery and Pattern Recognition Workshop (AIPR)*, pages 223–228, 2005.
- [35] A. W. K. Kong and D. Zhang. Competitive coding scheme for palmprint verification. In *International Conference on Pattern Recognition (ICPR)*, pages 520–523, 2004.
- [36] A. W. K. Kong and David Zhang. Feature-level fusion for effective palmprint authentication. In *First International Conference on Biometric Authentication (ICBA)*, pages 761–767, 2004.
- [37] A. W. Kin Kong, D. Zhang, and G. Lu. A study of identical twins palmprints for personal verification. *Pattern Recognition*, 39(11):2149–2156, 2006.
- [38] A. Kumar and C. Ravikanth. Personal authentication using finger knuckle surface. *IEEE Transactions on Information Forensics and Security*, 4(1):98–110, 2009.
- [39] A. Kumar and D. Zhang. Personal recognition using hand shape and texture. *IEEE Transactions on Image Processing*, 15(8):2454–2461, 2006.
- [40] X. Li. Modeling intra-class variation for nonideal iris recognition. In *Advances in Biometrics*, pages 419–427. Springer, 2005.

-
- [41] P. Lili and X Mei. The algorithm of iris image preprocessing. In *Fourth IEEE Workshop on Automatic Identification Advanced Technologies*, pages 134–138, 2005.
- [42] X. Liu, K.W. Bowyer, and P.J Flynn. Experiments with an improved iris segmentation algorithm. In *Fourth IEEE Workshop on Automatic Identification Advanced Technologies*, pages 118–123, 2005.
- [43] Guangming Lu, David Zhang, and Kuanquan Wang. Palmprint recognition using eigenpalms features. *Pattern Recognition Letters*, 24(910):1463 – 1467, 2003.
- [44] B. D. Lucas and T. Kanade. An Iterative Image Registration Technique with an Application to Stereo Vision. In *International Joint Conference on Artificial Intelligence (IJCAI)*, pages 674–679, 1981.
- [45] L. Ma, T. Tan, Y. Wang, and D Zhang. Efficient iris recognition by characterizing key local variations. *IEEE Transactions on Image Processing*, 13(6):739–750, 2004.
- [46] Libor Masek and Peter Kovesi. Matlab source code for a biometric identification system based on iris patterns. *M.Tech Thesis*, 2003.
- [47] A. Meraoumia, S. Chitroub, and A Bouridane. Fusion of finger-knuckle-print and palmprint for an efficient multi-biometric system of person recognition. In *IEEE International Conference on Communications (ICC)*, pages 1–5, 2011.
- [48] Abdallah Meraoumia, Salim Chitroub, and Ahmed Bouridane. Palmprint and finger-knuckle-print for efficient person recognition based on log-gabor filter response. *Analog Integrated Circuits and Signal Processing*, 69:17–27, 2011.

- [49] Goh Kah Ong Michael, Tee Connie, and Andrew Teoh Beng Jin. An innovative contactless palm print and knuckle print recognition system. *Pattern Recognition Letters*, 31(12):1708–1719, 2010.
- [50] K. Miyazawa, K. Ito, T. Aoki, K. Kobayashi, and H Nakajima. An effective approach for iris recognition using phase-based image matching. *IEEE Transactions on Pattern Analysis and Machine Intelligence*, 30(10):1741–1756, 2008.
- [51] D.M. Monro, S. Rakshit, and Dexin Zhang. Dct-based iris recognition. *IEEE Transactions on Pattern Analysis and Machine Intelligence*, 29(4):586–595, 2007.
- [52] A. Morales, C.M. Travieso, M.A. Ferrer, and J.B Alonso. Improved finger-knuckle-print authentication based on orientation enhancement. *Electronics Letters*, 47(6):380–381, 2011.
- [53] Loris Nanni and Alessandra Lumini. A multi-matcher system based on knuckle-based features. *Neural Computing and Applications*, 18:87–91, 2009.
- [54] Timo Ojala, Matti Pietikäinen, and Topi Mäenpää. Multiresolution gray-scale and rotation invariant texture classification with local binary patterns. *IEEE Transactions on Pattern Analysis Machine Intelligence*, 24(7):971–987, 2002.
- [55] Stephen M. Pizer, E. Philip Amburn, John D. Austin, Robert Cromartie, Ari Geselowitz, Trey Greer, Bartter Haar Romeny, John B. Zimmerman, and Karel Zuiderveld. Adaptive histogram equalization and its variations. *Computer Vision, Graphics, and Image Processing*, 39(3):355–368, 1987.
- [56] PolyU. The polyu knuckleprint database. <http://www4.comp.polyu.edu.hk/~biometrics/>.

- [57] PolyU. The polyu palmprint database. <http://www4.comp.polyu.edu.hk/~biometrics/>.
- [58] Ajita Rattani and Massimo Tistarelli. Robust multi-modal and multi-unit feature level fusion of face and iris biometrics. In *Advances in Biometrics*, volume 5558 of *Lecture Notes in Computer Science (LNCS)*, pages 960–969. Springer, 2009.
- [59] S. Ribaric and I Fratric. A biometric identification system based on eigenpalm and eigenfinger features. *IEEE Transactions on Pattern Analysis and Machine Intelligence*, 27(11):1698–1709, 2005.
- [60] Kaushik Roy, Prabir Bhattacharya, and Suen Ching Y. Iris recognition using shape-guided approach and game theory. *Pattern Analysis and Applications*, 14(4):329–348, 2011.
- [61] H. Schar. *Optimal operators in digital image processing*. PhD thesis, 2000.
- [62] Li Shang, De-Shuang Huang, Ji-Xiang Du, and Chun-Hou Zheng. Palmprint recognition using fastica algorithm and radial basis probabilistic neural network. *Neurocomputing*, 69(1315):1782 – 1786, 2006.
- [63] Jianbo Shi and Tomasi. Good features to track. In *Computer Vision and Pattern Recognition (CVPR)*, pages 593–600. IEEE, 1994.
- [64] Byungjun Son and Yillbyung Lee. Biometric authentication system using reduced joint feature vector of iris and face. In *Audio and Video Based Biometric Person Authentication*, volume 3546 of *Lecture Notes in Computer Science (LNCS)*, pages 513–522. Springer, 2005.

- [65] Z Sun, T Tan, Y Wang, and Stan Z. Li. Ordinal palmprint representation for personal identification. In *Computer Vision and Pattern Recognition (CVPR)*, pages 279–284, 2005.
- [66] Zhenan Sun and Tieniu Tan. Ordinal measures for iris recognition. *IEEE Transactions on Pattern Analysis and Machine Intelligence*, 31(12):2211–2226, 2009.
- [67] P. Viola and M Jones. Robust real-time object detection. *International Journal of Computer Vision*, 57(2):137–154, 2001.
- [68] Norbert Wiener. *Extrapolation, Interpolation, and Smoothing of Stationary Time Series*. The MIT Press, 1964.
- [69] R.P Wildes. Iris recognition: an emerging biometric technology. *Proceedings of the IEEE*, 85(9):1348–1363, 1997.
- [70] Xiangqian Wu, David Zhang, and Kuanquan Wang. Fisherpalms based palmprint recognition. *Pattern Recognition Letters*, 24(15):2829 – 2838, 2003.
- [71] Ming Xiong, Wankou Yang, and Changyin Sun. Finger-knuckle-print recognition using lgbp. In *International Symposium on Neural Networks, ISNN*, pages 270–277, 2011.
- [72] G.Z. Xu, Z.F. Zhang, and Y.D Ma. Automatic iris segmentation based on local areas. In *18th International Conference on Pattern Recognition (ICPR)*, volume 4, pages 505–508. IEEE, 2006.
- [73] Feng Yue, Wangmeng Zuo, Kuanquan Wang, and D Zhang. Fcm-based orientation selection for competitive coding-based palmprint recognition. In *19th International Conference on Pattern Recognition (ICPR)*, pages 1–4, 2008.

- [74] A. Zaim, M. Quweider, J. Scargle, J. Iglesias, and R Tang. A robust and accurate segmentation of iris images using optimal partitioning. In *18th International Conference on Pattern Recognition (ICPR)*, volume 4, pages 578–581. IEEE, 2006.
- [75] D Zhang. Polyu finger-knuckle-print database. <http://www4.comp.polyu.edu.hk/~biometrics/FKP.htm>.
- [76] D. Zhang, W K Kong, J. You, and M Wong. Online palmprint identification. *Pattern Analysis and Machine Intelligence*, 25(9):1041 – 1050, sept 2003.
- [77] Lin Zhang, Lei Zhang, and David Zhang. Finger-knuckle-print verification based on band-limited phase-only correlation. In *International Conference on Computer Analysis of Images and Patterns (CAIP)*, pages 141–148, 2009.
- [78] Lin Zhang, Lei Zhang, David Zhang, and Zhenhua Guo. Phase congruency induced local features for finger-knuckle-print recognition. *Pattern Recognition*, 45(7):2522–2531, 2012.
- [79] Lin Zhang, Lei Zhang, David Zhang, and Hailong Zhu. Online finger-knuckle-print verification for personal authentication. *Pattern Recognition*, 43(7):2560–2571, 2010.
- [80] Lin Zhang, Lei Zhang, David Zhang, and Hailong Zhu. Ensemble of local and global information for finger-knuckle-print recognition. *Pattern Recognition*, 44(9):1990 – 1998, 2011.
- [81] Zhijian Zhang, Rui Wang, Ke Pan, StanZ. Li, and Peiren Zhang. Fusion of near infrared face and iris biometrics. In *Advances in Biometrics*, volume 4642 of *Lecture Notes in Computer Science (LNCS)*, pages 172–180. Springer, 2007.

-
- [82] Le-Qing Zhu and San-Yuan Zhang. Multimodal biometric identification system based on finger-geometry, knuckleprint and palmprint. *Pattern Recognition Letters*, 31(12):1641 – 1649, 2010.

Publications

12. Aditya Nigam, Vamshi Krishna and Phalguni Gupta, “*Iris Recognition Using Block Local Binary Patterns and Relational Measures*” International Joint Conference on Biometrics, (**IJCB 2014**), Clearwater, Florida, USA, 29 September - 2 October 2014.
11. Aditya Nigam, Lovish, Amit Bendale and Phalguni Gupta, “*Iris Recognition Using Relational Measures*” IAPR 6th International Workshop on Computational Forensics, (**ICPR 2014**) Workshop, Stockholm, Sweden, August 24, 2014.
10. Aditya Nigam and Phalguni Gupta, “*Multimodal Personal Authentication Using Iris and Knuckleprint*”, 10th International Conference on Intelligent Computing (**ICIC 2014**), Taiyuan, China, August 3-6, Volume (8588) of LNCS, pp. (819-825), 2014.
9. Aditya Nigam and Phalguni Gupta, “*Designing An Accurate Hand Biometric Based Authentication System Fusing Finger Knuckleprint with Palmprint*” Neurocomputing, Elsevier (Impact Factor: 1.634), [Accepted].
8. Aditya Nigam and Phalguni Gupta, “*Quality Assessment of Knuckleprint Biometric Images*” IEEE 20th International Conference on Image Processing (**ICIP 2013**), Melbourne, Australia, September 15-18, pp. (4205-4209) 2013.
7. Aditya Nigam and Phalguni Gupta, “*Multimodal Personal Authentication System Fusing Palmprint and Knuckleprint*” 9th International Conference on Intelligent Computing (**ICIC 2013**), Nanning, China, July 28-31, Volume (375) of Springer, pp. (188-193), 2013.
6. Aditya Nigam, Anvesh T. and Phalguni Gupta, “*Iris Classification Based on its Quality*” 9th International Conference on Intelligent Computing (**ICIC**

- 2013), Nanning, China, July 28-31, Volume (7995) of LNCS, pp. (443-452), 2013.
5. Aditya Nigam and Phalguni Gupta, "***Palmprint Recognition using Geometrical and Statistical Constraints***" International Conference on Soft Computing for Problem Solving (**SocProS 2012**), Jaipur, India, December 28-30, Volume (236) of Springer, pp. (1303-1315), 2012.
 4. Aditya Nigam and Phalguni Gupta, "***Iris Recognition using Consistent Corner Optical Flow***" 11th Asian Conference on Computer Vision (**ACCV 2012**), Daejeon, Korea, November 5-9, Volume (7724) of LNCS, pp. (358-369), 2012.
 3. Amit Bendale, Aditya Nigam, Surya Prakash and Phalguni Gupta, "***Iris Segmentation using an Improved Hough Transform***" 8th International conference on Intelligent Computing (**ICIC 2012**), Huangshan, China, Volume (304) of Springer, pp. (408-415), July 25-29, 2012.
 2. Aditya Nigam and Phalguni Gupta "***Knuckleprint Recognition using Feature Tracking***" 6th Chinese Conference on Biometric Recognition (**CCBR 2011**), Beijing, China, December 3-4, Volume (7098) of LNCS, pp. (125-132), 2011.
 1. G.S Badrinath, Aditya Nigam and Phalguni Gupta, "***An Efficient Finger-knuckle-print based Recognition System Fusing SIFT and SURF Matching Scores***" 13th International Conference on Information and Communications Security (**ICICS 2011**), Beijing, China, 23-26 November, Volume (7043) of LNCS, pp. (374-387), 2011.